Università degli Studi di Cagliari

International PhD

in Innovation Sciences and Technologies

XXIX CYCLE- 2015-2016

Development and characterization of nanoporous and hybrid materials through electrochemical techniques for energetic applications

Scientific disciplinary sector: CHIM-07

PhD Student:	*Elisa Sechi*
PhD Coordinator:	*Prof. Roberto Orrù*
Tutor:	*Prof. Annalisa Vacca*

International PhD

in Innovation Sciences and Technologies

XXIX CYCLE- 2015-2016

Development and characterization of nanoporous and hybrid materials through electrochemical techniques for energetic applications

Scientific disciplinary sector: CHIM-07

PhD Student: *Elisa Sechi*

PhD Coordinator: *Prof. Roberto Orrù*

Tutor: *Prof. Annalisa Vacca*

This PhD thesis was developed mainly in the Department of Mechanical, Chemical and Materials Engineering (University of Cagliari) and in collaboration with the Department of Physics (University of Cagliari) and the Department of Chemistry (University of Southampton).

Elisa Sechi gratefully acknowledges Istituto Nazionale della Previdenza Sociale (INPS) for the financial support of her Ph.D. scholarship.

Contents

Abstract

This PhD project, focused on the achievement of nanoporous and hybrid materials, is divided in two main topics: the first one is the synthesis of nanoporous nickel electrodes through electrochemical dealloying; the second one is the preparation of polyaniline/porous silicon hybrid materials by aniline electropolymerization on n-type porous silicon surface. Both materials have been synthetized and characterized by electrochemical methods in order to study the effect of the parameters of preparation on their properties. A particular attention was pointed out on the photoactivity and catalytic behavior. The main results show that porous nickel can be obtained by selective etching of copper from Ni-Cu deposits, under pulsed voltage conditions. The highest values of surfaces have been obtained adopting a low ratio between the corrosion and relaxation time. These surfaces result fully exploitable for the hydrogen and oxygen evolution reactions, as well as for photoelectrochemical applications.

Concerning the porous silicon, the results show that an improved photoactivity can be achieved by electropolymerization of polyaniline, using the electroreduction of diazonium salt as underlayer. The hybrid samples present a higher photocurrent with respect to unmodified porous silicon, from the visible to the near-infrared region. Depending on the electrochemical conditions adopted for the synthesis, an increase in photocurrent more than one order of magnitude has been found.

Chapter 1

Introduction

Over the last decade, several works have been reported concerning the field of nanoporous conductive materials, since interesting properties get improved due to their enhanced surface area. For this reason, a great interest to explore their use in many applications such as sensing, energy systems and catalysts is emerged.
On the other hand, nanoporous conductive materials are suitable substrates to fabricate novel inorganic/organic composites, since it is possible to exploit a wider surface area.
In a similar way to nanoporous materials, nanocomposite structures have been widely investigated because they allow to improve the intrinsic properties of the single material and then, can be applied for a wide range of applications.
Electrochemical techniques represent a flexible and easy way to both synthesize and characterize porous systems based on metals and semiconductors. Furthermore, these methods allow also to functionalize the surface of such materials with organic molecules to create organic/inorganic heterostructures.

In this context this PhD project, focused on the achievement of porous and hybrids materials, is divided in two main topics:

- Synthesis of porous nickel oxides through electrochemical dealloying
- Preparation of Polyaniline/Porous silicon hybrid materials by aniline electropolymerization on n- type porous silicon surface

The common theme about these materials is the use of electrochemical techniques for their preparation and the study of their properties for energy-related applications, such as solar cells. The other point that joins the topics is the use of two different components exhibiting a p-type semiconductor

behaviour. The first component is polyaniline in its conductive form known as emeraldine salt, that it has been coupled with n-type porous silicon to obtain a p-n heterojunction; the second is nickel oxide (NiO) that is recently emerged among the forefront p-type semiconductors.

The Thesis is structured in four chapters subdivided in paragraphs for each topic, in order to allow the reader to better follow the progress of the research project.
A summary of this Thesis is reported below, where a short description of each chapter is given.

Chapter 1. Motivations and aim of the PhD thesis is reported and extensively discussed. A list of the publications in Journal and Conference papers is also given.

Chapter 2. The first PhD topic is presented and discussed.
A general overview of nickel based material employed for catalytic and solar energy-related applications is given. A description of electrochemical dealloying as method to produce nanoporous nickel follows along the chapter. Experimental methods and results about the synthesis of nanoporous nickel are presented. The results are subdivided in two paragraphs: the first and the second related to those obtained using boron doped diamond (BDD) and niobium (Nb) as substrate for the electrodeposition experiments, respectively. The results concerning the performance of the electrodes as electrocatalysts and photocathodes are reported.
At the end of the chapter short conclusion are given.

Chapter 3. The second topic of this PhD thesis is presented and discussed.
A general overview of hybrid heterojunctions and electrochemical functionalization of surfaces through diazonium salts is given. The attention is then focused on porous silicon and polyaniline characteristics, given the main mechanisms of the electropolymerization process.
The chapter continues with an overview of porous silicon/polyaniline heterojunctions. Experimental methods and results concerning the development of these materials by means of an electrochemical approach based on the electroreduction of diazonium salt are presented.

The results are divided in three main sections, related to each electrochemical phase of preparation of the hybrid materials. Preparation and performance of the devices will be widely discussed.
Finally, brief conclusions are given.

Chapter 4. This final chapter reports the final considerations and the future investigations.

1.1. Motivations

In this PhD thesis the development of two different materials by means of electrochemical techniques, have been studied. The performance of these materials for energy-related topics have been also investigated. Motivations about the necessity to focus the research on these fields are explained along this chapter, as well as the reasons deriving from the choice of these materials.

1) The first material is nanoporous nickel; it is proposed as electrocatalyst and photocathode.

Alkaline water electrolysis (AWE) is nowadays gaining consideration as a promising method for the large-scale production of carbon-free hydrogen and oxygen in view of power grid regulation and large scale energy storage. On one hand, the hydrogen production on cathodes could represent the possible hydrogen economy in the future, for instance in fuel cells. On the other hand, the oxygen production on anodes is also critical in some cases, for instance in internally-integrated fuel cell/battery systems. In spite of significant technological developments during the twentieth century, modern alkaline electrolysis cells are still limited by large energy consumption at limited operating current densities.
The development of catalytically active anodes and cathodes materials for the oxygen evolution reaction (*OER*) and hydrogen evolution reaction *(HER)* remains a challenging task.
With respect to the typically employed metals and metal oxides, such as Iridium oxide (IrO_2) or ruthenium oxide (RuO_2) for *OER* and platinum group metals (*PGM*) for *HER*, nickel presents different advantages: good corrosive resistance in alkaline solutions, commercial availability and low toxicity.
Moreover, nickel in its oxide form (NiO) is becoming interesting as promising material for photovoltaic applications, since it shows a p-type semiconductor behaviour. Photovoltaic energy represents an outstanding renewable source to reduce the actual high cost of energy consumption provided by fossil fuels.
In photovoltaic devices, it is very important to harvest as much light as possible by creating a large *p*/*n* heterojunction. By going from a smooth

surface to a porous surface, the area for light harvesting increases. As a result, these kind of electrodes enhance the excitation (hole/electron formation) as well as the mobility of charge carriers, resulting in an increase of efficiency device.
In this context, the contribution of this PhD work was to adopt electrochemical dealloying as method to tune the morphologic features of nickel based-electrodes in order to obtain an enhanced surface area, that should be promote an increase of both the photoactivity and the electroactivity.
In particular, the electrocatalytic performance of the as- prepared electrodes have been tested either towards hydrogen (*HER*) and oxygen evolution reaction (*OER*) and removal of phenol, used as a model of organic compounds.
Furthermore, a preliminary study of a thermal annealed dealloyed porous nickel working as photocathode compared with a smooth oxide nickel electrode is presented.

2) The second investigated material is a hybrid material constituted by porous silicon (*PSi*) and polyaniline (*PANI*).

In the last decade many research groups have been interested to study new methods to fabricate novel hybrid organic/inorganic structures for their huge potential in several applications, such as bioelectronics, clinical diagnostics, biological sensing, solar cells.
The main limitation of these systems is the short-term stability due to the lack of strong interfacial bonds between the organic molecules and the surface of the material. The electrochemical grafting of organic molecules, larger functional biomolecules and conducting polymers on conductive surfaces represents a chance to overcome this limitation. An affordable way to obtain covalent grafting on conductive surface is represented by the electrochemical reduction of diazonium salts: a very versatile alternative to conventional techniques. This strategy has been adopted to promote covalent bonds between aryl groups with several substituents and different substrates, such as gold and titanium.
A very promising polymer in this scenario is polyaniline (*PANI*): it has a potential use in a broad field due to its optical and electronic properties, low

cost, environmental stability and reversible control of conductivity by protonation and charge-transfer doping.

An outstanding material that can be coupled with *PANI* in order to create a heterojunction is porous silicon (*PSi*). Combining a n-type silicon (Si) substrate and *PANI* in its conductive form is possible to create a p-n heterojunction. Such configuration can be used for example to maximize the solar radiation adsorbed by photovoltaic devices; in this way should be possible to improve the photocurrent efficiency of the Si alone exploiting a wider surface area, as well as an organic coating as *PANI*.

Since the *PSi* surface is highly reactive and with a short term stability an approach that allows to stabilize the surface and to create a stable and uniform coating, based on the electrochemical reduction of 4-nitrobenzenediazonium salts (4-NBD), is proposed in this thesis.

The effects in photocurrent of *PANI* coating on *PSi* surface have been also investigated.

1.2. Publications in Journal and Conference Papers

Some of the topics in the present Thesis were presented in both national and international conferences and papers.

International Journal Papers:

M. Tiddia, G.Mula, M. Mascia, E. Sechi, A.Vacca, *Porous silicon–polyaniline hybrid composites synthesized through electroreduction of an aryldiazonium salt: preparation and photocurrent properties,* RSC Advances (2016), 6, 101880- 101887.

M. Tiddia, G. Mula, E.Sechi A.Vacca, E.Cara, N.D Leo, M. Fretto, L.Boarino, *4-nitrobenzene grafted in porous silicon: application to optical lithography,* Nanoscale Research Letters (2016), 11:436.

E.Sechi, A.Vacca, M. Mascia, S. Palmas, *Nickel-based nanoporous electrodes for water treatment,* Chemical Engineering Transaction (2016), 47, 97-102.

National and International Congresses and Conferences:

E. Sechi, A.Vacca, M.Mascia, S. Palmas, S. Corgiolu, P. Ampudia*, Preparation of Nickel Foams by selective corrosion of Ni/Cu films in different solvents,* 2nd E3 Mediterranean Symposium: Electrochemistry for Environment and Energy 2016, Gargnano (Italy)

E. Sechi, A.Vacca, M.V. Tiddia, G.Mula, M.Mascia, S. Palmas, S. Corgiolu, P. Ampudia, *Preparation of Polyaniline/Porous Silicon Hybrids for photovoltaic applications,* 2nd E3 Mediterranean Symposium: Electrochemistry for Environment and Energy 2016, Gargnano (Italy).

E. Sechi, M.Mascia, S. Palmas A.Vacca, *Catalytic activity towards hydrogen evolution of nanotubular Ni obtained through electrodeposition of Ni/Cu composites and anodic etching,* Convegno Nazionale Gricu 2016, Anacapri (NA), Italy.

E.Sechi, M.Mascia, S. Palmas, A. Vacca, S. Corgiolu, G.Mula, M Tiddia, *Hybrid Pani/PSi electrodes: preparation and photocurrent performances at different Wavelength,* 67th Annual Meeting of the International Society of Electrochemistry, 2016, The Hague (Netherlands).

E. Sechi, , M.Mascia, S. Palmas, A.Vacca, *Preparation of nanotubular Nickel through electrodeposition Ni/Cu composites and anodic etching***,** 67th Annual Meeting of the International Society of Electrochemistry, 2016, The Hague (Netherlands).

E.Sechi, A.Vacca, M. Mascia, S.Palmas*, Nickel-based nanoporous electrodes for water treatment,* The international conference of nanotechnology based innovative applications for the environment, 2016, Rome (Italy).

G.Mula, M. Tiddia, S. Rizzzardini, E.Sechi, S. Corgiolu,M.Mascia, A.Vacca, *pH switching of Photocurrent in polyaniline/porous silicon hybrid diffused heterojunctions Porous Semiconductors*, 10th Porous Semiconductors - Science and Technology (PSST) International Conference, 2016, Tarragona (Spain).

E.Sechi, A.Vacca, M. Mascia, S.Palmas**,** *Electrochemical dealloying of Ni/Cu films to obtain nanoporous nickel,* Giornate dell'Elettrochimica italiana, 2015, Bertinoro (Italy).

L.Mais, A.Vacca, M.Mascia, S. Palmas, E. Sechi, *Electrochemical etching of Cu-Ni alloy to obtain nanoporous nickel*,10th European Congress of Chemical Engineering, 2015, Nice (France).

In addition to the work presented in this Thesis the author has also participated to another research project that led to the publication of the following work in a national Conference:

A.Vacca, M.Mascia, S.Palmas, S. Corgiolu, V.Perra, E.Sechi, P.Ampudia, *Electrochemical Detection of Oligonucleotide Sequences linked on gold electrodes by diazonium Salts,* Giornate dell' Elettrochimica Italiana, 2016, Gargnano (Italy).

Chapter 2

Nanoporous nickel electrodes

2.1. Background

Nanoporous metals and their oxides are of particular interest for a wide range of potential applications, because of the improvement of their intrinsic properties with the extension of the active surface area.

For example, these materials have been explored as electrochemical catalysis, because the porous metallic frameworks can both increase the active area accessible to the reactant molecules and improve the electron mobility in the solid ligaments.[1–3] Other interesting applications for these materials have been widely investigated: from electrochemical sensors[1–4] to energy conversion/storage systems[3,5,6] and solar cells.[7–11]

In the past few decades, a number of advanced approaches have been explored to design and tailor the structure of porous metals. [12,13–17]

The field of development and application of porous metals is currently undergoing an exciting progress with increasing achievements. There is a great need to provide suitable updates of this kind of advanced materials including their fabrication methods, basic properties, and novel applications. A large number of strategies have been adopted to fabricate porous metals: template synthesis,[14,16,18–20] surfactant mediated synthesis[21,22] and dealloying. [1,2,12,23,24,25]

The last method has been commonly used for more than eighty years to produce Raney nickel, a porous metal powder prepared by chemical dealloying of $NiAl_3$ and employed as a heterogeneous catalyst.[26]

Dealloying is a corrosion process, in which the selective dissolution of the more active component from a homogeneous, single-phase alloy occurs, leaving behind a porous matrix.

A single phase alloy consists of two or multicomponent metals with different chemical activities: the difference in electrochemical potential

between the elements can lead to selective etching of the more active component under appropriate corrosion conditions, while the other remains intact.[12,23] The active element can be selectively removed either naturally in acid/base (known as chemical dealloying) or more quickly in an electrochemical system (electrochemical dealloying). Chemical dealloying is a free corrosion way, which is much easier to implement with respect to electrochemical dealloying. As a typical example, the simplest method that is reported in literature consists into dip Ag–Au alloys in nitric acid. The solubility of silver with respect to gold leads to the formation of nanoporous gold. The pores formation process of electrochemical dealloying has been subjected to a remarkable debate over the years and, although several efforts have been put to understand the precise mechanisms driving the pore formation it remains not totally understood. [1,12, 25,27,28,29] To understand the mechanism characterizing the pore formation during electrochemical dealloying a lot of competing processes should be considered: dissolution rate of the active component, surface diffusivity of the inert metal and capillary force.[2]

Typically, the noble component of a binary alloy moves to form two-dimensional islands by a surface diffusion process and passivates the surface, while the active component is electrochemically etched. Previous studies have shown that, after the more reactive metal atoms are dissolved at alloy/electrolyte interface, the nobler metal atoms at alloy/electrolyte interface undergo an atomic rearrangement process and form clusters, progressively more exposing the underlying more reactive metal atoms.[25]

The parallel processes of chemical dissolution of the more reactive atoms and atom rearrangement of the more inert atoms permit the dissolution to proceed and eventually penetrate throughout the whole alloy.[12] In general, two important parameters should be considered for the experimental observation on the dealloying process: the parting limit and the critical potential. The parting limit defines the limiting concentration of the nobler component in an alloy, above which dealloying cannot proceed. The critical potential (E_c) is the threshold that marks the transition from the alloy passivity zone to that where the rapid formation of pores starts.[1]

Dealloying typically occurs at a potential above the E_c. However, some studies have reported that selective dissolution can also occurs below E_c, although the dissolution rate is relatively slow.[30]

Among various systems Ag–Au alloy was firstly investigated to produce nanoporous gold by means of electrochemical dealloying; [31] after these systems many kinds of nanoporous metals (such as Ni, Au, Ag, Cu, and Pt) have been fabricated using the dealloying method. [25]

Due to their unique bulk appearance, three-dimensional metal nano-ligaments and open pores structure, dealloyed nanoporous metals have received extensive attention in areas such as catalysis, energy storage, sensing and actuation. [31] Among the metals, Ni based materials have lately attracted great attention for its applications in photonic materials[32], electrochemical capacitors[32] and electrocatalysts for hydrogen[33–41] and oxygen evolution reactions. [42,43,44,45,46] Nanoporous nickel can be developed starting from Ni-Cu systems by electrochemical dealloying under specific experimental conditions. In a copper-nickel (Cu/Ni) alloy system, copper is thermodynamically more stable than nickel but taking advantage of the formation of a passive nickel oxide film, nanoporous nickel can be prepared by selective electrochemical etching of copper.

With this technique different nickel porous electrodes have been obtained: results have shown that the morphology of the porous structures depends on the composition of Cu/Ni film electrodeposited and on the electrochemical conditions used for the selective corrosion.[47]

In this PhD thesis the electrochemical behavior of porous nickel electrodes produced by the electrochemical anodic dissolution of Cu-Ni films has been studied. The electrodeposition of copper-nickel films was carried out on boron doped diamond and niobium electrodes using different experimental conditions.

One of the most important challenges for the current dealloying technology is how to control the morphology and composition of the porous materials. To address this challenge, the effects of different dealloying parameters, such as operative conditions and solution composition have been investigated in this research project. The as- prepared electrodes have been then tested for electrocatalytic and energy- related applications.

To introduce the topic a brief overview about catalytic and energy- related applications is given in the following paragraphs, pointing the attention on nickel-based materials.

2.1.1. The role of nickel-based materials as catalysts

Metals, their oxides and mixtures are widely used as catalysts and electrocatalysts in several processes; among the others, the oxygen and hydrogen evolution reaction deriving from the oxidation and reduction of water plays an important role in environmental applications.
On one hand, the hydrogen production on cathodes could represent the possible hydrogen economy in the future: the ideal energy carrier that can be an alternative to fossil fuels, for instance in fuel cells.
On the other hand, the oxygen production on anodes is also critical in some cases, for instance, in internally-integrated fuel cell/battery systems. In spite of significant technological developments during the twentieth century, the production of catalytically active anode materials for the oxygen evolution reaction (*OER*) and cathodes for hydrogen evolution reaction (*HER*), remains a challenging task. There is the necessity to find alternative materials to platinum group metals (*PGM*)[48] and the so-called *active anodes* (IrO_2 or RuO_2),[49] typically employed for *HER* and *OER*, respectively.
Among the metals, nickel based materials present different advantages such as commercial availability, low toxicity and good corrosive resistance in alkaline solutions. Moreover, nickel electrodes have been early proposed for the degradation of several organic compounds such as amines and alcohols. [50]
The *HER* has been extensively studied in the literature. The overall reaction in alkaline media is written as:

$$\boldsymbol{2H_2O + 2e^- \rightarrow H_2 + 2OH^-} \qquad \textbf{(1)}$$

Here **(1)** is a multi-step process. When metallic electrodes are used as cathodes, metal active centers (M) are involved in the reaction path.
About the mechanism proposed for nickel based materials to produce hydrogen in aqueous solutions, is generally accepted that at room temperature it can proceeds via **(2)**, followed either by **(3)** or **(4)** reaction mechanism, as follows: [51]

$$\boldsymbol{H_2O + M + e^- \rightarrow MH_{ads} + OH^-} \qquad \textbf{(2)}$$

$$H_2O + MH_{ads} + e^- \rightarrow H_2 + M + OH^- \quad (3)$$

$$MH_{ads} + MH_{ads} \rightarrow H_2 + 2M \quad (4)$$

Here, MH_{ads} is the electrode surface occupied by hydrogen atoms.
The first reaction step **(2)** is a one electron discharge, so-called *Volmer* step, that leads to the formation of surface-bounded hydrogen ad-atoms (MH_{ads}). The second step is either electrochemical desorption, so called *Heyrovsky electrochemical desorption* **(3)** or chemical recombination, so-called *Tafel catalytic recombination* **(4)**.
Both steps lead to the evolution of molecular hydrogen and involve the adsorbed hydrogen H_{ads}. Thus, the rate of hydrogen evolution depends on the energy of the metal-hydrogen bond. *PGM* present the main catalytic activity towards to the *HER*. However, *PGM* cannot be use in the large-scale alkaline water electrolysis due to their high cost.

The overall *OER* reaction in alkaline media includes four electrons and can be described by the following equation:

$$4OH^- \rightarrow O_2 + 2H_2O + 4e^- \quad (5)$$

The reaction expressed by this equation is a complex multi-step process. In spite of many important investigations, there are still unanswered mechanistic questions. On nickel based electrodes *OER* normally takes place on the surface covered with oxides but it is also well known that also nickel hydroxide can catalyze *OER* reaction.[52]
In the first case the simplified mechanism, generally proposed is:[43,46]

$$M + OH^- \rightarrow MOH + e^- \quad (6)$$

$$MOH + OH^- \rightarrow MO^- + H_2O \quad (7)$$

$$MO^- \rightarrow MO + e^- \quad (8)$$

$$2MO \rightarrow 2M + O_2 \quad (9)$$

Where M is a free catalytic site on the electrode surface for *OER*.

Moreover, according this mechanism the electrochemical reaction shown in **(7)** or (**9)** can be the determining step for the reaction, depending on the potential applied. In case of formation of highly oxides sites which catalyze *OER* reaction the hydroxilation of the nickel surface proceeds as follows:[52.53]

$$\boldsymbol{Ni + 2OH^- \rightarrow Ni(OH)_2 + 2e^-} \qquad \textbf{(10)}$$

Where $Ni(OH)_2$ layer forms under open circuit potential in alkaline solutions. In recent studies it has been suggested that nickel is passivated by several molecular layers of nickel oxide NiO covered with a compact layer of $Ni(OH)_2$ hydroxide staying in contact with solution. [46,53] At higher anodic potential Ni(II) shifts to Ni(III) following the reaction[50] :

$$\boldsymbol{Ni(OH)_2 \rightarrow NiOOH + H^+ + e^-} \qquad \textbf{(11)}$$

NiOOH sites react to form oxygen. Another possibility is to exploit these sites for the oxidation of organic pollutants present in the solution.
Indeed, it is well known that electrochemical degradation of organic molecules at the *active anodes* (i.e. IrO_2 or RuO_2) takes place simultaneously with the oxygen evolution reaction, which involves the formation of highly oxidised sites: at these sites the oxidation of organics reactants competes with oxygen evolution due to chemical decomposition of the oxides with higher oxidation state.[54]
In general, the electrocatalytic properties of the electrode materials depend on both electronic and geometrical factors. The former are those connected to the properties that affect the strength of the surface-intermediate bonds and depends on the chemical structure of the surface.
The second issues are those related to the extension of the actual surface area and are not strictly related to real electrocatalysis, since the activation energy of the reaction will not be affected.[55]
It is possible to improve the electrocatalytic performance by reducing the activation energy or by increasing the actual active surface per apparent unit.

2.1.2. The role of nickel-based materials in energy-related applications

Metal oxide semiconductors have been proposed in low-cost solar energy-related applications, such as photovoltaic devices[56], photocharge storage,[57] photoelectrochemical water splitting. [58]

The majority of the works on photovoltaic devices adopts n-type metal oxides, due their related properties: chemical and thermal stability, easiness to process, and availability. The typically metal oxides, which have dominated the literature in this area, are typically wide band gap n-type: titanium dioxide (TiO_2), bismuth vanadate ($BiVO_4$), zinc oxide (ZnO), hematite (α-Fe_2O_3), and tungsten trioxide (WO_3).[7,59–63]

Recently, many efforts have been put in the research of p- type oxide semiconductors. Indeed, to couple a p-type oxide cathodes with n-type oxide anodes can be a suitable alternative to harvest more of the solar spectrum and then, improve the performance and reduce the cost of solar harvesting systems. Nowadays Nickel oxide (NiO), copper iodide (CuI),[11] copper thiocynate (CuSCN)[64] are the most studied p-type oxide semiconductors. [59,65,66] Among these materials, NiO, with a large band gap of 3.6-4eV presents the following advantages: good stability and transparency, low cost, environmental benignity, and ease of preparation.[29,67] The main limitation of the commercial NiO is the very low efficiency. Two principal solutions are typically adopted to overcome this limitation. The first is based on the sensitization of p-type semiconductors with organic dyes or quantum dots.[10,67] For example Bach and co-workers demonstrated that the photovoltaic solar efficiency of a tandem solar cell using a dye-sensitized NiO photocathode increases of 2.42%, due to its contribution to generate photocurrent.[68] Other works are also present in literature that confirm the benefits of this method.[10,69,70] Anyway, these systems presents three main drawbacks: 1) a very fast charge recombination between the holes in NiO and the reduced dye, 2) small open-circuit photovoltage and 3) high dark current.

The second chance to increase the overall power-conversion efficiency can be represented to the adoption of a simple strategy to change the morphology of NiO. Indeed, by going from a smooth surface to a porous surface increases the area for light harvesting. As a result, these types of electrodes enhance the excitation (hole/electron formation) as well as the mobility of charge carriers, resulting in an increase of device efficiency.

Moreover, these materials present the advantage to exhibit exclusive channels for mass transport. [71,72]

Evidences of the improvement of the efficiency with the use of nanomaterials with micro-nano, hierarchical, or mesoporous structures as n-type photoanodes have been reported.[9,73,74]

Few reports have focused the attention on the morphology and structure of the materials employed as p-type photocathodes. Recently, He et. al obtained a maximum incident photo- current conversion efficiency of 22% from macroporous NiO prepared by means of etching in alkaline solutions.[65]

In this context, the contribution of this PhD work was to adopt electrochemical dealloying as method to tune the morphologic features of nickel based electrode in order to obtain an enhanced surface area, that should be promote an increase of the photocurrent efficiency.

Specifically, in this PhD thesis a preliminary study of a thermal annealed dealloyed porous NiO working as photocathode compared with a smooth oxide nickel electrode is presented.

2.2. Experimental methods

2.2.1. Chemicals

Boric acid (H_3BO_3) and potassium hydroxide (KOH) were purchased from Sigma-Aldrich®. Sodium sulphate anhydrous (Na_2SO_4), nickel sulphate hexahydrate ($NiSO_4*6H_2O$), copper sulphate pentahydrate ($CuSO_4*5H_2O$), phenol (C_6H_6O), glycerol ($HOCH_2CH(OH)CH_2OH$), ethylene glycol ($C_2H_6O_2$), potassium nitrate (KNO_3) and sulfuric acid (H_2SO_4) were supplied by Carlo Erba.

2.2.2. Electrochemical Set-up

All electrochemical experiments were performed at room temperature using an AUTOLAB PGSTAT302N (Metrohm, Switzerland) potentiostat/galvanostat equipped with a frequency response analyzer controlled with the NOVA software (***Fig. 1***).

Fig. 1 *Autolab 302N potentiostat-galvanostat controlled by NOVA software (Metrohm, Switzerland).*

Two conventional hand-made three-electrode cells (V_1 = 10 ml and V_2 =25 ml) made by a cylindrical Teflon chamber, containing the electrolytic solution were used to develop nickel porous electrodes. The cell with a higher volume was employed only for the electrodeposition experiments performed onto niobium substrates.
The working electrode was located at the bottom of the cell and the electrical contact consists in an aluminum disc. The circular exposed geometrical area of the electrodes was 0.5 cm^2 (diameter = 0.8 cm).

A platinum titanium grid placed in front of the anode at 1 cm distance constituted the counter electrode. A saturated calomel electrode (SCE) was used as reference electrode. The working electrodes are described in the following subchapter. All the potentials presented refer to SCE. The SCE potential measured with respect to the standard hydrogen electrode (SHE) is 0.241 V.
As an example, ***Fig. 2*** shows the electrochemical set-up employed to prepare Ni-Cu deposits onto BDD substrates and the associated nickel nanoporous electrodes.

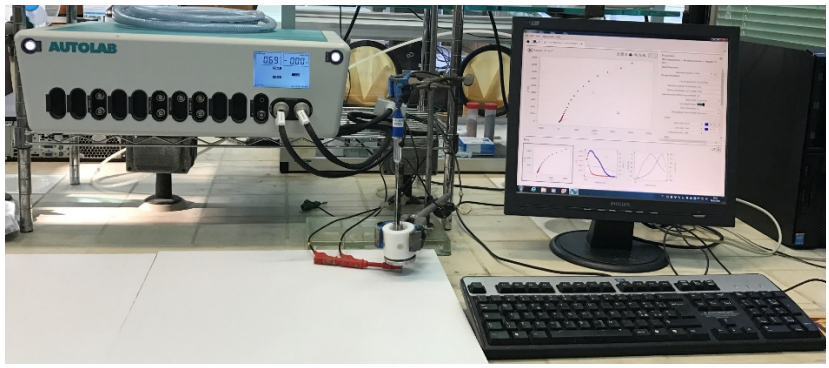

Fig. 2 *Electrochemical set-up employed to prepare Ni-Cu deposits and nanoporous nickel electrodes starting with a BDD as electrodeposition substrate.*

Working Electrodes

The preparation of the Ni-Cu deposits was performed using two substrates:

- Boron doped diamond *BDD* (thickness 2 mm, Neocoat, Switzerland)
- Niobium foil (thickness 0.25 mm, 99.8%, Aldrich)

Prior to electrochemical deposition, BDD were polished with water and acetone on a cloth polishing pad and then submitted to galvanostatic runs (2 mA) in 0.5 M H_2SO_4 for 30 minutes. The electrodes were then rinsed with double-distilled water. An exposed geometrical area of 0.5 cm^2 was adopted for the electrodeposition experiment.
Prior to deposition, niobium discs were mechanical polished with wet diamond particles (sizes: 3, 1, 0.5 μm) and colloidal silica gel (particles size: 0.05 μm), each for 5 minutes on polishing cloths and rinsed with triple-distilled water. Then, the samples were submitted to sonication in acetone for 15 minutes. Finally, the electrodes were again rinsed with triple-distilled water. An exposed geometrical area of 15.9 cm^2 was adopted for the electrodeposition experiment.

2.2.3. Electrochemical synthesis and characterization

Synthesis

The freshly polished electrodes adopted as working electrodes were subjected to electrodeposition in a plating solution containing 0.5 M $NiSO_4$, 0.005 M $CuSO_4$ and 0.5 M H_3BO_4 (pH=4), using a constant potential of -0.8 V for a total time of 130 minutes and under gentle stirring conditions.
In a preliminary investigation BDD substrates were adopted; in a second time the electrodeposition was carried out onto niobium discs in order to get a higher reproducibility with respect to the BDD substrates.
Concerning the nickel-copper (Ni-Cu) deposits onto niobium (Nb) substrates after the electrodeposition the discs were cut in slices with a final exposed geometrical area of 0.5 cm^2.
After the Ni-Cu films have been deposited, the films were subjected to anodic dissolution both in aqueous and water glycerol solutions$(1:3)_{V/V}$, containing 0.5 M H_3BO_4 and 0.5 M Na_2SO_4 (PH= 3.8). In addition, in this case stirring conditions have been used.
In a preliminary investigation the experiments were carried at pulsed voltage modulated between V_{corr} (E= 0.5 V) and V_{relax} (E=*OCP*) for time durations of t_{corr} (1 s) and t_{relax} (5 s), respectively. A total time of 30 minutes was employed (typically the dissolution current drops to zero within this

period). In addition to water/glycerol solutions, the Ni-Cu films deposited onto niobium electrodes were also subjected to anodic dissolution in water/ethylene glycol solutions $(1:3)_{V/V}$.
In order to better clarify the effect of the corrosion and relaxation times, the experiments at Nb substrates were carried out adopting several time durations, which are shown in ***Table 1***. For the first case shown in ***Table 1*** both aqueous, water glycerol and ethylene glycol solutions were adopted.
The other samples shown in the table were prepared using only aqueous solutions. The samples developed as NPt_1t_5 but using water/glycerol and water ethylene glycol are designated as $NPGt_1t_5$ and $NPeGt_1t_5$.
For comparison the anodic dissolutions experiments have been also performed at a constant voltage of 0.5 V for 30 minutes in either aqueous and water/glycerol solutions.

name	t_{corr}	t_{relax}	t_{corr}/t_{relax}
NPt_1t_5	*1*	*5*	*0.2*
$NPt_{0.1}t_{0.5}$	*0.1*	*0.5*	*0.2*
$NPt_{0.01}t_{0.05}$	*0.01*	*0.05*	*0.2*
NPt_1t_{50}	*1*	*50*	*0.02*
$NPt_{0.1}t_5$	*0.1*	*5*	*0.02*
$NPt_{0.01}t_{0.5}$	*0.01*	*0.5*	*0.02*

Table 1 *Experimental conditions adopted for the electrochemical dealloying experiments performed onto Ni-Cu film electrodeposited onto Nb substrates.*

For clarity, in the rest of the text the samples produced in aqueous solutions using constant and pulsed voltage and *BDD* as electrodeposition substrates are called as *Const-Ni-foams* and *Pulse-Ni-foams*, respectively.
The samples prepared with the same experimental conditions but employing aqueous/glycerol solution are instead named *ConstG-Ni-foams*

and *PulseG-Ni-foams* in case of constant and pulsed voltage conditions, respectively.

Morphologic characterization

A scanning electron microscope (SEM) equipped with EDX detector (Zeiss, Germany) was used to characterize the morphology and the chemical composition of the nanoporous nickel electrodes before and after the anodic dissolution (***Fig. 3***). Auger electron Spectroscopy (AES) was also used to investigate the distribution of the copper and nickel before and after the anodic dissolution experiments. Focused ion beam (FIB) was used to obtain very precise cross-sections of the samples for subsequent imaging via SEM, to evaluate nickel pores thickness.

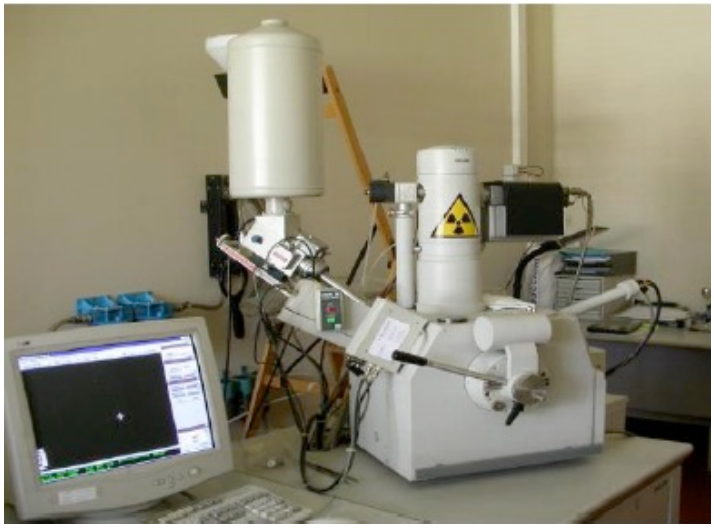

Fig. 3 *Scanning Electron Microscopy (SEM) equipped with Energy Dispersive X-Ray (EDX) detector (Zeiss, Germany).*

Cyclic voltammetries (CV) and linear sweep voltammetries (LSV)

The electrodes have been characterized through cyclic voltammetry (CV) starting from the open circuit potential (OCP) in the negative or positive

direction at different potential windows using different solutions composition, such as Na_2SO_4 0.5 M, KNO_3 0.1M, electrodeposition and corrosion solutions, etc. Scan rate was varied in a range from 5 to 100 mV/s for all the measurements.
In order to avoid ion concentration gradients in the electrolyte, the solution was magnetically stirred prior to each scan.
Linear sweep voltammetry (*LSV*) were also performed to study the behavior of the electrodes in electrodeposition solutions in the potential range from E= OCP to E= -1 V in cathodic direction. Moreover, LSV were carried out in anodic direction in the anodic dissolution solutions in the potential range from E= OCP to 1 V. A sweep rate in a range between 0.5 mV/s and 5 mV/s was typically adopted. For comparison the same analysis were also performed in nickel and copper foil electrodes.

Electrochemical impedance spectroscopy (EIS)

The characterization of the electrode/electrolyte interface was also carried out through electrochemical impedance spectroscopy (EIS), using the attained current density at around the OCP value. The measurements have been performed in a frequency range from 30-100 kHz down to 0.1 - 0.01 Hz with excitation amplitude of 10 mV in different kind of solutions.
The impedance spectra were then fitted to an equivalent electrical circuit by using the ZSimpWin 2.0 software (EChem software).

Electrocatalytic activity

Prior to test the electrocatalytic activities, the electrodes were conditioned by potential cycling, over 150 times, between E= 0 and E= 0.8 V Vs. SCE at 50 mV/s in 1M of KOH. The electrochemical oxidation was carried out in order to produce $Ni(OH)_2$/NiO/Ni composites. The kinetic parameters of the *OER* and *HER* process were determined by linear sweep voltammetry (*LSV*) in basic solutions containing 1 M KOH at sweep rate of 0.5 mV/s. A potential range from OCP to 1 V and OCP to -1.3 V was employed for *OER* and *HER*, respectively. To obtain overpotential η values, reversible oxygen potential was taken as 172 mV Vs. SCE, while the reversible hydrogen potential was taken as 1.067 V Vs. SCE. [75]

Moreover, EIS measurements were carried out at both in the oxygen and hydrogen evolution region in alkaline solutions containing KOH 1 M.
LSV analysis have been also performed in order to investigate the electrocatalytic activity of the electrodes towards phenol removal in the anodic region. The potential range used varies from OCP to 1 V and solutions containing 0.1 M KOH were employed. Furthermore, the anodic oxidation of phenol was evaluated by cyclic voltammetry in 0.1 M KOH containing 28 ppm of phenol, followed by degradation experiments. These ones were carried out both in potentiostatic and galvanostatic mode at 1 V and 5 mA respectively. Solutions containing 14 ppm of phenol were employed. During the runs, samples of electrolyte were withdrawn and analyzed for the concentration of reactant by 4-aminoantipiryne method (ASTM 5530D) using UV spectrophotometer (Agilent Technologies, Cary Series Spectrophotometer; ***Fig. 4***).

Fig. 4 *UV spectrophotometer (Agilent Technologies, Cary Series Spectrophotometer).*

Photoelectrochemical measurements

After the anodic etching, the samples were submitted to potential cycling, over 150 times, between E= 0 and E= 0.8 V Vs. SCE at 50 mV/s in 1M of KOH. After oxidation, the electrodes were rinsed in deionized water and

dried in a nitrogen stream. A subsequent annealing treatment was needed in order to convert $Ni(OH)_2$ and NiOOH groups in NiO. Thermal treatment was carried out in air atmosphere for 30 min at 500 °C, after ramping 5 °C min^{-1}.

The photoelectrochemical measurements were carried out in a hand-made three photoelectrochemical cell (PEC), equipped with a quartz window. The investigated samples were adopted as working electrodes while a platinum wire constituted the counter electrode and a SCE the reference. 0.1 M KNO_3 aqueous solution was used as the supporting electrolyte. The same electrochemical cell was employed to study the behaviour of the systems under dark conditions. The PEC was irradiated with a 300 W Xe lamp (LOT-Quantum Design Europe) equipped with AM O optical filter.
The light transmission spectra obtained with the AM O filter is shown in ***Fig. 5***. This filter was employed since NiO has a band gap of 3.6-4 eV, that converted through Plank Law ($E = h\nu$) corresponds to a wavelengths λ range $310 < \lambda < 345$ nm.
The incident power density (W/cm^2) of the light was measured by LP 471 UVU or LP 471 PAR quantum radiometric probes: the recorded value was 140-138W/m^2. In ***Fig. 6*** the complete photoelectrochemical set-up is shown.

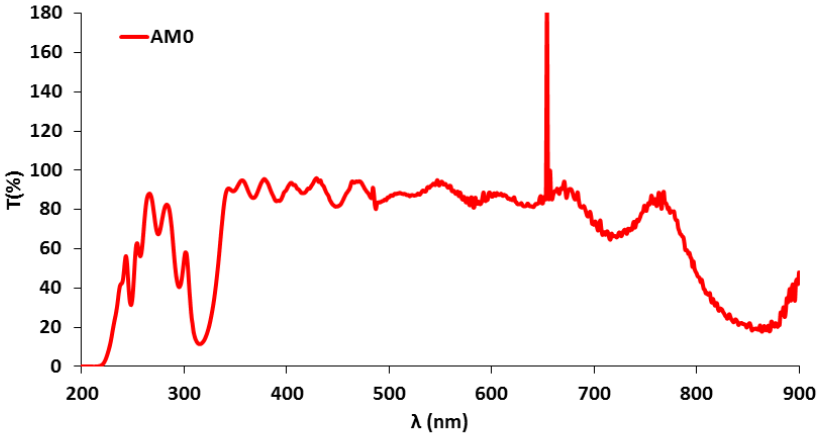

Fig. 5 *Transmission spectra of 300 W Xe lamp (LOT-Quantum Design Europe) equipped with AM O optical filter.*

In order to text the photoactivity of the electrodes, LSV were performed from E= OCP to E= -1.2 V in cathodic direction at scan rate of $5mVs^{-1}$. Both dark and irradiation conditions were adopted. Photocurrent density was calculated with respect both the nominal and the real surface area of the samples.

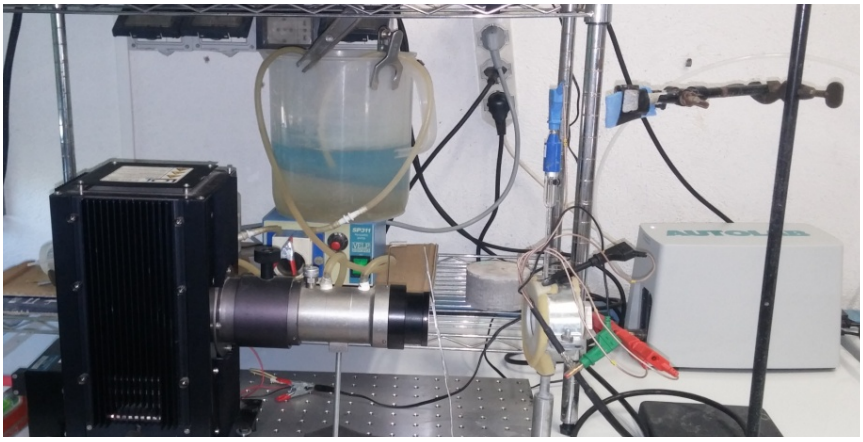

Fig. 6 *Photoelectrochemical set-up employed to study the photoactivity of the samples.*

2.3. Results: BDD as substrates

2.3.1. Electrodeposition

Before to undergone the freshly BDD samples to electrodeposition the electrochemical behaviour of nickel and copper was investigated, performing CV using different potential windows.
Fig. 7 displays the CV of a BDD electrode in a solution containing 0.5M Ni(II) and 0.005 M Cu(II) (***Fig. 7a***; black curve) and in a solution containing only Ni(II) ***(Fig. 7a*;** red curve) at scan rate of 10 mV/s. All the solutions contained also 0.5 M H_3BO_4. ***Fig. 7b*** shown the CV in the same solution of ***Fig. 7a*** (black curve) with a different potential window.

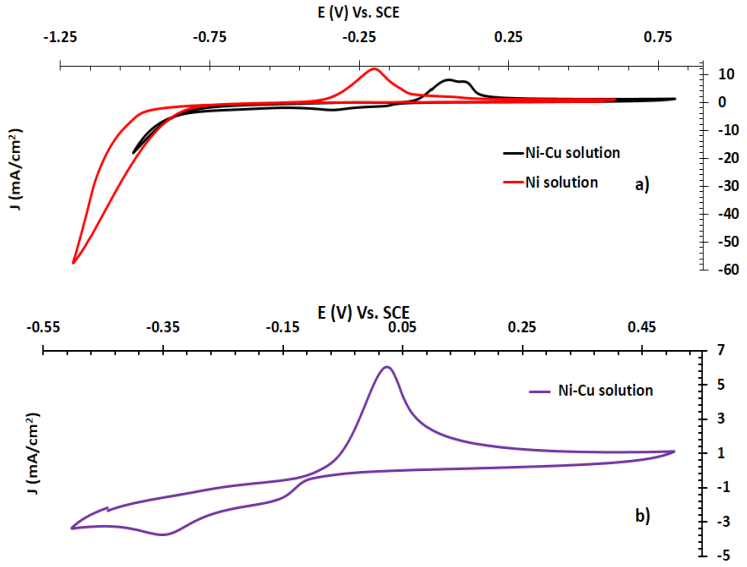

***Fig.** 7 CV recorded in aqueous solutions containing 0.5 M H_3BO_4 and 0.5 M $NiSO_4$ (in red) and 0.5 M $NiSO_4$ + 0.005 M $CuSO_4$ (black) and (b) 0.5 M $NiSO_4$ + 0.005 M $CuSO_4$ with a cathodic scan limit of -0.5V, on a BDD electrode at scan rate of 10 mV s^{-1}.*

As can be noticed, observing the cyclic voltammogram performed in the solution containing only nickel (red curve) the onset of nickel deposition appears at about -0.76 V with an exponentially increase of the current with the negative potential, while on the positive scan the peaks associated with Ni stripping are seen at around -0.2 V.

The charge related to oxidation is smaller than that of reduction, showing that Ni passivation arises during the anodic scan. This behaviour is in agree with previous electrodeposition studies of Ni(II) on ITO substrates.[76]

Conversely, observing the cyclic voltammogram performed in the solution containing both nickel and copper ions (black curve), can be appreciated the reduction peaks associated with Cu(I) and Cu(0) (at E= -0.4 and -0.1V respectively) and the onset nickel deposition potential (at -0.75 V). In the potential range between -0.1 V to -0.75 V (the onset nickel deposition potential) the diffusion limited deposition of copper is the only reduction process. A more negative potentials of -0.75 V, both nickel and copper can

be electrodeposited. In this potential window the deposition rate of copper is independent to the potential applied and it depends only from its concentration in solution; the rate of Ni deposition instead increases as the potential becomes more negative. At potential more negative of -1 V bubble formation, related to hydrogen evolution was observed. To assess if the anodic peaks were related to the stripping of copper, a CV using a scan negative limit at E= -0.5 V in the same solution was performed (See ***Fig. 7b***). Two reduction peaks can be observed which can be related to the reduction of Cu(II) to Cu(I) at -0.15 V and the reduction of Cu(I) to Cu(0) at -0.15 V. In the reverse scan, one single anodic peak related to the stripping of the deposited metallic copper is seen at around 0.05 V.

When the nickel deposition occurs (See black curve in ***Fig.7a***) two anodic peaks can be appreciated: the first at 0.05 V attributable to the stripping of Cu(II) to metallic copper (as in ***Fig. 7b***) and a second at 0.15V. This last peak can be related to the stripping of copper from Ni-Cu deposit onto BDD surface. Also in this case this behaviour is in agree with the study of Chang et. all about Ni- Cu electrodeposition on ITO substrates.[76]

The absence of nickel stripping peaks indicates that Cu can be selectively removed from the Ni-Cu deposit due to nickel passivation. It is important to underline that nickel passivation phenomena is allowed by the presence of boric acid in solution.[77]

According to the results from the CV study, the deposition of the Ni/Cu films has been performed at -0.8 V in order to obtain a Cu-rich films.

Fig. 8 displays the SEM images of the electrodeposits obtained at potential of -0.8V.

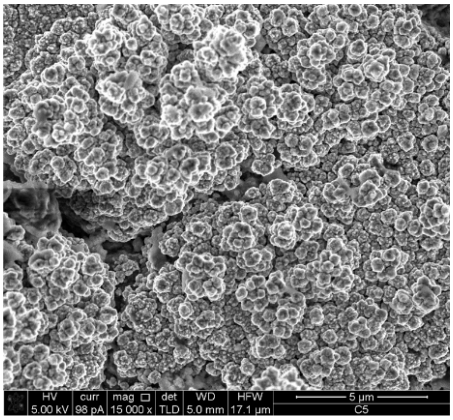

Fig. 8: *SEM image of Cu-Ni deposits prepared at V= -0.8V.* [78]

It can be observed a regular and homogeneous distribution of Ni-Cu electrodeposits onto the BDD surface, with a dendritic morphology reflecting the original morphology of the BDD substrates.

The Auger mappings of Ni and Cu (See ***Fig. 9a*** and ***Fig. 9b***), further confirm a uniform composition of the deposits and reveal a homogeneous distribution of each element on the substrate.

The EDX analysis of the Ni-Cu films shows a molar fraction of 0.4 and 0.58 for nickel and copper, respectively (***Fig.10***).
This means that a deposition potential of -0.8 V has allowed the electrodeposition of both elements on the BDD surface in a similar amount. Previous reports have shown that to prepare a better porous structure the component being etched should generally be near or higher than 50%.[76]

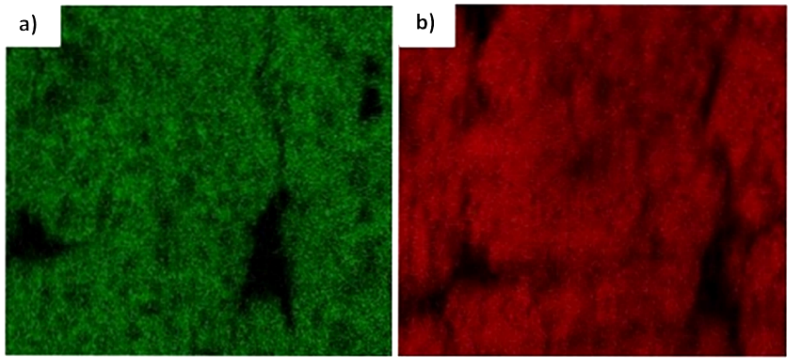

Fig. 9 *Auger mappings of nickel (a) and copper (b) of the deposits.* [78]

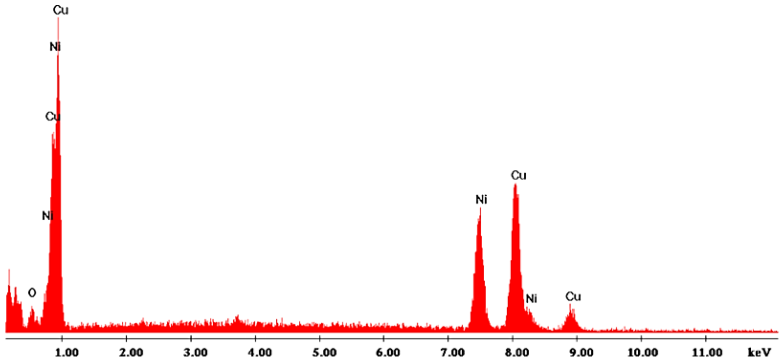

Fig. 10 *EDX analysis performed onto Ni-Cu systems, electrodeposited onto a BDD substrate at V=-0.8 V for a total time of 130 min.*

Fig. 11 shows a typical J/V curve recorded during an electrodeposition experiment; the passed charge was evaluated integrating the area under the J/t curve obtaining a value of 4 Coulombs.

Fig. 12 shows the J/V electrochemical response of Ni- Cu deposits, recorded at 100 mV/s in the solution employed for the anodic dissolution experiment.

As can be noticed is present a single anodic peak at about 0.25 V, associated to the stripping of the deposited metallic copper on the BDD surface. On

the reverse scan the cathodic peak (at around -0.4 V) related to deposition of the metallic copper onto electrode can be observed.

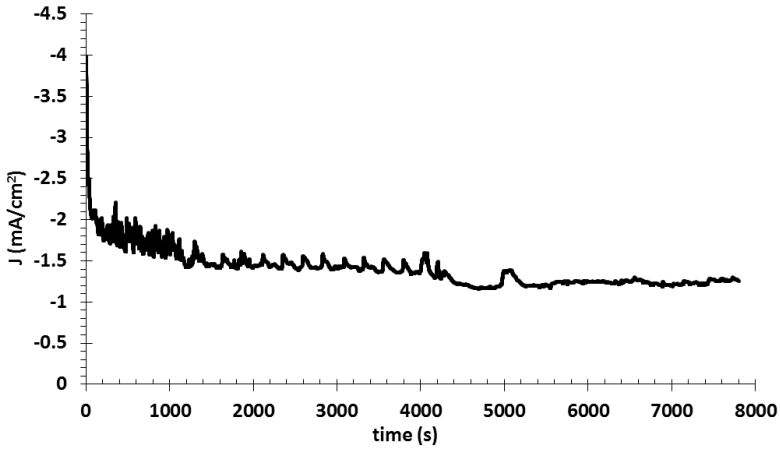

Fig. 11 *J/t curve recorded during the electrodeposition experiment onto BDD electrode performed at V= -0.8V.*

The reduction-oxidation peaks related to nickel behaviour cannot be observed due to the formation of a passive oxide film on its surface in such solution[77,79].

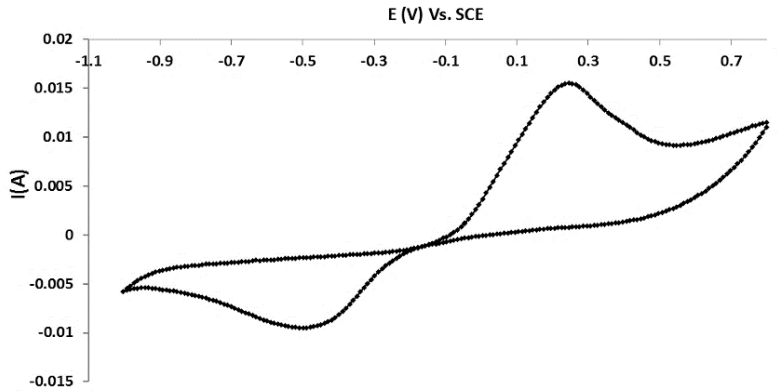

Fig. 12 *Cyclic voltammogram of Ni-Cu deposits recorded in 0.5 M Na_2SO_4 and 0.5 M H_3BO_4, at scan rate of 100 mV s^{-1}.* [78]

2.3.2. Electrochemical anodic dissolution

Prior to undergone the Ni-Cu electrodeposits to anodic dissolution, the electrochemical behaviour of bare nickel and copper foil have been investigated (***Fig. 13***).

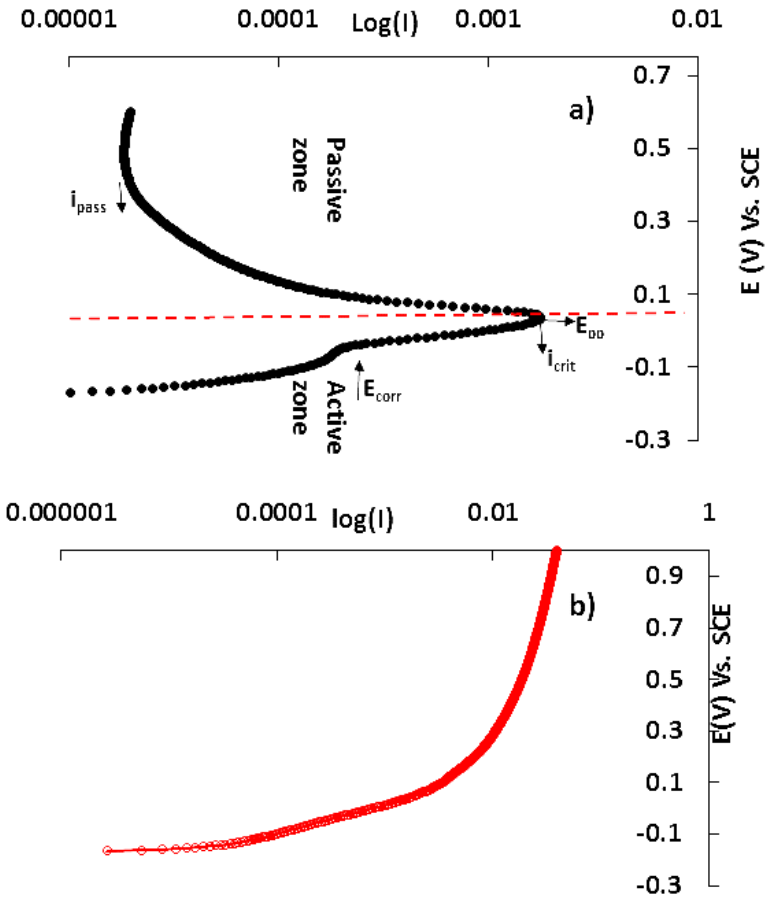

Fig. 13 *Linear polarization curve of Ni (a) and Cu (b) in 0.5 M Na_2SO_4 and 0.5 M H_3BO_4 at scan rate of 5 mV s^{-1}.*

The polarization diagram of nickel in the corrosion solution (***Fig. 13a***) exhibits the presence of two zones: activation and passivation zone.[80,81] As

the potential increases from the corrosion potential E_{corr} at -0.1 V the current increases according the typical metal dissolution behaviour, until to reach a critical value of i_{crit} of around 1.7 mA. This point defines the starting of stability for passive films that takes place at potential higher then primary passive potential E_{pp}, centred at 0.05 V.
Beyond E_{pp} the current falls several orders of magnitude to a residual current i_{pass} of 0.1 mA.
This behaviour demonstrates the passivity condition that exhibits nickel in such solutions. The ***Fig. 13b*** displays the polarization curve of copper: it can be observed the absence of passivation zone and the corrosion onset potential at around 0 V.
After this preliminary investigation, the Ni-Cu deposits were submitted to selective anodic dissolution of copper in a solution containing 0.5 M Na_2SO_4 and 0.5 M H_3BO_4 (See *Synthesis*). The voltage value of both the potentiostatic runs and pulsing step for the anodic dissolution experiment was chosen 200mV higher than the copper stripping peak potential (See ***Fig.12***), due to the reasonably high current generation, which is in good consistence with previous studies.[77]
Moreover, this potential ensures to perform the copper dissolution when the nickel passivation occurs (See ***Fig. 13 a***). The pulse bias was set slightly above to the OCP value in order to guarantee a generation of a very low current. Earlier studies report that minimum current flow is necessary for the relaxation steps in order to avoid the re-deposition or dissolution of copper, giving the time to atoms to reorganize without disturbance. [12]

Fig. 14 displays the SEM images of the electrodeposits undergone to anodic dissolution in both aqueous and water/glycerol solution $(25, 75\ \%)_{V/V}$, using potentiostatic and pulsed voltage conditions.
The anodic etching results in the formation of a nickel porous structure with different characteristics, which depend on the employed operative conditions. It is evident that a higher porosity, a homogeneous pores distribution and a more regular pores shape have been achieved using pulsed voltage conditions (*Pulse-Ni-Foams* in ***Fig. 14b*** and *PulseG-Ni-Foams* in ***Fig.14d***).
In particular, it can be noticed a more regular tubular pores shape in case of *PulseG-Ni-Foams* (***Fig.14d***), although these samples show higher pores

sizes and the presence of copper deposits on their surface; occurrence probably due to the difficulty to control the current value during the relaxation time (bias).

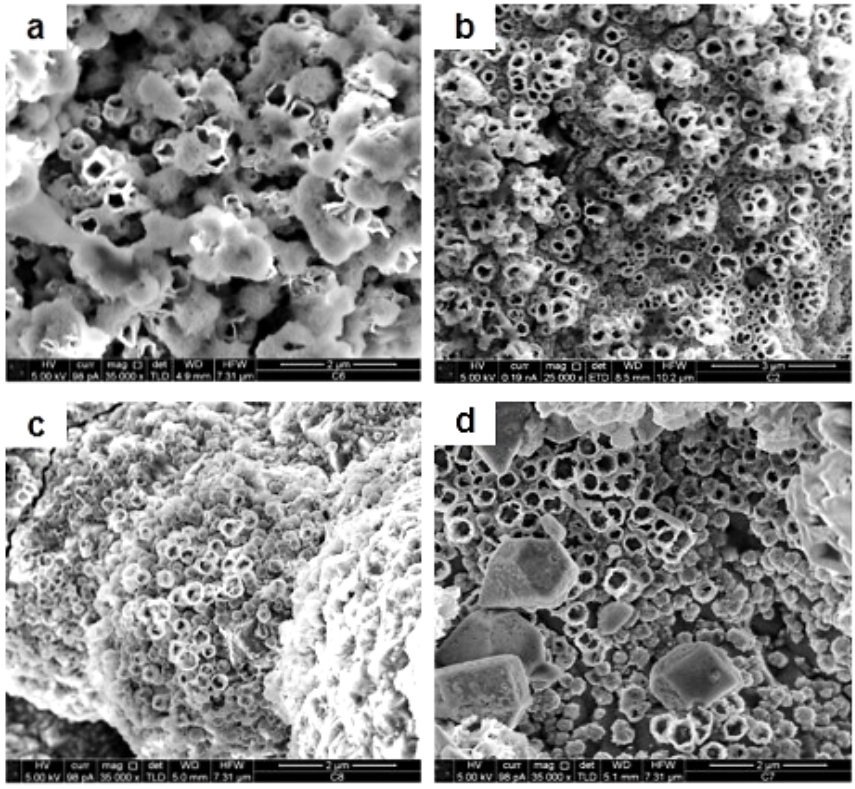

Fig. 14 *SEM images of Cu-Ni electrodeposits submitted to anodic dissolution in aqueous solutions (a-b) at constant (Const-Ni-foams; a*[78] *and pulsed voltage (Pulse-Ni-foams; b); (c-d) in water/glycerol solutions at constant (ConstG-Ni-foams; c) and pulsed voltage (PulseG-Ni-foams; d).*

Table 2 summarizes the molar fractions of copper, nickel and oxygen and the pores diameters of the samples (calculated from SEM images) obtained from the different experiments.

Name	Solution	V	X_{cu} (%)	X_{ni} (%)	X_O (%)	d_{pores} (nm)
Const-Ni-foams	aqueous	constant	48	28	23	100-300
ConstG-Ni-foams	glycerol	constant	-------	75	25	150-300
PulseG-Ni-foams	glycerol	pulsed	5	90	5	200-400
Pulse-Ni-foams	aqueous	pulsed	-------	92	6	100-300

Table 2 *Molar fractions of Cu, Ni and O calculated by EDX analysis. Also the pores diameters of the samples are reported.*

The *EDX* result show that except for *Const-Ni-foams* (***Fig. 14a***) the other electrodes show an almost total absence of copper traces and then a high level of purity.
As example, ***Fig. 15*** shows the Auger mappings of Ni and Cu and of both elements related to *Pulse-Ni-Foams*. These analyses confirm the EDX results, showing a very low presence of copper onto the electrodes.

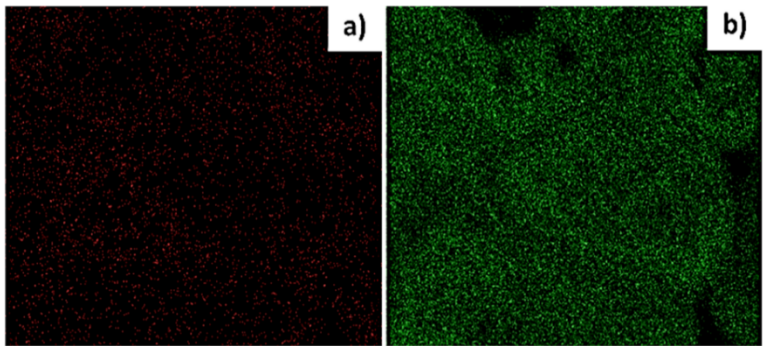

Fig. 15 *Auger mappings of copper (a) and nickel (b) elements of Pulse-Ni-foams.*

2.2.3.Capacitance measurements

Capacitance measurements have been performed in order to obtain a measure of the real surface area of the electrodes, that it is strictly connected to the double layer capacitance C_{dl}. From the measure of C_{dl} can be determined the roughness R_{ough} and the morphologic factor φ of the samples, which give us an indication about the porosity of the samples. Both the porosity factors can be determined from C_{dl}, exploiting the linear dependence of the capacitive current i_c on the scan rate v, typically observed for rough and porous electrodes. [82–84] As a representative example, ***Fig. 16*** displays the complete voltammogram of *ConstG-Ni-foams* at scan rate of 100 mV/s and the differential voltammograms, recorded at the same scan rate but in a range of 100mV, in aqueous solutions containing Na_2SO_4 0.5 M. The differential voltammogram used in the determination of the differential capacities covers the interval 0.2-0.3 V: it is clearly identifiable a capacitive potential interval in this region that can be ascribed to the only non-Faradic component. The non-Faradic C_{dl} takes account of the charge accumulation in the electrode solution interface, as the only storage mechanism.

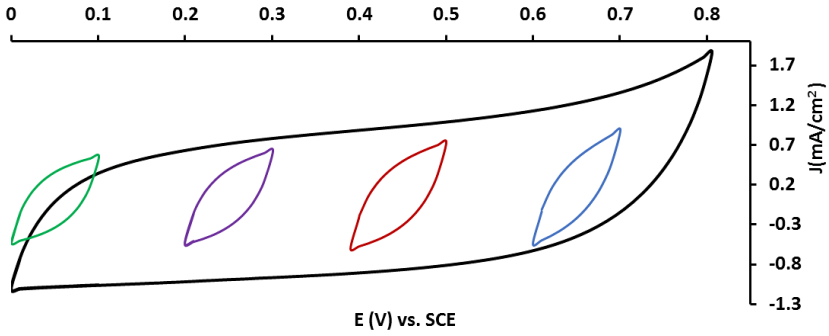

Fig. 16 *Complete and differential voltammogram of ConstG-Ni-foams in aqueous solution containing Na_2SO_4 0.5 M, at scan rate of 100 mV/s.*

In ***Fig. 17a*** and ***Fig. 17b*** are reported the CV in the selected interval for *ConstG-Ni-foams* at low scan rate v_{low} and high rate v_{high}, respectively.

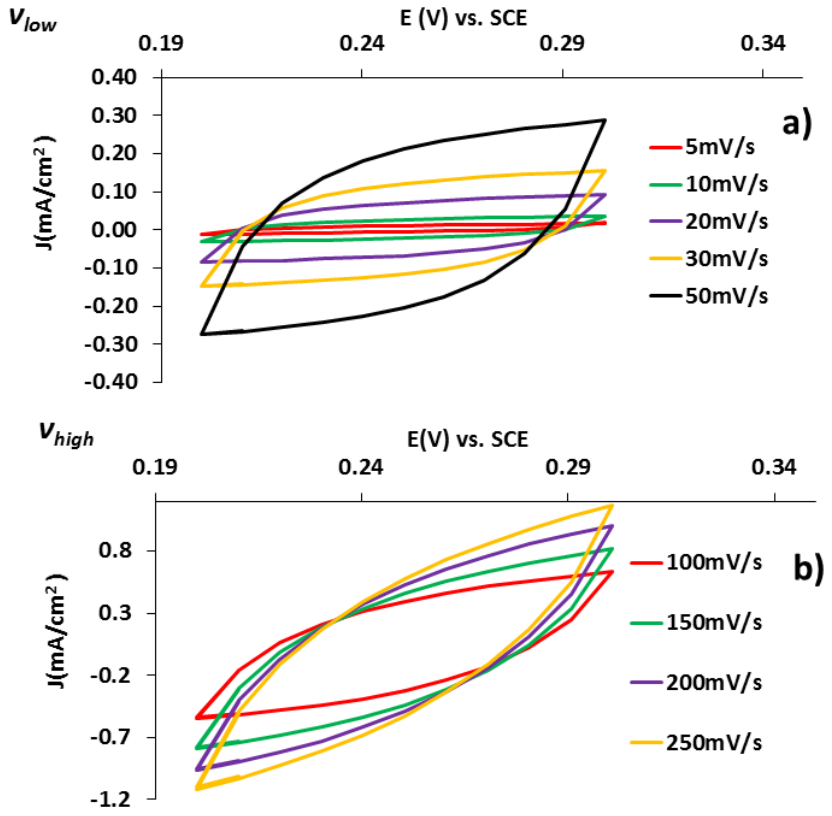

Fig. 17 *CV of ConstG-Ni-foams in aqueous solution containing Na_2SO_4 0.5 M, at (a) low scan rate (5, 10, 20, 30, 50 mV/s) and (b) high scan rate (100, 150, 200, 250 mV/s).*

It can be appreciated two distinct behaviours at v_{high} and v_{low}: the first related to the more accessible surface area of the electrodes and the second to both the less and more accessible regions.

As shown in ***Fig. 17***, two distinct behaviours of i_c can be appreciated. For low scan rate interval v_{low} (***Fig. 17a***), i_c is essentially constant over a broad potential interval preceding the anodic switching potential. At v_{high} instead an approximately stationary i_c is appreciated just near to the anodic switching potential. Moreover, two potential values (singularity) both on the forward and backward scans where i_c is independent from the v can be

observed. This behaviour is in agree with previous studies.[82] A possible explanation about this behaviour was related to the ionic resistance inside the pores, R_p, as a function of v.[85] Based on these considerations, the measure of i_c using the midpoint of the potential window (0.25V), typically used in literature is not totally accurate, due to the deviation from linearity observed at high scan rate.[83,86–88]

Anyway, other studies showed that the measure of i_c is more adequate when it is calculated from the last recorded CV, taking care that the potential employed is located within the last 20% of the potential interval covered.[82] For these reasons, the values of capacitive current densities j_c ($j_c=i_c/A$; A is the nominal area of the electrodes) have been measured in the differential voltammogram at 0.29 V (in anodic direction), for each value of v.

Fig. 18 shows the plot of j_c versus both v_{low} and v_{high}. The linear dependence of the capacitive current j_c on the scan rate v, confirms the non-Faradic behaviour of the current in the selected potential range.

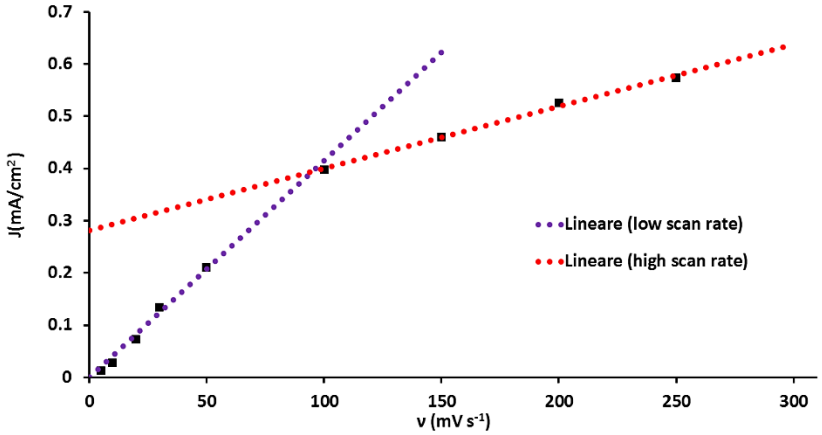

Fig. 18 *J/v answer of ConstG-Ni-foams at low scan rate (in violet)and high scan rate (in red)calculated at 0.29 V.*

This linear behaviour was obtained for all the experimental conditions, demonstrating the presence of both an inner and external accessible porous region in all the cases.

Taking into account that the differential capacitance C_{dl} is defined as:

$$C_{dl} = \left(\frac{di_c}{dv}\right)_V \qquad (12)$$

From v_{low} and v_{high} domain (first and second segment in ***Fig. 18***) can be determined both the C_{dl} and the external capacitance C_{de}, following:

$$\boldsymbol{i_c = C_{dl} v_{low}} \quad \textbf{(13)}$$

$$\boldsymbol{i_{ce} = C_{de} v_{high}} \quad \textbf{(14)}$$

Where V is the potential, i_{ce} is the capacitive current associated to the more accessible regions.
Considering **(13)** and **(14)** can be obtained the inner differential capacitance C_{di}:

$$\boldsymbol{C_{di} = C_{dl} - C_{de}} \quad \textbf{(15)}$$

Finally, the roughness R_{ough} and the morphologic factor φ of the samples can be calculated following:

$$\boldsymbol{R_{ough} = \frac{C_{dl}}{C_I}} \quad \textbf{(16)}$$

$$\boldsymbol{\varphi = \frac{C_{di}}{C_{dl}}} \quad \textbf{(17)}$$

Where C_I is the capacitance of a smooth nickel electrode, generally taken with the value of 20 µF/cm^2. [82]
Table 3 summarizes the values of the parameters discussed above, obtained in each experimental condition.
It can be observed that 0.6 <$\boldsymbol{\varphi}$ < 0.79 and 220 <R_{ough} <340 have been obtained depending on the experimental conditions. It worth to be noticed that samples prepared with potentiostatic mode present comparable R_{ough} values with respect *PulseG-Ni-foams*, but lower φ, due to the inferior difference between C_{de} and C_{di}. Moreover, the highest C_{de} of *ConstG-Ni-foams* with respect to the others samples, can be attributed to the incomplete coverage of the BDD substrate, being the same a rough substrate (See ***Fig. 14 d***). It is also evident that higher values of C_{di} have been obtained for *Pulse-Ni-foams*: occurrence that confirms the SEM results (See *Electrochemical anodic dissolution).*

Name	C_d (μF/ cm²)	C_{dl} (μF/ cm²)	C_{de} (μF/ cm²)	φ	R_{ough}	d_{pores} (nm)
Const-Ni-foams	4400	2600	1800	0.6	220	100-300
ConstG-Ni-foams	5300	2200	3100	0.67	265	150-300
PulseG-Ni-foams	4400	2900	1500	0.79	220	200-400
Pulse-Ni-foams	6800	5100	1700	0.75	340	100-300

Table 3 *C_{dl}, C_{di}, C_{de}, R_{ough}, φ obtained for Const-Ni-foams, ConstG-Ni-foams, Pulse-Ni-foams and PulseG-Ni-foams. In addition, the d_{pores} of the samples, obtained from SEM analysis are reported.*

2.3.4. Electrocatalytic activity

Oxygen and hydrogen evolution reactions

In order to investigate the electrocatalytic performance of the electrodes towards *OER* and *HER* the kinetic parameters of the related processes have been determined, through *LSV* in basic solutions, taking into account both the geometric (A) and the real surface area (A_r) of the electrodes.
The polarization curves are normally represented by Tafel equation:

$$\boldsymbol{\eta = a + \beta log J} \qquad \textbf{(18)}$$

Where η is the applied overpotential, a is the intercept of the curve related to the exchange current density i_o, β is the Tafel slope and J is the current density.
The η were obtained by subtracting the reversible hydrogen/oxygen equilibrium potential $E^0_{O2/H2}$ Vs. SCE from E applied, as follows:

$$\boldsymbol{\eta = E_{appl} - E^{o}_{O_2/H_2(Vs.SCE)}} \qquad \textbf{(19)}$$

where E_{appl} is the potential applied Vs. SCE and $E^{o}_{O_{2/(Vs.SCE)}}$ and $E^{o}_{H_2\,(Vs.SCE)}$ were taken as 0.17 and 1.07 Vs. SCE.[43,89]

The difference between these potentials is a direct measure of the irreversibility of the electrochemical process.

It is common practice in literature to express the apparent activities of the electrodes with the parameter $\eta_{10,}$ (i.e overpotential at current density of 10 mA/cm^2), regarding the geometric surface area of the samples, since the current is related to the amount of hydrogen/oxygen through the Faraday's law.[43] This parameter gives us an indication of the quantity of energy should be adopted to produce a precise amount of oxygen/hydrogen.

About the mechanism proposed for nickel based materials to produce hydrogen in aqueous solutions, is generally accepted that at room temperature it can proceeds via *Volmer* reaction, followed either by *Heyrovosky* or *Tafel* reaction mechanism, as explained in *The role of nickel based materials as catalyst*.

The equation **(2)** followed to the third reaction **(3)** yields to a slope β ca. 120 mV/Dec, while the *Volmer -Tafel* reaction **(3)-(4)** leads to a slope β of 40 mV/s.[34] Anyway, it has been demonstrated that formally it is impossible to discriminate at which overpotential the rate determining step *rds* changes when β is ca. 120 mV/ dec; in fact this value of β is also obtained when the surface coverage by adsorbed hydrogen tends to 1 and the *rds* is *Heyrovsky*.[90]

Fig. 19 shows the Tafel plots for both *Pulse-Ni-foams* and *PulseG-Ni-foams*, while ***Table 4*** summarizes the obtained kinetic parameters obtained for the investigated electrodes in *HER* region.

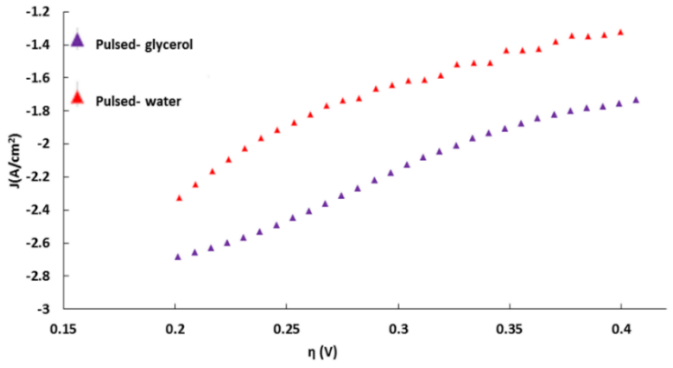

Fig. 19 *Tafel plot for HER of the Pulse-Ni-foams in water and PulseG-Ni-foams solutions in KOH 1 M at sweep rate of 0.5 mV s^{-1}.*

The obtained values of β demonstrate that *HER* process proceeds via *Volmer-Heyrovosky* reaction. Moreover, values of i_o higher of four orders of magnitude have been achieved with respect to typical recorded values for smooth nickel electrodes of 0.07 μA/cm^2, demonstrating that the porous surface is fully accessible for *HER*.[91] As expected, the electrodes showing the highest surface area present the best electrocatalytic performance towards *HER* (see and i_o and η_{10} in ***Table 4***).
Anyway, to understand if the totality of the inner surface area was fully exploited for the faradic process and the electroactivity depended just from the extension of the surface of the electrodes, the exchange current density was also calculated with respect to the real surface area A_r.
This parameter can be estimated as:

$$A_r = A * R_{ough} \qquad \textbf{(20)}$$

In ***Table 4*** the exchange current density normalized per the real surface area is designated as i_{or}.

Name	R_{ough}	β (mV/ sec)	i_o (mA/cm²)	η_{10} (mV)	i_{or} (μA/ cm²)
Pulse-Ni-foams	340	128	0.16	235	0.47
PulseG-Ni-foams	220	156	0.05	410	0.22

Table 4: *β, i_o, η_{10}, i_{or} related to HER, obtained from the interpolation of the polarization curve represented in Fig. 19. β, i_o have been extrapolated from the potential window 0.2 <η <0.3 V.*

As can be appreciated i_{or} higher of one order of magnitude have been achieved for both the electrodes with respect to smooth nickel electrode. This can be attributed to the other factors, which have a role in determining the electroactivity, as the morphology and the chemical structure. For example, the morphology of the porous structure can affect the detachability of evolving bubbles, while the presence of traces of copper may enhance the intrinsic catalytic activity of the material.

Conversely, the polarization curve recorded in *OER* region related to nickel based materials typically shows the presence of two defined Tafel regions at low η_{low} and high overpotentials η_{high}. The presence of these two regions can be explained by the change in the valence state of the active sites of the catalysts and by the influence of higher oxide on *OER*. The linear part of Tafel curve led to theoretical β of 40 mV/dec and 120 mV/dec [92] in case of reaction shown in **(9)** and **(7)** as *rds*, respectively (See *The role of nickel based material as catalyst*). Anyway, β for *OER* depends on the composition of the oxide electrodes and on the supports employed temperature and solution composition. Values ranging from 40 to 90 mV/dec have been found for η_{low}. [44,42,92] For η_{high} instead have been found values ranging from 120-220 mV/dec.[42,44 ,92]

In ***Fig. 20*** the CV_s of the *Pulse-Ni-foams* recorded over 150 times between E= 0 mV and 650 mV, at scan rate of 100mV/s in 1 M KOH are shown. It can be observed the anodic and cathodic peak related to the transition Ni(II)/Ni(III) oxides at 0.1 V and 0.45 V, respectively (See **(11)** in *The role of nickel based material as catalysts*). It worth to be noticed that the current peaks increase remarkably with the number of scans. This can be attributed to an enrichment of the Ni(III) oxides at the surface of the electrode with increasing of the scans, resulting in a thicker electrocatalytic layer. [93]

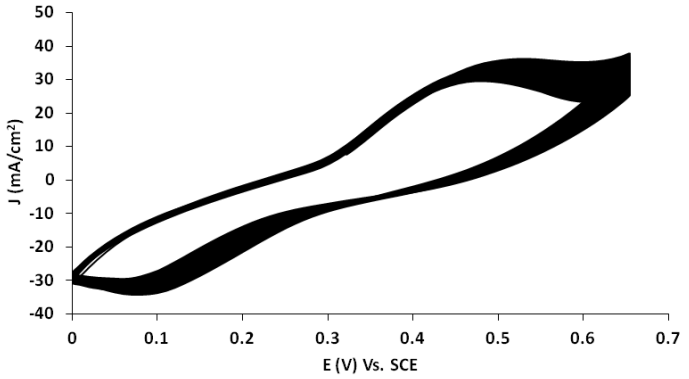

Fig. 20 *Cyclic voltammogramm of the Pulse-Ni-foams in 1 M KOH at scan rate of 100 mV* s^{-1}. [78]

The polarization curve related to the *OER*, illustrated in ***Fig. 21*** displays the presence of two Tafel regions at η_{low} (200-300 mV) and η_{high} (300-400mV) and for both *Pulse-Ni-foams* and *PulseG-Ni-foams,* respectively.

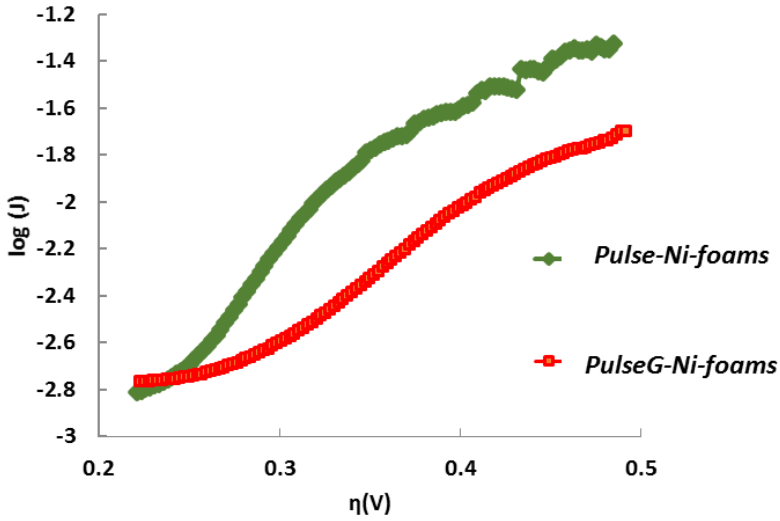

Fig. 21 *Tafel plot for OER of the Pulse-Ni-foams and PulseG-Ni-foams in KOH 1 M at sweep rate of 0.5 mV* s^{-1}.

Table 5 summarizes the obtained kinetic parameters obtained for the investigated electrodes in *OER* region for both η regions.

Name	R_{ough}	β_1 (mV/ sec)	i_o (mA/cm²)	i_{or1} (μA/ cm²)	β_2 (mV/ sec)	i_{o2} (mA/cm²)	i_{or2} (μA/ cm²)	η_{10} (mV)
Pulse-Ni-foams	340	90	0.004	0.012	140	0.2	0.59	310
PulseG-Ni-foams	220	90	0.003	0.013	157	0.1	0.46	400

Table 5 *β_1, i_{o1}, i_{or1}, β_2, i_{o2}, i_{or2}, η_{10} of samples characterized by different values of R_{ough}. The parameters β_1, i_{o1}, i_{or1}, have been calculated in the OER overpotential range between 0.2-<η_{low}< 0.3 V; β_2, i_{o2}, i_{or2} between 0.3<η_{high}< 0.4 V.*

As can be seen, the obtained β values for η_{high} (β_2) and η_{low} (β_1) were comparable than those of smooth Ni based electrodes. [43,44]
Compared to a smooth nickel anode the obtained i_o value for η_{low} region was five order of magnitude higher; whereas for η_{high} region (i_{o2}) was about 2 order of magnitude higher; [92] the remarkable increase can be attributed also in this case to the enhanced surface area of the porous electrodes. About η_{10} values of 310 and 400 mV have been found for *Pulse-Ni-foams* and *PulseG-Ni-foams* electrodes. It is evident that the best results in terms of i_o, i_{o2} and η_{10} have been achieved for *Pulse-Ni-foams*. Again, the reason is essentially linked to the higher surface area of the porous structure, as in *HER* case. Furthermore, comparing the real exchange current density i_{or} at η_{low} a remarkable increase with respect to a smooth nickel electrode of three order of magnitude is still observed. As for *HER*, this can be ascribed to the intrinsic properties of the samples deriving from the electrochemical dealloying process. Comparable values of i_{or2} (exchange current density calculated at η_{high}) with respect a smooth nickel electrode have been instead found. This suggests that at η_{high} the gas evolution is too vigorous to allow to fully exploit the overall surface area.

To ensure a complete characterization of the electrode/electrolyte interface and the investigated reactions, *EIS* measurements were made in the potential range corresponding to the linear part of the previously polarization curves, where the steady state conditions could be guaranteed. The Nyquist representation of the impedance of the pulsed samples in basic media at several anodic η shows the presence of one or two deformed and overlapped semicircles, both dependent on the voltage applied (***Fig. 22***).
It is possible to notice that the diameter of the semicircles at low frequencies considerably diminishes with the anodic η, demonstrating an increase of oxygen evolution rate at η_{high}. ***Fig 22d*** shows the comparison between the Nyquist plot of *Pulse-Ni-foams* and *Pulse-Ni-foams* at η =0.345 V: it worth to be noticed the different behaviour of the electrodes at the same η that demonstrates that at *Pulse-Ni-foams* the oxygen formation occurs at low overpotential values.
The experimental data of the impedance response characterized by one or two semicircles in the Nyquist plot has been modelled using one-time constant (1T) electric equivalent circuit (*EEC*) model and the 2T time

constant parallel model, respectively. The first model is the classic *Randles* model in which the solution resistance R_s is in parallel with the transfer charge resistance R_{ct} and CPE_1, which is used instead of the double layer capacitance C_{dl} (***Fig. 23a)***.

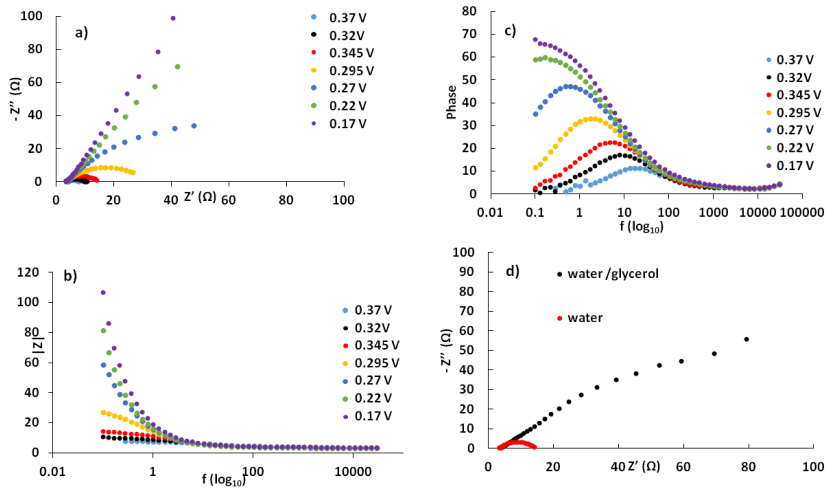

Fig. 22 *a) Nyquist diagram, Bode module (b) and Bode phase (c) of Pulse-Ni-foams recorded in KOH 0.1 M at several overpotential in OER region, (d) comparison of Nyquist plot recorded at Pulse-Ni-foams and PulseG-Ni-foams at η = 0.3455 V.*

The 2T time constant parallel model, consists in a slightly modified model originally proposed by Armstrong and Henderson (***Fig. 23b)***.[94] This model in terms of equivalent circuit is composed by the uncompensated resistance solution R_s in series with the parallel connection between the component connected to the transfer kinetics (constant phase element *CPE* and R_{ct}) and the faradic impedance of the reaction Z_f (C_p and R_p). The *CPE* represents a deviation from the purely double layer capacity C_{dl} behaviour related to surface in-homogeneity. Its impedance Z_{CPE} is described by the following equation[95]:

$$\boldsymbol{Z_{CPE} = \frac{1}{T(j\omega)^n}} \qquad \textbf{(21)}$$

Where T is a capacitance parameter (in F cm^{-2} s^{n-1}) and n is a parameter characterizing the rotation of the complex plane impedance plot. The double layer capacitance can be estimated from: [95]

$$\boldsymbol{T = C_{dl}^{n}\left(R_{s}^{-1} + R_{ct}^{-1}\right)^{1-n}} \quad \textbf{(22)}$$

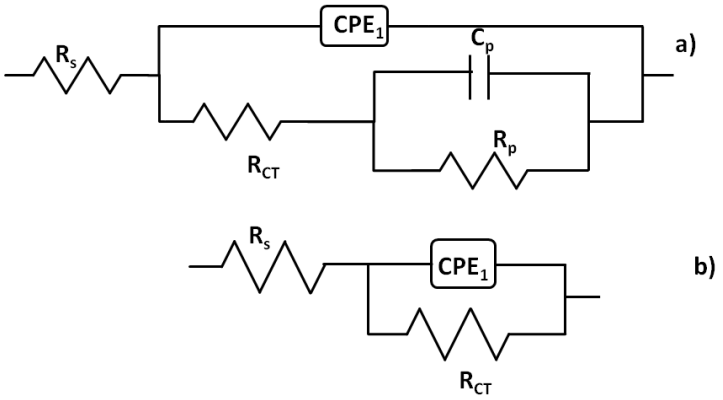

Fig. 23 *EEC used to model the EIS response of Pulse-Ni-foams and PulseG-Ni-foams at anodic η: a) two-time constant (2 T) parallel model and (b) one-time constant (1 T)*

The fitting quality was evaluated by the chi-squared (χ^2) values, which were in the range between 10^{-3} and 10^{-4}. ***Table 6*** shows the values of the parameters obtained from the fitting of the experimental data at two overpotential values.

As can be seen for *Pulse-Ni-foams* were employed the 1 T constant model, due the presence of one deformed semicircle in Nyquist plot. The reason is connected to the high vigorous bubble gas formation that causes interference, so that a poor define spectra is obtained. It can be observed that as the anodic overpotential increases, R_{ct} diminishes, indicating the increase of the kinetics rate of the process. The two constant time τ_1 *(*CPE_1*,* R_{CT}*),* τ_2 *(*C_p*,* R_p*)* (identified only for *PulseG-Ni-foams* samples) decrease with the overpotential, demonstrating also that both the Nyquist semicircles are connected to the faradic kinetics. Furthermore, the decrease of τ_2 with

the overpotential is connected to the increase and decrease of C_p and R_p element, respectively.

	PulseG-Ni-foams η (mV) = 295	*PulseG-Ni-foams* η (mV) = 325	*Pulse-Ni-foams* η (mV) = 295	*Pulse-Ni-foams* η (mV) = 325
$R_s(\Omega)$	3.674	3.621	3.568	3.541
$T/S*s^n$	0.01053	0.009711	0.01705	0.01601
n	0.5526	0.579	0.691	0.6956
$R_{ct}(\Omega)$	42.38	34.48	1.69	6.306
$C_{dl}(mF/cm^2)$	10.9	8.7	16	11.7
$C_p(mF/cm^2)$	2.033	4.48	----------	----------
$R_p(\Omega)$	230.4	24.19	----------	----------
τ_1 (s)	0.23	0.15	0.086	0.036
τ_2 (s)	0.23	0.054	----------	----------
X^2	$1.25*10^{-3}$	$4.30*10^{-4}$	$7.22*10^{-4}$	$5.683*10^{-4}$

Table 6 *ECC parameters obtained from the fitting of the EIS spectra at anodic η =325 and 295 mV for Const-Ni-foams and ConstG-Ni-foams, recorded in KOH 1 M.*

Fig. 24 shows the Nyquist diagram recorded at *Const-Ni-foams* and *ConstG-Ni-foams* in *HER* region: two semicircles can be appreciated.
Similarly, to the Nyquist impedance response in *OER* region, it can be appreciated that the diameter of the semicircle at low frequencies considerably diminishes with the cathodic η, indicating a more vigorous hydrogen evolution with the η.
Also in the phase Bode plot two constant phase elements can be clearly identified, indicating a correspondence with two CPE/Capacitance elements of the EEC. Anyway, in case of high hydrogen evolution observed for *Const-Ni-foams* not always two constants phase element were identified (See ***Fig. 24d***). Similar EIS responses have been recorded by Choquette et al.[96,97] and I. H. Cardona et al.[33,34]

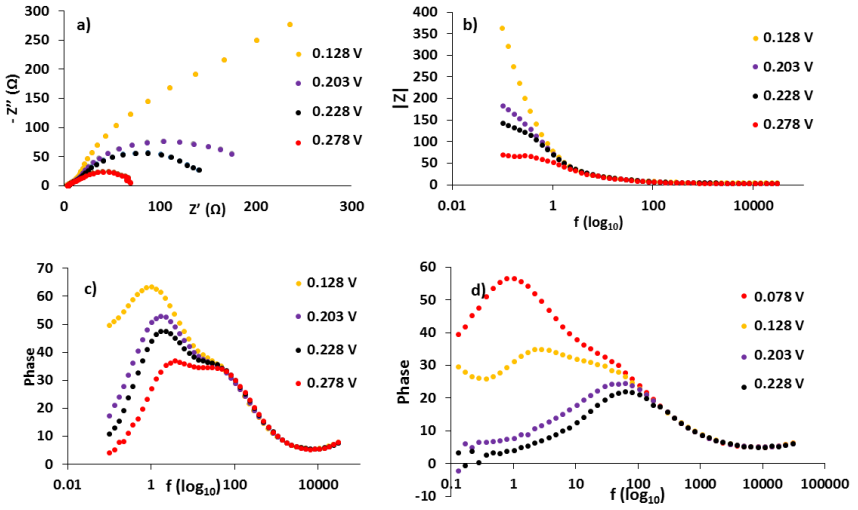

Fig. 24 *Nyquist diagram, Bode module (b) and Bode phase plot of ConstG-Ni-foams c), Bode phase plot of Const-Ni-foams (d) recorded in KOH 0.1 M at severalcathodic overpotential.*

Impedance complex plane plots of porous nickel electrodes at HER potentials found in literature typically show two distinct or overlapped semicircles.[97,98] Anyway, the second semicircle is not always visible. Chen and Lasia proposed a kinetic model containing two *CPE–R* elements, the so called *2 CPE model* (***Fig. 25***) to explain this phenomenon.[98]

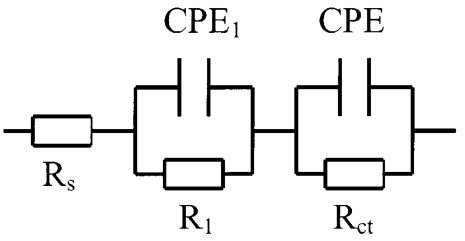

Fig. 25 *Typical 2CPE Model used for HER in porous electrodes.*

In this model the high frequency (HF) semicircle (CPE_1–R_1) is related to the porosity of the electrode and is independent of the kinetics of the faradic process. The low frequency semicircle (CPE–R_{ct}) is connected to the kinetics of the faradaic reaction of *HER*.

However, *HER* can also generate two semicircles, both related to the kinetics of the electrode process. By standard statistical analysis, it is very complicated to distinguish between the two models. The fitting of EIS spectra of the experimental data with the *2 CPE model* showed in ***Fig. 25*** has led to a not very good fitting of the experimental data.

As for the *OER*, the experimental data have been modeled with the 1T (***Fig. 23a***) or 2T model illustrated *in* ***Fig. 23b*** in case of one or two peaks characterizing the phase Bode plot.

Table 7 displays the values of the circuits elements, obtained from the fitting between the experimental and modelled predicted data, at several cathodic η. Also in this case a very good agreement between the experimental and the modelled data have been obtained with χ^2 always lower than $1.5* 10^{-3}$.

	PulseG-Ni-foams η (mV) = 178	*PulseG-Ni-foams* η (mV) = 203	*PulseG-Ni-foams* η (mV) = 228	*PulseG-Ni-foams* η (mV) = 278	*Pulse-Ni-foams* η (mV) = 0	*Pulse-Ni-foams* η (mV) = 203	*Pulse-Ni-foams* η (mV) = 228
$R_s(\Omega)$	4.158	4.083	4.12	3.805	3.705	3.658	3.87
$T/S*s^n$	0.001163	0.002052	0.001816	0.001942	0.003673	0.004154	0.002857
n	0.8	0.722	0.7281	0.7265	0.6922	0.6309	0.6737
$R_{ct}(\Omega)$	36.94	30.46	31.52	28.43	28.54	16.65	11.48
C_{dl} (mF/cm^2)	1.059	1.411	1.2	1.3	2.6	1.7	1.08
$R_p(\Omega)$	888	182.7	121.3	41.71	1251	----------	----------
C_p (mF/cm^2)	4.357	1.9	2.238	3.1	0.6175	----------	----------
τ_1 (s)	0.019566	0.021492	0.019669	0.018554	0.038	0.014	0.006
τ_2 (s)	1.934299	0.173602	0.135735	0.066694	0.39	----------	----------
X^2	$1.31*10^{-3}$	$2.686*10^{-4}$	$1.49*10^{-3}$	$4.22*10^{-4}$	$5.27*10^{-4}$	$8.232*10^{-4}$	$1.053*10^{-3}$

Table 7 *ECC parameters obtained from the fitting of the EIS spectra at several cathodic overpotentials for PulseG-Ni-foams and Pulse-Ni-foams, recorded in KOH 1M.*

It can been observed that R_{ct} decreases with the η for both the electrodes, indicating a faster kinetics reaction. It can be observed that also R_p decreases with η for *PulseG-Ni-foams.*

Analogous considerations can be done for the constant time at low frequencies τ_2 in case of *PulseG-Ni-foams* and τ_1 in case of *Pulse-Ni-foams.* Lower values of both τ_1 and R_{ct} have been recorded in case of *Pulse-Ni-foams:* this indicates that the hydrogen evolution reaction occurs at lower values of overpotential in this case. It worth to be notice that in case of *PulseG-Ni-foams*, τ_1 is almost constant with η; this can be explained considering that the first semicircle of Nyquist plot could takes account also of the geometry of the electrodes.

These results are in agree with the linear polarization analysis and they confirm the better electrocatalytic performance of *Pulse-Ni-foams.*

The higher catalytic activity toward *HER* and *OER* obtained for *Pulse-Ni-foams* with respect to *PulseG-Ni-foams* can be mainly due to the higher real surface area. Another factor to be considered is the morphology, the pore sizes and their distribution, which determine the accessibility of the electrolyte and the easiness of gas bubble release. *Pulse-Ni-foams* shows a more dendritic structure and longer pores than *PulseG-Ni-foams.*

Phenol degradation

As anticipated in the *The role of nickel based materials as catalysts* NiOOH sites react to form oxygen but they can also be exploited for the oxidation of organic pollutant present in the solution. At these sites the oxidation of organics reactants competes with oxygen evolution due to chemical decomposition of the oxides with higher oxidation state.[54, 78]

***Fig.* 26** displays the cyclic voltammetry of *Pulse-Ni-foams* in 0.1 M KOH solution with or without 28 ppm of phenol, chosen as model of organic compounds. As can be seen upon the addition of phenol both the anodic and cathodic peak currents slightly enhanced. This behaviour can be ascribed to the phenol oxidation by Ni hydroxides electro-generated at the anode surface by **(9)-(10)** as follows: [78]

$$\boldsymbol{NiOOH + phenol \rightarrow Ni(OH)_2 + product} \qquad \textbf{(23)}$$

A similar electrocatalytic mechanism has been used to explain the mechanism for the electrochemical oxidation of many organic compounds with Ni anodes in alkaline electrolyte. [50]

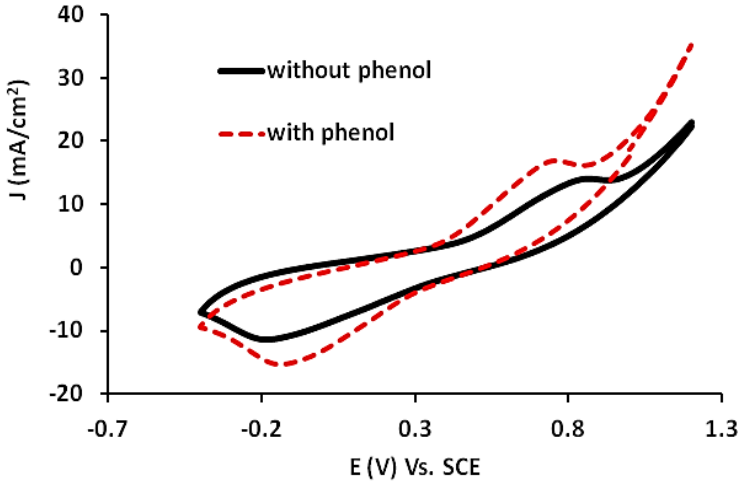

Fig. 26*: CV of Pulse-Ni-foams in the presence or absence of 28 ppm of phenol in 0.1M KOH.* [78]

Fig. 27 shows that the degradation process of phenol under galvanostatic and potentiostatic conditions.
Moreover, it can be noticed that the process follows a pseudo-first-order kinetics and the degradation rate is not affected by current density, under the operative conditions adopted, indicating a mass transfer controlled process.
As for the *OER* a greater surface area due to the porosity of the electrode allows the generation a great number of active sites for the formation Ni (II)/Ni (III) redox couples.

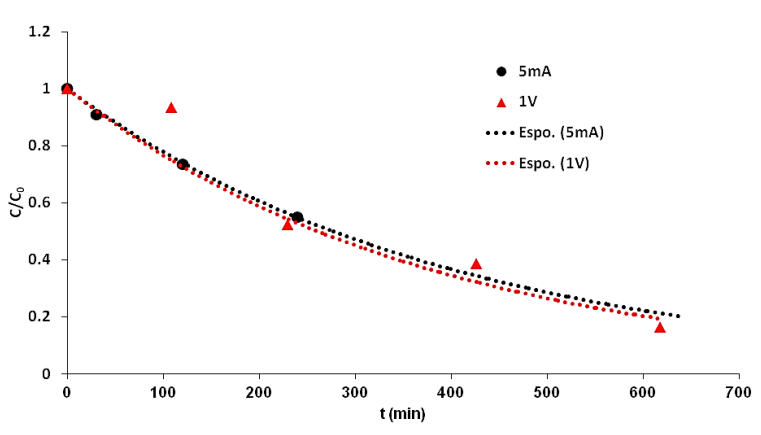

Fig. 27 *Trend of phenol concentration during oxidation at 1 V and 5 mA in 0.1M KOH by Pulse-Ni-foams.* [78]

2.4. Results: Niobium electrodes as substrates

2.4.1. Electrodeposition

As in the case of the BDD substrates, the freshly niobium electrodes were submitted to electrodeposition under potentiostatic conditions at E= 0.8 V.

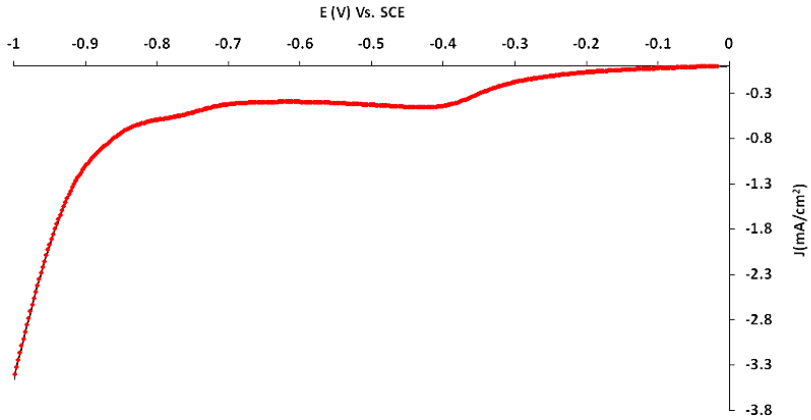

Fig. 28 *LSV recorded in a solution containing NiSO4 0.5 M, CuSO4 0.005 M and H_3BO_4 0.5 M at a niobium electrode (v= 5mV s^{-1}).*

Before the electrodeposition a linear sweep voltammetry has been performed in the electrodeposition solution at 5 mV s^{-1} to favorite a slow deposition and the formation of a thin film onto niobium surface (***Fig. 28***). As can be seen at -0.3 V the current increases with the beginning of the copper deposition and at the onset nickel deposition potential (around V=- 0.72 V) the current enhances again, due to the beginning of the nickel electrodeposition. Between E= -0.72 V and E= -0.82 V both nickel and copper can be electrodeposited and above E= -0.82 jjffV hydrogen evolution reaction takes place.

Fig. 29 displays the SEM image of the Ni-Cu systems onto the niobium surface: a homogeneous distribution of the metallic elements on the surface can be observed.
Differently from the deposit at BDD, a smoother metallic layer is obtained at niobium substrates, due to different roughness of BDD and Nb foils.

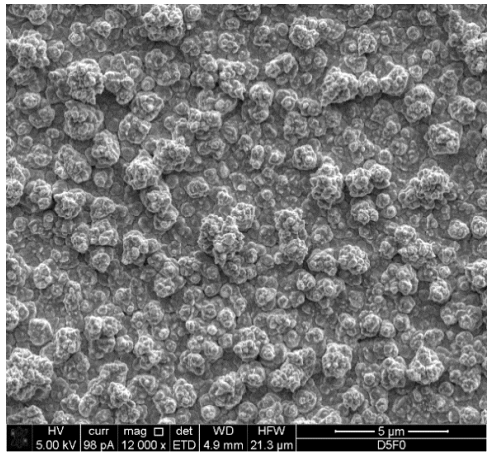

Fig. 29 *SEM image of Ni- Cu onto niobium substrates.*

The Auger mappings of copper and nickel represented in ***Fig. 30*** in green and red respectively, reveal essentially an homogeneous distributions of each element on the niobium surface with some copper agglomerations which characterized the surface.

The chemical composition of the film calculated by EDX analysis indicates a molar fraction of 30% of copper and 70% of nickel. A 30% more of nickel has been found with respect to the BDD substrates; this means that at potential of -0.8V different percentage compositions can be achieved using different substrates and that probably nickel deposition starts at lower potential onto niobium surfaces. The recorded charge during the electrodeposition experiment was around 2.5 C/cm^2: around the 40% less than that recorded at BDD substrates.

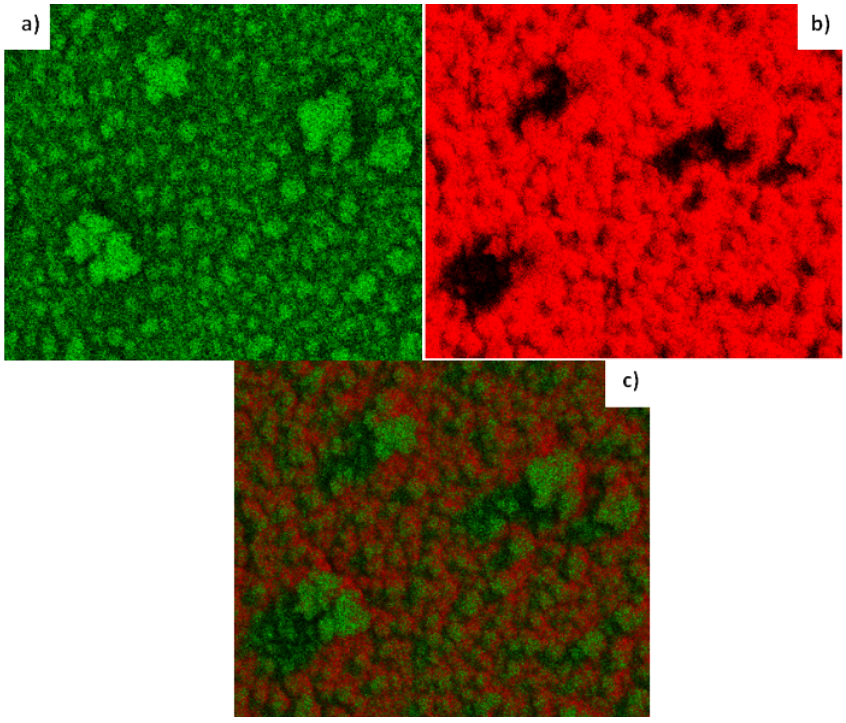

Fig. 30 *Auger mappings of Cu (a) and Ni (b) and both of Ni and Cu of the Ni-Cu deposits onto niobium substrates.*

2.4.2. Electrochemical dissolution and characterization

As reported in *Synthesis* the electrochemical dissolution experiments were carried out using different percentages of glycerol and ethyl glycol, in order to evaluate the effect of the solvent viscosity on the morphology and composition of the electrodes.
Fig. 31 shows a SEM image of a copper-nickel system submitted to anodic dissolution in aqueous solutions at pulsed voltage using a corrosion and relaxation time of 1 s and 5 s, respectively (NPt_1t_5).
A homogeneous and high porous structure with a regular tubular pores shape has been achieved, with pores diameters in the range of 200-350nm.
No significant morphology differences have been obtained changing the solvent during the etching.

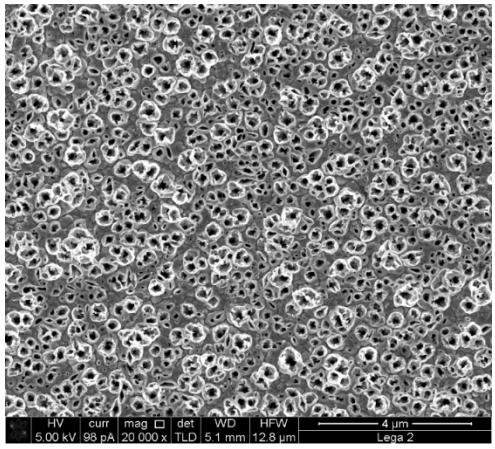

Fig. 31 *SEM image of Ni-Cu systems submitted to anodic dissolution at pulsed voltage (V_{corr}= 0.5V, t_{corr}=1 s; V_{relax}=OCP; t_{relax}=5 s) in aqueous solution (NPt_1t_5 samples).*

No significant morphology differences have been obtained changing the solvent during the etching.
This means that the water plays the main role during the anodic dissolution experiment. A more regular pores shape and size seem characterize these samples with respect the BDD pulsed samples developed with the same experimental conditions (See *Electrochemical anodic dissolution*).

Fig. 32 shows the cross section of a sample prepared using the same experimental conditions. The average pores thickness was estimated as 531 nm.

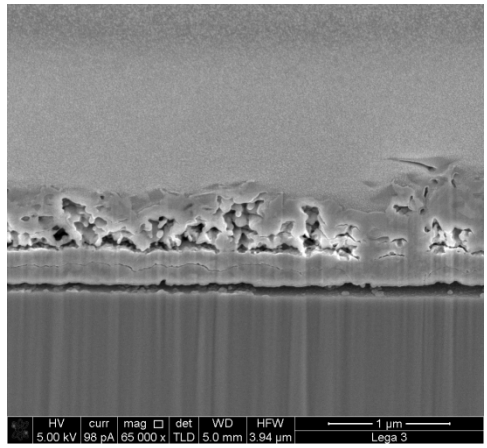

Fig. 32 *Cross section of Ni-Cu systems submitted to anodic dissolution at pulsed voltage (t_{corr}=1s and t_{relax}=5s) in aqueous solution (NPt_1t_5 samples).*

Fig. 33 displays an example of a J/t curve recorded during an anodic dissolution experiment: the dissolution current remarkably increases in initial period, and then gradually decreases after reaching a maximum value and in the final period tends to level off at a very low value.

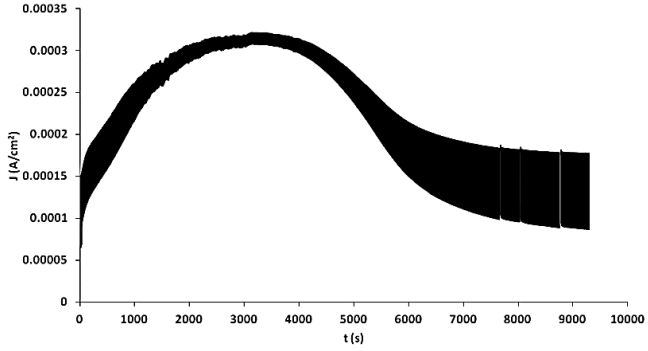

Fig. 33 J*/t curve of Ni-Cu systems submitted to anodic dissolution at pulsed voltage(t_{corr}=1s and t_{relax}=5s).*

The current increases at the starting phase can be due to the growth of active sites due to removal of copper of the surface layer and to the formation of the passive oxide layer onto nickel.
The decrease of the dissolution current instead can be mainly caused by both the reduction of copper amount in the Ni-Cu deposit and to the Ni passivation phenomena.[99]
The recorded charge after the corrosion was around the 30% of the electrodeposition charge: the dissolved content of copper from the Ni-Cu deposits results almost corresponding to the amount of copper present in the deposits themselves.
The change of viscosity does not seem affect neither the chemical composition: in each case, a high purity level of the samples has been achieved, with copper amounts in a range of 4-6%.
In the following anodic dissolution experiments the pulsed voltage was modulated between different corrosion and relaxation times and then two different ratio between the corrosion and relaxation time were employed (See *Synthesis*). The aim was to evaluate the optimal time to dissolve and rearrange during the corrosion process, for copper and nickel atoms, respectively. Then, the purpose was to understand how these choices affected different phenomena: the passivation of the nickel surface, the migration of the copper ions from the electrode/electrolyte interface to the bulk of the solution and the dissolution process itself.
Fig. 34 shows the SEM images of the samples obtained using different corrosion conditions. (For the names of the samples refers to *Synthesis*). It can be observed that a high and homogeneous porous structure has been achieved in each reported case, with different morphologic features depending on the experimental conditions. In particular NPt_1t_5 ***(Fig. 34a)*** and $NPt_{0.1}t_{0.5}$ ***(Fig. 34b)*** appear characterized by a similar morphology, although the first presents a higher pores density and homogeneity of the pores size and shape. It worth to underline that these samples were prepared using the same ratio between the corrosion and relaxation time (t_{corr}/t_{relax}). The other sample realized using the same corrosion t_{corr} and relaxation time t_{relax} ($NPt_{0.01}t_{0.05}$ in ***Fig. 34c)*** is instead characterized by a poor pores density. This can be ascribed to the use of both the lowest t_{corr} and t_{relax}: probably not sufficient enough to allow both the corrosion and atomic redistribution. It is interesting to notice a quite similar morphology between the samples

prepared using the lowest t_{corr}/t_{relax} (NPt_1t_{50} in ***Fig. 34d***, $NPt_{0.1}t_5$ in ***Fig. 34e***, $NPt_{0.01}t_{0.5}$ in ***Fig. 34f).***

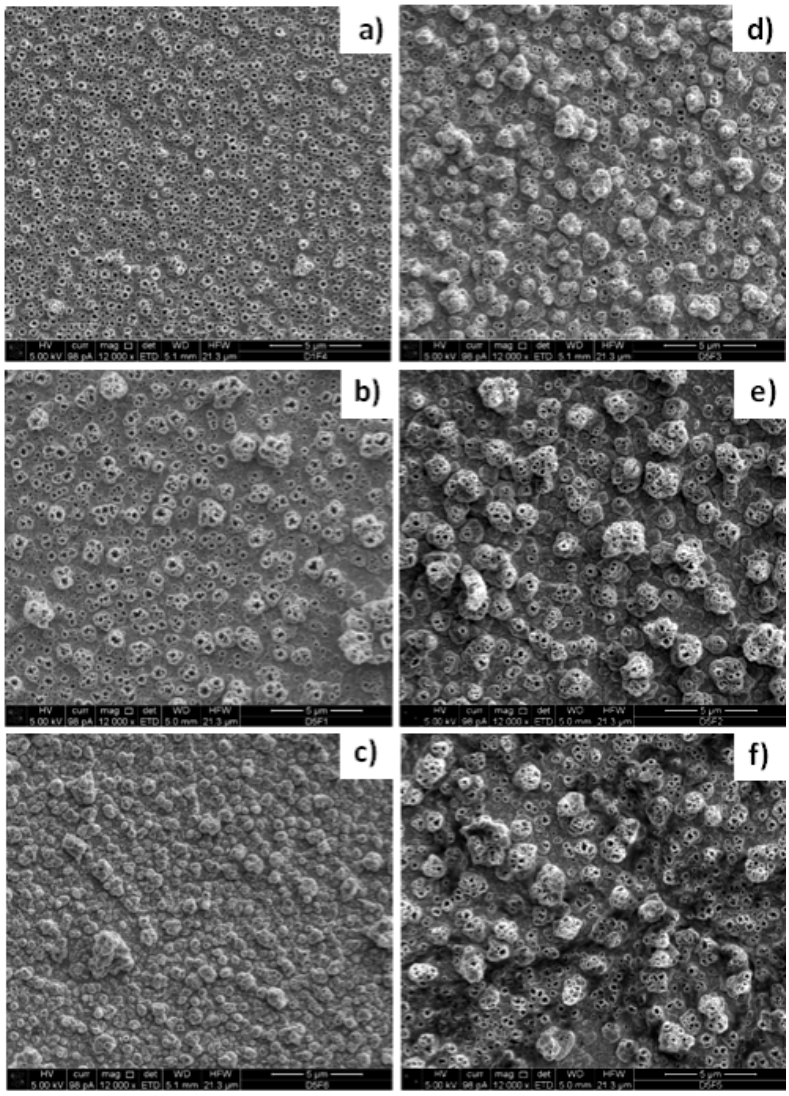

Fig. 34 *SEM images of samples submitted to anodic dissolution using: a)* t_{corr}*=1s;* t_{rilass}*=5s:* NPt_1t_5 *(b)* t_{corr}*=0.1 s ;* t_{rilass}*=0.5s:* $NPt_{0.1}t_{0.5}$ *, c)* t_{corr}*=0.01 s ;* t_{rilass}*=0.05s:* $NPt_{0.01}t_{0.05}$*, d)* t_{corr}*=1 s ;* t_{rilass}*=50 s:* NPt_1t_{50}*, e)* t_{corr}*=0.1s ;* t_{rilass}*= 5s :*$NPt_{0.1}t_5$ *f)* t_{corr}*=0.01 s ;* t_{rilass}*=0.5s:* $NPt_{0.01}t_{0.5}$*.*

Observing ***Table 8***, it can be appreciated that decreasing the t_{corr} and keeping constant t_{relax} the pores diameter diminishes for each couple of times (See NPt_1t_5/***Fig. 34a*** and $NPt_{0.1}t_5$/***Fig. 34e*** and $NPt_{0.1}t_{0.5}$/***Fig. 34b*** and $NPt_{0.01}t_{0.5}$/***Fig. 34f***), although a slightly and progressive decrease of the purity of the samples was found. Between these couples of samples those with the lowest t_{corr} are also characterized by the highest copper amount. This can be attributed to the fact that the atoms require a time enough sufficient to allow the removal of copper itself (See $NPt_{0.01}t_{0.05}$ in ***Fig. 34 c***).

name	t_{corr}	t_{relax}	t_{corr}/t_{relax}	d (nm)	Wt_{Ni}	Wt_{Cu}
NPt_1t_5	1	5	0.2	200-350	90	6.42
$NPt_{0.1}t_{0.5}$	0.1	0.5	0.2	140-300	86.3	8.6
$NPt_{0.01}t_{0.05}$	0.01	0.05	0.2	50-150	76.5	19.5
NPt_1t_{50}	1	50	0.02	170-250	80.81	14.43
$NPt_{0.1}t_5$	0.1	5	0.02	170-250	88.87	8.37
$NPt_{0.01}t_{0.5}$	0.01	0.5	0.02	70-250	82	11

Table 8 *Average diameters d (nm) and molar fractions of Cu and Ni (W_{Cu} and W_{Ni}) of porous nickel electrodes produced using different t_{corr} and t_{relax} during the anodic pulsed voltage dissolution experiments.*

Conversely, increasing the t_{relax} and keeping constant the t_{corr} it can be appreciated a decrease of the pores size in the case of the use of t_{corr} of 1 s (NPt_1t_5 in ***Fig. 34a*** and NPt_1t_{50} in ***Fig. 34d***) and 0.1 s ($NPt_{0.1}t_{0.5}$ in ***Fig. 34b*** and $NPt_{0.1}t_5$ in ***Fig. 34e***). This is not verified in the case of a t_{corr} of 0.01 s; but anyway these samples are prepared with both the lowest t_{corr} and t_{relax}, which have led to a very low porosity and the highest copper amount.
This can be explained considering that just the absolute value of the t_{corr} and t_{relax} are not sufficient parameters to control the pores sizes and the porosity of the samples, but a combination of more factors should be considered.
As previously discussed, one of the parameter that gives us indications about the porosity is the real surface area of the electrodes. Then, as for the BDD electrodes, capacitive measurements have been performed in order to

determine the C_{dl} and the roughness R_{ough}, which are strictly connected to the real surface area of the electrodes. Anyway, also performing EIS measurements is possible to estimate these parameters. Hence, as this purpose, EIS measurements were made at OCP value in solutions containing KOH 1 M.

As an example in ***Fig. 35*** is reported the Nyquist and Bode plot of $NPt_{0.01}t_{0.5}$. Similar electrochemical responses have been recorded for the other samples.

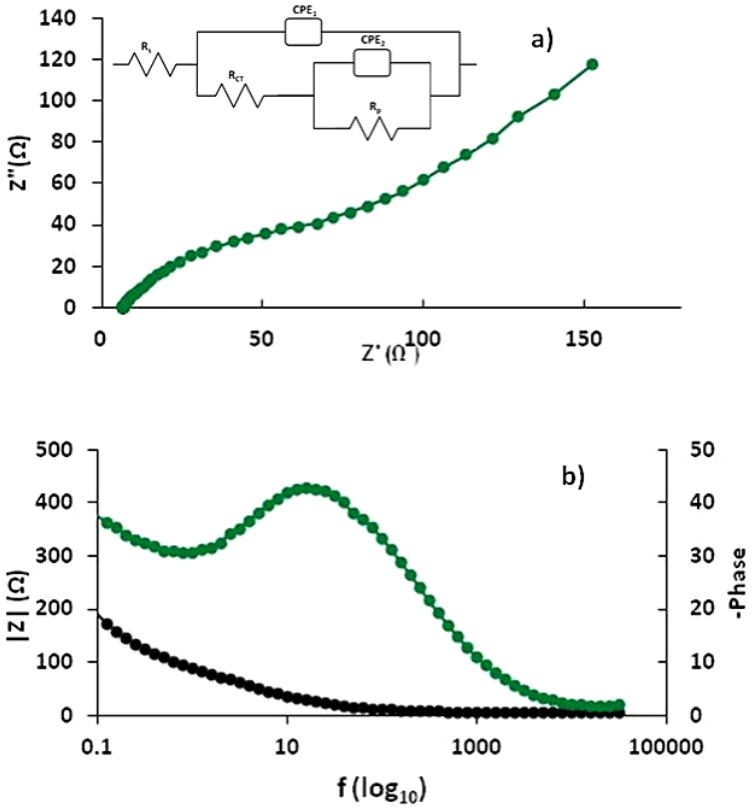

Fig. 35 *Nyquist and Bode EIS spectra of measured data for the* $NPt_{0.01}t_{0.5}$ *recorded at OCP value in KOH 1 M. The inset shows the ECC used to model the experimental data.*

The Nyquist diagram shows the presence of one semicircle and the beginning of a second one (a nearly straight line): the capacitive loop at high frequencies is typically associated to the charge transfer kinetics and

the second to the mass transport limit. The electrochemical equivalent circuit (EEC) that has been proposed to model the electrical behavior of the electrodes is the 2T time constant parallel model, typically used for porous and rough electrodes (See inset in ***Fig. 35***). [39] The *EEC* is composed by two parallel *CPE-R* circuit elements in series with the resistance of the solution R_s. The CPE_1-R_{ct} element describes the behavior of the system at high frequencies and it is composed by the charge transfer resistance R_{ct} and the constant phase element CPE_1, which impedance allows to obtain C_{dl} through **(21)-(22)**.The CPE_2 element instead can be associated to the diffusion phenomena inside the pores. The impedance results concerning the C_{dl} interpreted with *ZSimpWin* software are reported in ***Table 9.*** This table reports also the roughness factors R_{ough} obtained considering the C_{dl} of a smooth nickel electrode as 20 μF/cm^2 .[37,98,100] For comparison also the data obtained for the Cu-Ni deposits have been reported. A good agreement between experimental and predicted data has been obtained for all the experimental conditions, with χ^2 lower than 10^{-3}. As can be seen from the table the groups of samples prepared using a lower ratio between the times present a higher C_{dl} and then of roughness. Moreover, fixing the ratio between the corrosion and relaxation time an increase of the porosity is recorded with the decrease of the corrosion time. This is not verified in the case of a very low density of pores (See ***Fig. 34c***).

name	t_{corr}	t_{relax}	t_{corr}/t_{relax}	C_{dl} (μF/ cm²)	R_{ough}
deposit	--------	----------		260	13
NPt_1t_5	*1*	*5*	*0.2*	430	21.5
$NPt_{0.1}t_{0.5}$	*0.1*	*0.5*	*0.2*	1438	74.6
$NPt_{0.01}t_{0.05}$	*0.01*	*0.05*	*0.2*	*492*	*24.6*
NPt_1t_{50}	*1*	*50*	*0.02*	*1221*	*61*
$NPt_{0.1}t_5$	*0.1*	*5*	*0.02*	*1526*	*76.5*
$NPt_{0.01}t_{0.5}$	*0.01*	*0.5*	*0.02*	*2123*	*106*

Table 9 *C_{dl} values of nanoporous nickel electrodes prepared using different t_{corr} and t_{relax}, interpreting the experimental impedance data with ZView software by the equivalent circuit shown in the inset in Fig. 34.*

As widely discussed in *Background*, since the real surface area is a determining factor that affects the properties of the electrodes, different

kind of electrodes characterized by a different roughness have been selected in order to investigate their electrocatalytic performance towards *HER* and *OER*. For the same purpose, the photoactivity of the samples presenting the highest porosity compared to a smooth nickel electrode have been also studied.

2.4.3. Electroactivity

Two kind of samples (NPt_1t_5, $NPt_{0.1}t_{0.5}$) representative of two different porosity range, have been selected in order to investigate their electrocatalytic performance towards *HER* in alkaline solutions. Similarly, the samples NPt_1t_5 and $NPt_{0.1}t_5$ have been designated to study their behavior as electrocatalysts for *OER*. Moreover, the electroactivity of Ni-Cu deposits and $NPt_{0.01}t_{0.05}$ have been also reported as comparison. As for the nickel porous electrodes prepared using BDD as substrates for the electrodeposition, the study has been performed by means of LSV in basic solutions at pH=14, at anodic and cathodic η for *HER* and *OER* respectively.

Observing the steady-state polarization curve in ***Fig.36*** it is evident that the onset *HER* overpotential decreases when the C_{dl} of the electrodes assumes higher values and then the porosity of the electrodes increases. Moreover, it can be appreciated that $NPt_{0.01}t_{0.05}$ although exhibits a roughness R_{ough} comparable to that of NPt_1t_5, displays a lower *HER* onset η*:* fact that can be ascribed to the high copper amount in this sample. Indeed, studies which demonstrated the improved *HER* electrocatalytic activity of Ni-Cu alloys are reported in literature.[101]

Table 10 shows the kinetic parameters estimated from the linear polarization curve presented in ***Fig.36*** in form of Tafel plot, using **(18)**. About the mechanism of the reactions a slope in the range of 100-140 mV/dec was recorded: values in agree with the results present in literature for nickel based electrodes, which indicate that *Volmer-Heyro*vosky reaction is the rate determining step *rds*.[43,44]

Comparable β values have been found for *Pulse-Ni-foams* realized onto BDD substrates (See *Oxygen and hydrogen evolution reactions*).

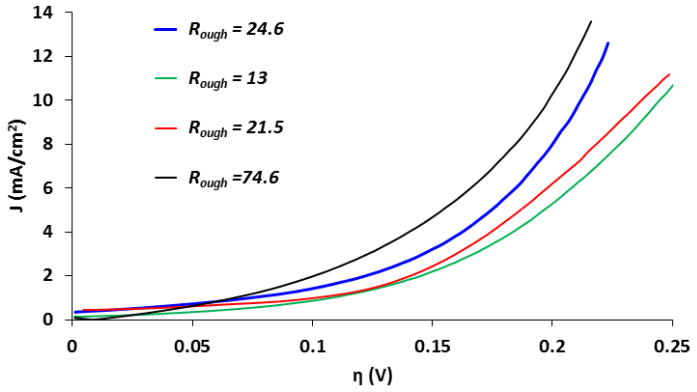

Fig. 36 *Steady-state polarization curve for HER on Ni-Cu deposits (in green), NPt_1t_5 (in red), $NPt_{0.01}t_{0.05}$ (in blue), $NPt_{0.1}t_{0.5}$ (in black) recorded at cathodic η in KOH 1 M. A sweep rate of 0.5 mV s^{-1} was employed.*

Name	R_{ough}	I_o (mA/cm²)	I_{or} (μA/cm²)	β (mV/dec)	η_{10} (mV)
Ni-Cu deposit	13	0.14	10.78	100	245
NPt_1t_5	21.5	0.2	9.54	125	236
$NPt_{0.01}t_{0.05}$	24.6	0.28	11.38	140	213
$NPt_{0.1}t_{0.5}$	74.6	0.35	4.7	140	200

Table 10 *β, i_o, i_{or}, η_{10} obtained for the samples characterized by different values of R_{ough}. The parameters have been calculated in the HER overpotential range $0.15<|\eta|<0.25$ V.*

The lowest values of η_{10} have been obtained for the samples presenting the highest R_{ough} (samples with C_{dl} = 1438 μF/cm^2). Similar considerations can be done considering the i_o values; in addition it can be appreciated that i_o and η_{10} increases and decreases with the roughness of the electrodes, respectively. Comparable values of η_{10} and i_o have been obtained with

respect the Ni-porous electrodes synthesized onto BDD substrates when the same experimental conditions were employed. (See *Oxygen and hydrogen evolution reactions)*.

Moreover, like for the *Pulse-Ni-foams and PulseG-Ni-foams*, it is clear that higher values of i_o compared with that of a nickel smooth electrode (i_o= 0.07 μA /cm^2) have been obtained in all the investigated electrodes.[91]

Normalizing the exchange current densities for the active surface area of the electrodes, the real exchange current density i_{or} was calculated.

As can be appreciated i_{or} higher of two and three orders of magnitude have been achieved for all the investigated electrodes compared to a smooth nickel electrode. This can be attributed to the intrinsic properties of the porous electrodes in case of NP_1t_5 and $NPt_{0.1}t_{0.5}$, due to the morphologic structure conferred by the electrochemical dealloying, that can either increases the active area accessible and improve the electron mobility.

The higher i_{or} value of NP_1t_5 with respect $NPt_{0.1}t_{0.5}$ suggests that the inner porous surface of $NPt_{0.1}t_{0.5}$ is not totally exploitable for *HER*; this suggest that the pores size, shape and distribution play a role in the resulting electrocatalytic performance.

Concerning Ni-Cu deposits instead, the enhancement of i_o compared to a smooth nickel electrode can be connected essentially to the presence of a rough dual system composed both from Ni and Cu. The highest i_{or} value achieved for $NPt_{0.01}t_{0.05}$ suggests essentially that both the porous framework and the copper amount affect the overall electroactivity of the electrodes.

Fig. 37 displays the steady- state polarization curve recorded in anodic region in alkaline solutions for different kind of electrodes. The figure shows that the overall electrocatalytic activity towards *OER* (See the onset overpotential) increased in the order Ni-Cu deposits < NPt_1t_5 < $NPt_{0.01}t_{0.05}$ < $NPt_{0.1}t_5$.

Observing the kinetic parameters in ***Table 11***, estimated from the Tafel plot, it can be appreciated that the exchange current density calculated at low overpotential i_0 (0.25<η 0.3 V) and high overpotential i_{o2} (0.3<η 0.4 V) follows mainly the same increasing trend with respect the R_{ough} that has been observed for *HER*. Anyway, comparing i_o and i_{o2} of NPt_1t_5 and $NPt_{0.01t0.05}$ can be appreciated the opposite behaviour; this can be ascribed to the different composition of the material.

It is interesting to note that instead η_{10} decreases progressively with the R_{ough} of the samples. Moreover, comparing i_o with the typical values obtained for a smooth nickel electrode at both η_{low} and η_{high} a remarkable enhancement associated to the increase of the surface area was found. In particular, an increase of five and one/two orders of magnitude for η_{low} and η_{high} has been observed, respectively.[44]

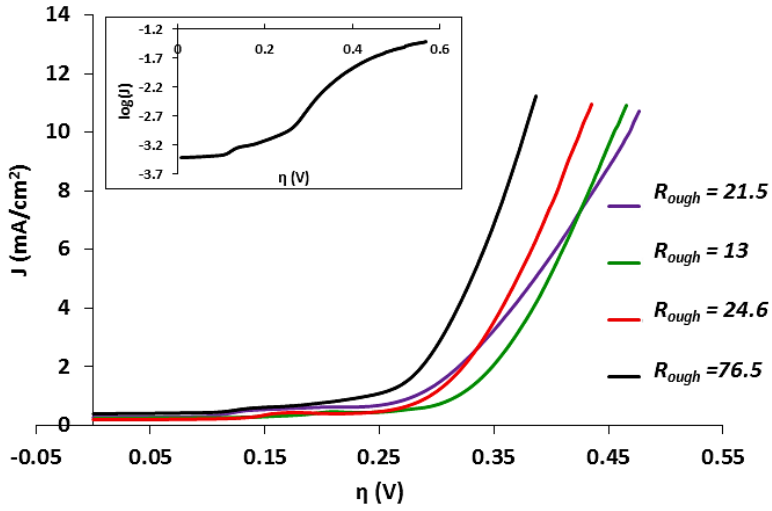

Fig. 37 *Steady-state polarization curve for OER on Ni-Cu deposits (in green), NPt_1t_5 (in violet), $NPt_{0.01}t_{0.05}$ (in red), $NPt_{0.1}t_5$ (in black) recorded at anodic η in KOH 1 M. A sweep rate of 0.5 mV s^{-1} was employed. In the inset, the Tafel plot of $NPt_{0.1}t_5$ is shown.*

Similar results have been found also for *Pulse-Ni-foams*. Furthermore, comparing the real exchange current density at η_{low} (i_{or1}) a remarkable increase with respect to a smooth nickel electrode is still observed. This can be ascribed to the intrinsic properties of the samples submitted to electrochemical dealloying and to the chemical structure of the electrodes surface. Comparable values of i_{or2} have been instead found for all the cases analysed. This suggests that at η_{high} the gas evolution is too vigorous to allow to fully exploiting the overall surface area. Concerning the mechanism reactions driving the *OER* two Tafel slope regions ranging from 80-90 mV/dec for η_{low} (0.28-0.35V) and 130-165 mV/dec for η_{high} (0.35-0.4V) can be distinguished. As an example in the insert of ***Fig. 37*** the Tafel

plot of the $NPt_{0.1}t_5$ is reported. As for the *Pulse-Ni-foams* a mechanism based on the desorption of oxygen molecules according an electrochemical desorption can be assumed. This results are in agree with other *OER* studies present in literature about nickel based electrodes.[92]

Name	R_{ough}	I_o ($\mu A/cm^2$)	β_1 (mV/dec)	I_{or1} ($\mu A/cm^2$)	I_{o2} (mA/cm^2)	β_2 (mV/dec)	I_{or2} ($\mu A/cm^2$)	η_{10} (mV)
Ni-Cu deposit	13	1	80	0.08	0.015	130	1.5	456
NPt_1t_5	21.5	6.3	90	0.2	0.06	165	3	460
$NPt_{0.01}t_{0.05}$	24.6	2.5	90	0.1	0.018	150	1	423
$NPt_{0.1}t_{0.5}$	72.5	7	90	0.1	0.2	165	3	370

Table 11 *β_1, i_o, i_{or1}, β_2, i_{o2}, i_{or2}, η_{10} of samples characterized by different values of R_{ough} and chemical composition. The parameters β_1, i_o, i_{or1}, have been calculated in the OER range between $0.28<\eta<0.35$ V; β_2, i_{o2}, i_{or2} between $0.35<\eta<0.4$ V.*

2.4.4. Photoelectrochemical measurements

In order to investigate the use of the developed samples as photocathodes, they were submitted first to potential cycling over 150 times, in basic solution (*See Photoelectrochemical measurements*) to allow the conversion of Ni(II) to Ni(III) oxides. After that the samples were undergone to thermal annealing at 500 ° C in order to permit the conversion of Ni(III) to NiO. Indeed, as reported in Background, a minimum temperature of 300° C is required to permit the crystallization and transformation to $Ni(OH)_2$ and NiOOH to NiO form.[102]
Anyway, C. Hu et al. reported that at 300 ° C only metallic amorphous Ni was measured by XRD analyses, while increasing the annealing temperature NiO crystallites size increases: at 500 ° C NiO has been determined as the dominant phase. [65] Since a high crystallinity guarantees a low recombination of charge carriers a temperature of 500 ° C was adopted in order to increase the photocurrent density.[103]

Fig. 38a shows the cathodic photocurrent response after annealing of oxide $NPt_{0.01}t_{0.5}$ *(Ox-*$NPt_{0.01}t_{0.5}$*)* in KNO_3 0.1 M aqueous electrolyte, in comparison with a smooth nickel electrode undergone to the same thermal treatment (*NiO* in ***Fig. 38b***).

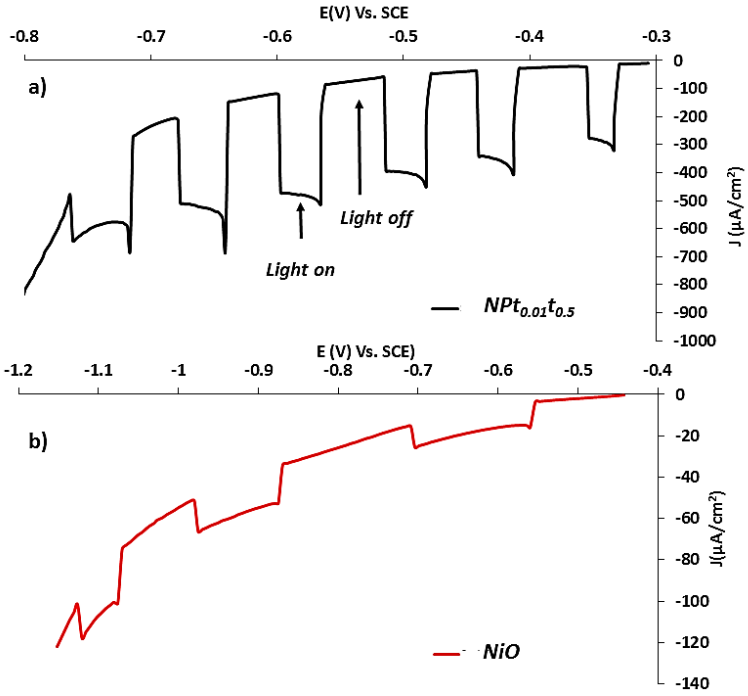

Fig. 38 *LSV of (a) smooth Ni and (b)* $NPt_{0.01}t_{0.5}$ *after thermal annealing at 500 C ° recorded in 0.1 M* KNO_3 *aqueous electrolyte. The potential was ramped (5 mV* s^{-1}*) from the OCP to -1.2 V. Data were recorded under dark and irradiation condition (AM O filter).*

As can be seen negligible current values are observed under dark conditions, while under irradiation a remarkable increase of the recorded photocurrent is observed for both the cases.

Moreover, it can be appreciated that both the samples display the typical photoelectrochemical behaviour characterizing the p-type semiconductors.[104] It worth to be noticed the different axis scale used for the current density to represent the photocurrent answer of the two

samples: an outstanding increase of the photocurrent of *Ox-NPt*$_{0.01}t_{0.5}$ compared to *NiO* is appreciated.

Table 12 shows different parameters extrapolated from the linear sweep voltammetry shown in ***Fig. 38*** as well as the OCP recorded under dark OCP_{dark} and illumination OCP_{light}.
The R_{ough} of *NiO* was estimated as illustrated in the Chapter *Electrochemical anodic dissolution and Characterization*, using the same method employed for $NPt_{0.01}t_{0.5}$.
As can be seen the more positive OCP value under illumination conditions with respect the dark characterizing the p-type oxide semiconductor is present for both the electrodes. The OCP_{dark} of $NPt_{0.01}t_{0.5}$ is more than NiO. This is an interesting result since the efficiency of the p-type photocathodes is limited by the intrinsically low OCP.[105]
The photocurrent generated at around 100 mV from the OCP for *Ox-NPt*$_{0.01}t_{0.5}$ and *NiO* was -408 μA cm^{-2} (nominal area) and -15 μA cm^{-2} respectively.
It is obvious that the remarkable increase of the photoactivity of *Ox-NPt*$_{0.01}t_{0.5}$ is mainly caused by the enhanced surface area.
Anyway, the two samples present a different dark current I_{dark} at the same fixed η. It is interesting to evaluate the increment in photocurrent with respect the I_{dark} of each sample.
Table 12 displays that the difference ΔI ($I_{dark} - I_{light}$) shown by *Ox-NPt*$_{0.01}t_{0.5}$ is around 32 and 20 times higher than that of *NiO* at 100 and 400 mV from the OCP value. *Ox-NPt*$_{0.01}t_{0.5}$ exhibits a photocurrent increment ($\frac{I_{dark}-I_{light}}{I_{dark}}$) with respect the bias value of 13.5 while *NiO* of only 3.5. In order to understand if the overall of the real surface area of *Ox-NPt*$_{0.01}t_{0.5}$ was photoactive the parameter ΔI was estimated also with respect the real surface area of the electrodes (ΔI_r). It is clear that the increase of the photocurrent is mainly caused by the enhancement of the surface area and that the surface is probably fully exploited for increasing the photocurrent. Anyway, $NPt_{0.01}t_{0.5}$ presents a higher photocurrent compared to NiO, also normalizing the photocurrent with respect their real surface area (See ΔI_r).
This suggests that also the particular morphology and structure of the nanoporous nickel electrodes fabricated with the employed method in this

PhD study plays a role in improving the overall photoelectrochemical performance.

	NiO	Ox-NPt$_{0.01}$t$_{0.5}$
R_{ough}	7.6	106
OCP_{dark} (mV)	-441	-300
OCP_{light} (mV)	-390	-240
$I_{dark}(\eta_{OCP}$= 100mV) (μA/cm$_2$)	-3.3	-28
$I_{light}(\eta_{100mV})$ (μA/cm$_2$)	-15	-406
ΔI (μA/cm$_2$)	11.7	378
Δi_r (μA/cm^2)	1.56	3.56
$I_{dark}(\eta_{400mV})$ (μA/cm^2)	-33.9	-267
$I_{light}(\eta_{400mV})$ (μA/cm^2)	-53.5	-677
$\Delta i_{light-dark}$ (μA/cm^2)	19.6	400
Δi_r (μA/cm$_2$)	2.58	3.77

Table 12 *OCP_{dark}, OCP_{light}, I_{dark} and I_{light} recorded at 100 and 400 mV from the OCP_{dark}) for NiO and Ox-NPt$_{0.01}$t$_{0.5}$. ΔI is calculated as I_{light} - I_{dark} both respect the nominal and real surface area of a Ni smooth electrode and NPt$_{0.01}$t$_{0.5}$.*

2.5. Conclusions

Nanoporous nickel films have been successfully fabricated on both BDD and niobium as substrate, by an electrochemical easy method based on the electrochemical selective anodic etching of copper from Ni-Cu deposits.
The stripping of copper during the electrochemical etching results in the formation of nanoporous nickel electrodes characterized by an essentially open pores structure.
Depending on the conditions adopted for the etching, different surface area were obtained, characterized by different pores sizes (ranging from 70 to 400 nm), shapes and copper amount (from 5 to 20%).
In particular, it was demonstrated that modulating the potential pulses between different corrosion and relaxation times is possible to tune the pores sizes and the roughness of the electrodes. Starting from the same electrodeposition conditions the widest surfaces (R_{ough} in the range of 70-100) have been mainly obtained using a lower ratio between the corrosion and the relaxation time (at a fixed corrosion time). Anyway, these electrodes reported higher copper amount.
It was demonstrated that the prepared samples with this approach can be effectively employed as anodes for *OER* as well as cathodes for *HER* in alkaline solutions. The as-prepared nanoporous nickel electrodes exhibited much enhanced electrocatalytic activity for *HER* and *OER* in comparison with a commercial smooth nickel electrode, resulting mainly from their enhanced surface area.
Values of exchange current density until four orders of magnitude higher for *HER* compared to a smooth nickel electrode have been recorded. Concerning *OER* exchange current density until five and two orders of magnitude more for low and high overpotential were obtained.
It was also proven that the real surface area is mainly fully exploited for the faradic processes analyzed, although differences depending on the pores morphology and the overpotential applied have been found.
Values of real exchange currents density for *HER* and *OER* higher than smooth Ni electrodes (one order of magnitude for *HER* and until three for *OER* at η_{low}) have been also found. The results show also that the chemical composition of the samples affects the electroactivity. In particular, the electrocatalytic behavior towards *HER* appears positively affected by the presence of copper in the nickel porous electrode.

Moreover, evidences about the effectiveness of the as- prepared samples as anodes for degradation of organic compounds in alkaline solutions, were reported. The removal of phenol was achieved under potentiostatic and galvanostatic conditions. The degradation occurred in the region of oxygen evolution, confirming that the oxidation is mediated by surface oxides electrogenerated. The kinetics observed was very fast, being the mass transfer the controlling step.

Finally, it was demonstrated that after an annealing treatment the porous electrodes can be also employed as photocathodes in neutral solutions.

The samples showed a p-type semiconductor behaviour, typical of photocathodes. A remarkable increase in photocurrent more than one order of magnitude was recorded with respect a commercial nickel electrode submitted to the same thermal annealing, mainly attributed to the enhancement of the surface area.

An improvement in photoactivity considering the real surface area of the electrode was also recorded.

These results demonstrate that the particular morphology and structure developed with the adopted strategy positively affect both the electroactivity and photoactivity of the samples.

Chapter 3

PANI/PSi hybrid materials

3.1. Background

In the last decade there have been many attempts to fabricate hybrid organic/inorganic structures to obtain materials with optimal electrical and optoelectronic properties for several kind of devices, such as light-emitting devices, solar cells, sensors and biosensors.[106] The main limitation present in these systems is the lack of strong interfacial bonding between the organic molecules and the surface of the material. The production of stable bonds between organic compounds and conductive surfaces represents a chance to overcome this limitation. The chemical or electrochemical grafting of organic molecules or polymers has been widely studied because it allows to obtain dense and ordered layers able to protect the surface or to give specific properties.[107] An affordable route to obtain covalent grafting on conductive surface is represented by the electrochemical reduction of diazonium salts: as proposed earlier in 1992 by Jean Pinson and co-workers.[108] This method has been adopted to promote covalent bonds between aryl groups with different substituents and several substrates such as gold, glassy carbon and silicon.[109,110]

There are four commercially available aryldiazonium salts such as 4-nitrobenzenediazonium tetrafluoroborate, 4-bromobenzenediazonium tetrafluoroborate (4-NBD), 4-formylbenzenediazonium hexafluorophosphate and 4-aminodiphenylamine diazoniumsulfate. The most employed diazonium salt has been 4-NBD because its NO_2 group can be electrochemically reduced into NH_2, providing a confirmation of the success of the grafting reaction and allowing quantifying the electroresponsive groups attached to the surface.

Several electrochemical parameters (scan rate, time of reduction) and operative mode (cyclic voltammetries, potentiostatic, galvanostatic) can be employed in order to control the surface coverage and the density of the resulting organic layer, yielding sub-monolayer to multilayer films. [111,112] Different media for this reaction have been also investigated: typically, the electrochemical reduction of diazonium salts is performed in acetonitrile (ACN) or acidic aqueous solution as protic solvents. Recently also different ionic liquids have been proposed for the electrochemical reduction of 4-NBD on graphene sheets[113] and glassy carbon electrodes.[114,115]

3.1.1. Electrochemical functionalization of PSi surfaces

Among the porous materials, porous silicon electrodes (*PSi*) have been investigated for many applications in several fields, spanning from gas- and bio-sensing to photonics and photovoltaics, mainly because of its open pore structure, high specific area, biocompatibility, electroluminescence and photoluminescence properties.[26-29] Moreover, *PSi* is well known for is large use in photolitography.

Photolithography is a common method that requires a strong resistance to etching solutions: it is difficult to perform it on *PSi* for several reasons which mainly come from the high reactivity of the porous layer and the unwanted pore filling.[116] *PSi* patterning is usually achieved by performing a lithographic process on silicon (*Si*) surface before the *PSi* electrochemical etching[117] or through holographic methods directly on the porous surface.[118,119]

It is well known that the optical lithography on *PSi* is hindered by the high reactivity of the material being easily etched by alkaline solutions.[120] On the other hand, in literature several methods for the stabilization of the *PSi* surface, e.g., thermal carbonization, hydrosilylation, electrochemical modification, or high-temperature thermal oxidation are reported. [116,121–127] Another method is the polymer impregnation of *PSi* that has been proposed a few years ago by L. De Stefano et al.[128] with interesting results in terms of layer stability. In that case, the impregnation was performed by drop casting and spin coating. Other approaches have been proposed in literature in order to create organic ordered layers. The first way proposed to promote

Si-C covalent bond by chemical or photochemical reactions: the hydrosilylation of alkenes at H-terminated Si surfaces and the silanization of hydroxyl-terminated Si surfaces are only some examples of the modification of silicon with organic compounds. An alternative way to obtain covalent grafting on Si surface is represented by the electrochemical reduction of diazonium salts: as proposed earlier in 1997[129], 4-nitro- and 4-bromobenzenediazonium salts can be electrochemically reduced on H-terminated Si (111) surfaces in an aqueous acidic HF solution.

In ***Fig. 39*** is shown the proposed reaction mechanism for the electrochemical reduction of diazonium salts on silicon electrode. [109] It is well known that the electrochemical grafting starts with the cleavage of dinitrogen and the formation of phenyl radicals, which abstract a hydrogen atom from the surface to produce a silyl radical. The silyl radical reacts with a second phenyl radical, allowing the formation of a Si-C bond.[109]

More recently, the reduction of different diazonium salts on *Si* has been demonstrated with no applied voltage due to the spontaneous electron transfer at the OCP, which leads to the local generation of aryl radicals.[130,131] The required contact time for the spontaneous grafting ranges from 30 to 60 min while the potential-driven electrochemical reduction allows faster reaction rates and the surface of silicon is protected against the formation of SiO_2. It is worth to note that H-terminated silicon is not strictly necessary for the electrochemical reduction of diazonium salt: nitrobenzene and 4-methoxydiphenylamine have been grafted on Si surfaces with electrochemically grown SiO_2 layers by K. Roodenko et al.,[132]

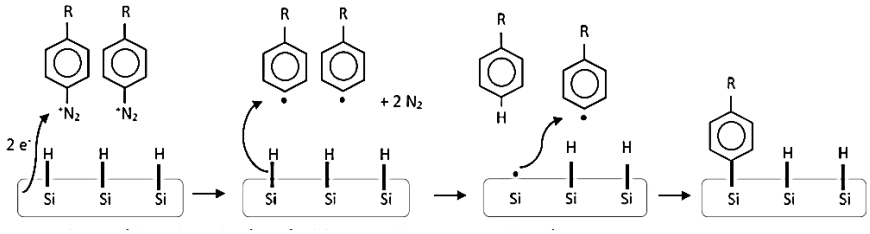

Fig. 39 *Mechanism of electrochemical grafting of aryl diazonium salts on silicon electrode.*[133]

In this scenario, in this PhD project the functionalization of *PSi* surface by electroreduction of 4-NBD was performed. In the following paragraphs, we will see that this approach allowed to obtain a stable and uniform coating

that provides strong resistance to the etching solutions. Moreover, we will see that this organic coating is also suitable for further functionalization treatments that in this study will lead to the development of a *PANI/PSi* hybrid material.

3.1.2. PANI as conducting polymer

Conducting polymers (CPs) have lately attracted attention and a significant effort has been put to understanding properties and conduction mechanisms. A wide range of CPs, with different compositions and structure have been investigated: polyacetylene (PA), polyaniline (*PANI*), polythiophene (PT) and polypyrrole (PPy).[134] CPs exhibit good conductivities, although lower than metals, keeping the mechanical properties of a polymer. Furthermore, CPs often show a switch behaviour: they can change their conductivity from *p*-type (electron-acceptor) to *n*-type (electron-donor) and vice versa. [135] In particular, *PANI* displays excellent properties: a wide range of conductivity forms (from insulating to metallic regime), unique redox tunability, good environmental stability, low cost and ease of synthesis, as well as electrical conductivity considerably higher than a standard polymer**.** [136]. Applications of *PANI* in solar cells, capacitors and supercapacitors, ion and gas sensors have been broadly studied.[110,137–139]*PANI* can be obtained by chemical or electrochemical oxidative polymerization of aniline;[140,141] moreover, recently photochemically initiated polymerization[142] and enzyme catalyzed polymerization were also reported in literature.[143]
The electrochemical growth and redox mechanisms of *PANI* have been extensively investigated. [144,145]
Electrochemical polymerization of aniline is typically performed in strong acidic aqueous media, such as nitric or chloridric acid, which stabilize the primary cation radical required for the polymerization initiation (***Fig.40***).[146] This process is demonstrated to be auto-catalyzed, [146] and the experimental factors: electrode material, solution composition, dopant anions, pH of the electrolyte etc., effect the polymerization process.[147–149]

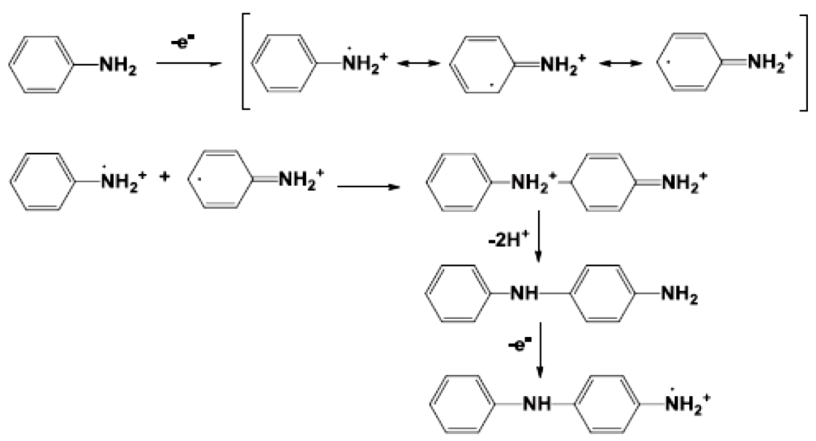

Fig. 40 *PANI in strong acid media.*[146]

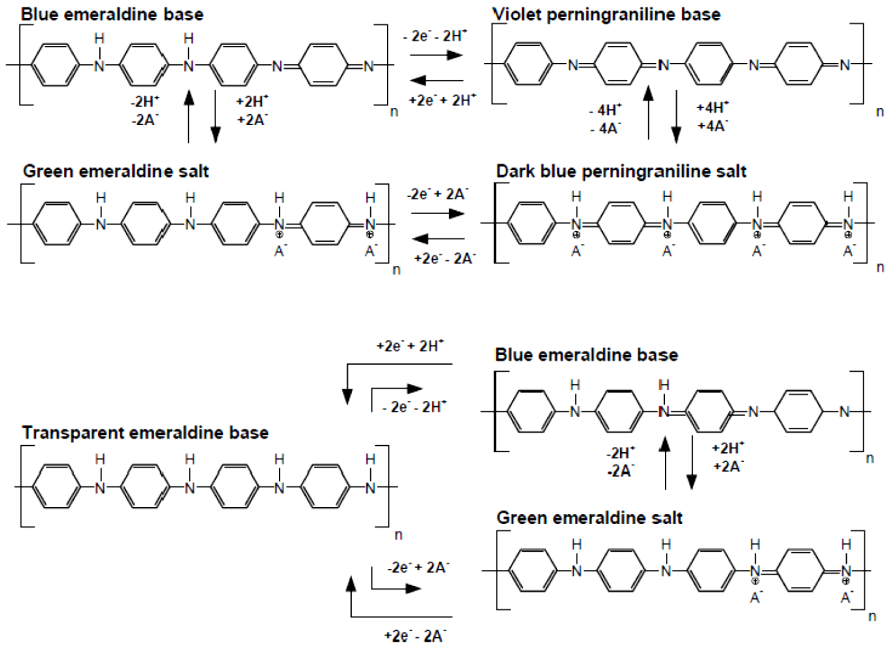

Fig. 41 *PANI forms and reversibility.*[150]

The process starts with the formation of dimeric species from nucleophilic attack of the aniline on the nitrene cation radical, resulting in three dimerization products, as well as competitive degradation reactions.[151]
Among the electrochemical techniques to synthesize *PANI*, different electrochemical methods such as cyclic voltammetry, [152,153] potentiostatic, [154,155] and galvanostatic [156,157] have been successfully employed.
Depending on its redox state, *PANI* can show different forms: leucoemeraldine (LE), emeraldine (E), nigraniline (NA) and pernigraniline (PNA)[150] (***Fig. 41)***. The only conducting form of *PANI* is emeraldine salt, obtained by doping or protonation of emeraldine base with the imine nitrogens protonated by acids.[158,159]

3.1.3. PSi/PANI hybrid structures

A flexible way method to produce hybrid nanocomposite materials with improved electrical and optoelectronic properties consists in to couple a porous matrix with a highly conductive organic conjugated polymer.[84,160]
Hybrid structures of *PANI* and *PSi* have been investigated from 1993 by V. P. Parkhutik [161]and studied as a rectifier exploiting the properties as p-n junction. Both n and p-type *PANI* and p an n type *PSi* were employed.[162,163]
Different methods of coupling have been used such as spin coating and direct chemical or electrochemical polymerization of aniline onto the surface of *PSi* or oxidized *PSi*. [164–166]
A *PSi/PANI* immunosensor has been electrochemically developed with the aim to obtain stable immobilization of biomolecules and a great sensitivity and specificity of the device.[164]
Two main limitations are often present in these systems: the high reactivity of hydrogen terminated silicon surface[165]and the very limited adhesion between *PANI* and substrates of different nature, due to the lack of strong interfacial bonding.[110] To overcome these limitations, Chiboub et al. proposed the chemical synthesis of aniline-terminated *PSi* surface by reacting brominated *PSi* layer with aniline molecules: the aniline moieties anchored onto the *PSi* surface were used as reactive sites for *PANI* polymerization.[165]

As reported above, the functionalization of the surfaces by electroreduction of aryl diazonium has been proposed as a suitable way to realize an underlayer, resulting in organic films generally insulating, optically transparent and highly adherent. [109,167,168] Depending on the applications, two main approaches can be adopted for the functionalization: the first involves the diazotization *in situ* of aryl amines with $NaNO_2$, followed by reductive grafting; the second the use of commercially available and stable diazonium salts, such as 4-NBD.[169] The latter approach allows avoiding the use of HCl and the problems arising from diffusion of $NaNO_2$ inside porous structures as *PSi*.

It was demonstrated that the presence of an underlayer is able to improve the deposition of many polymers at metals and semiconductors surfaces.[170–173]

The electrodeposition of *PANI* using an underlayer obtained by electroreduction of aryl diazonium has been firstly employed by Santos et al., [174] who demonstrated that a thin layer of diphenylamine grafted on glassy carbon surfaces allows to improve the stability of the hybrid structures. The underlayer was obtained through electrografting of nitrobenzene from a corresponding diazonium salt followed by electrochemical reduction of the nitro group to ammine. The electrochemical reduction of diazonium derivatives represents a flexible technique for surface functionalization.

Recently, Jlassi et al., performed the aniline polymerization in presence of the 4-diphenylamine[175,176] diazonium-modified bentonite, obtaining exfoliated clay/polyaniline nanocomposites conversely to those prepared with unmodified clay which exhibited a polyaniline-rich surface but without any sign of exfoliation. Moreover, they demonstrated that the presence of the organic layer significantly modifies the interface of the composite leading to an improvement in dielectric properties and mechanical properties. A similar approach has been adopted by A. Mekki et al.,[177] to synthesize multi-walled carbon nanotubes–polyaniline nanocomposites with enhanced conductive properties and high surface area.

In the second part of the following chapter of this thesis a layer-by-layer approach is proposed, in which a layer of phenyl ammine has been electrochemically deposited on the surface of *PSi* and used as underlayer for the subsequent step of aniline electropolymerization. This multistep

technique has been recently used to obtain stable and covalent bonds between: gold and poly(para-phenylene), [178] *PANI* and gold, [110] *PANI* and nanotubular TiO_2[84] and to the best of our knowledge has not been applied to hybrid *PSi/PANI*. The underlayer has been obtained through electrografting of 4-NBD from a corresponding diazonium salt followed by electrochemical reduction of the nitro group to ammine.

3.2. Experimental methods

3.2.1. Chemicals

Anhydrous acetonitrile (ACN, 99.8%), 4-nitrobenzenediazonium tetrafluoroborate (4-NBD salt), tetrabutylammonium hexfluorophosphate ($TBAPF_6$), aniline (>99.5%) and potassium nitrate (KNO_3) were purchased from SigmaAldrich®. Hydro-fluoric acid (HF, 50%) and perchloric acid ($HClO_4$, > 70%) were supplied by Carlo Erba. Pure ethanol was obtained from VWR.
Aniline was freshly distilled and stored in the dark. The aqueous solutions were prepared with double-distilled water (18 M Ω cm).

3.2.2. Electrochemical Set-up

All electrochemical experiments were performed at room temperature using an AUTOLAB PGSTAT302N (Metrohm, Switzerland) potentiostat/galvanostat equipped with a frequency response analyzer controlled with the NOVA software.

A conventional hand-made three-electrode cell (V = 5 ml) made by a cylindrical Teflon chamber (base diameter = 2.5 cm; height = 5 cm) containing the electrolytic solution was employed. *PSi* samples (Physics Department, University of Cagliari) were used as working electrodes and located at the bottom of the cell; the electrical contact consisted in an aluminum disc. The circular exposed geometrical area of the electrodes was 0.6 cm^2 (diameter = 0.87 cm). A platinum titanium grid placed in front of the anode at 1 cm distance constituted the counter electrode. A platinum tip was used as quasi-reference electrode.
All the potentials presented refer to Pt quasi-reference electrode.
The *PSi* electrochemical anodization was carried out in the dark in an etching solution composed by HF:H_2O:EtOH in a 15:15:70 proportion, respectively, using a current density of 50 mA/cm^2. [179] The geometry of the electrodes was circular with 1 cm of diameter.
Fig. 42 shows the complete electrochemical set-up.

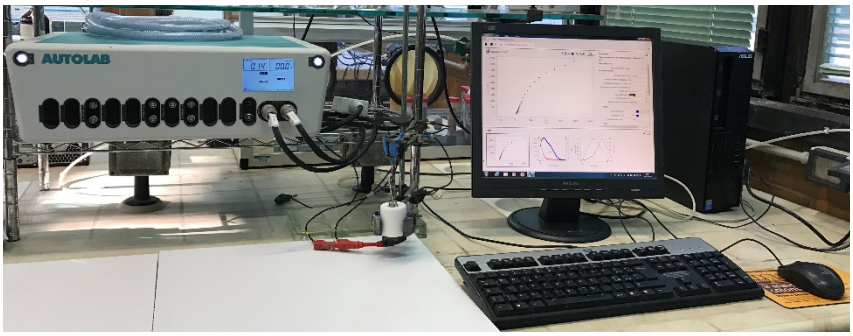

Fig. 42 Electrochemical set-up adopted to prepare *PSi*/*PANI* Hybrid structures

3.2.3. Electrochemical synthesis and characterization

Electrochemistry

The functionalization of *PSi* adopted for the resistance test against alkaline solutions was performed both by cyclic voltammetry (CVs) and by potentiostatic techniques. ACN + 0.1 M ($TBAPF_6$) solutions containing 2 mM of 4-NBD were employed. Consecutive CVs in the potential range −0.4/−1.2 V at a scan rate of 10 mV/s were performed with a number of cycles of 2, 5, 8 and 12 .The potentiostatic runs were performed by applying −1.1 V for a total time of 600 s.
The *PSi* submitted to the following two electrochemical steps to obtain a *PSi/PANI* heterojunction were functionalized using the CV approach.
A number of five cycles was used, followed by a potentiostatic step at -1.1 V for 300 s. Moreover, two CV have been performed in the same solution. In the second step, the nitro groups were electrochemically reduced to amino groups in a water/ethanol solution (90/10%) $_{V/V}$ containing KNO_3 0.1M, as supporting electrolyte. Two CV were carried out by varying the potential from the OCP to -1.7 V and back to -0.5 V, at a scan rate of 10 and 100 mV/s, depending on the experiment.

In conclusion, the polymerization of aniline was electrochemically performed by CV in ACN solution containing $HClO_4$ (0.1 M) and aniline (0.1 M). The potential was varied from the OCP to -0.8 V and back to -0.2 V. In order to obtain *PANI* in the emeraldine salt form, the last scan of the polymerization was ended at -0.2 V in the anodic direction.

For a better understanding samples obtained by electropolymerization on aminophenyl modified *PSi* are denoted along the text as *PSi/Ar/PANI*. Several *PSi/Ar/PANI* samples were prepared using different scan rate of polymerization from 30 mV/s to 100 mV/s. Some samples have been also prepared with different number of potential cycles (from 4 to 10 cycles), at fixed scan rate of 30 mV/s.

For comparison, the electrochemical polymerization of aniline was carried out directly at *PSi* sample, without the deposition of aminophenyl underlayer. These samples are called in the text as *PSi/PANI*.

To remove any physisorbed, unreacted materials from electrode surface, the electrodes were rinsed carefully with ACN between each preparation steps. Finally, the electrodes were dried with nitrogen stream.

Characterization

The modified substrates were characterized by electrochemical impedance spectroscopy (EIS) in ACN solution containing 0.1 M $TBAPF_6$ by varying the frequency from 30 kHz down to 0.1 Hz at OCP with excitation amplitude of 10 mV. The impedance spectra were then fitted to an equivalent electrical circuit by using the ZSimpWin 2.0 software (EChem software).

The electrodes have been characterized also through (CVs) before and after the electrochemical aniline polymerization, starting from OCP to -0.8 V and back to -0.2, in ACN solution containing 0.1 $HClO_4$. Different values of scan rate were used.

A scanning electron microscope (SEM) was used to characterize the morphology of the *PSi* and *PSi* after electrochemical functionalization.

Optical reflectivity

A PerkinElmer Lambda 950 UV/Vis/NIR Spectrophotometer equipped with a Universal Reflectance Accessory was adopted for the optical reflectivity measurements (***Fig. 43***).

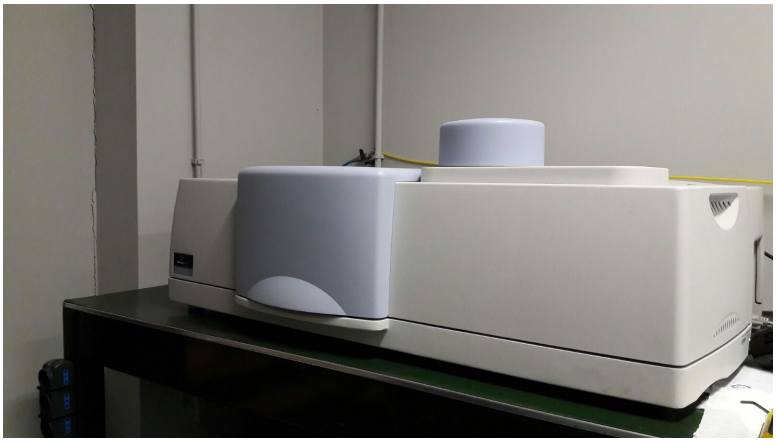

Fig. 43 *PerkinElmer Lambda 950 UV/Vis/NIR Spectrophotometer*

Optical reflectivity have been used to characterize the resistance of the 4-NBD grafted samples to alkaline etching solutions and to characterize the behavior of the samples after the electrochemical polymerization step.
The reflectivity spectra have been then measured in the 250–2500 nm wavelength range. For comparison, also the optical reflectivity of the pristine *PSi* layer was measured.

Photocurrent measurements

PSi and *PSi/PANI* hybrid structures were submitted to photocurrent measurements to evaluate the device efficiency. The photocurrent measurements were performed with samples covered with a sputtered semitransparent gold contact using a white light source (tungsten halogen lamp) focused on the samples surface by means of a microscope objective to a circular area with a diameter of 0.4 cm.

The photocurrent measurements were performed using a series of long-pass filters in the UV-VIS range (305–830 nm range). The photocurrent set-up is shown in ***Fig. 44***.

Photocurrent measurements were also performed in order to evaluate the reversibility between the protonated and deprotonated *PANI* form; the samples have been dipped first in a basic solution (ACN containing 0.1 M NH_3; pH=9) and then in an acid solution (ACN containing 0.1 M $HClO_4$; pH=4): after each dipping step, the photocurrent was recorded.

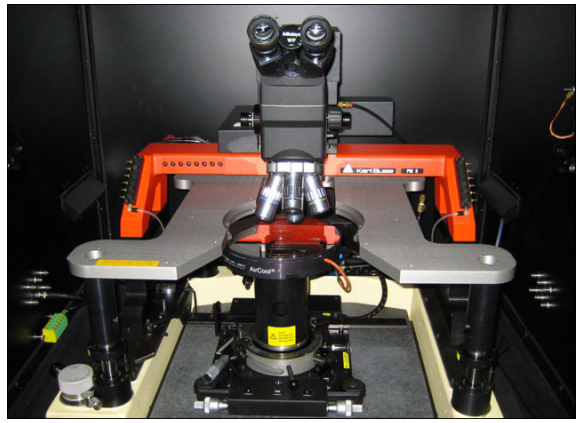

Fig. 44 *Photocurrent set-up.*

3.3. Results: 4-NBD Electrografting

The freshly *PSi* samples were submitted to the electrografting of 4-NBD in ACN media solution containing 2 mM 4-NBD and 0.1 M ($TBAPF_6$), as supporting electrolyte.
ACN media was used due its low surface tension of 26mN/m (25°C), in order to guarantee an easy penetration inside the porous structure. ***Fig. 45*** reports the first and the fifth cycle of electrografting process on a *PSi* electrode. The current density (J) was calculated with respect to the geometric surface of the sample (0.6 cm^2). As can be seen the first cycle of the cathodic scan displays an irreversible diazonium reduction peak at - 0.7 V, related to the reduction of aryl diazonium cations to aryl radicals. This indicates the cleavage of dinitrogen and the subsequent one electron covalent reaction between the silicon and nitrobenzene radicals and it is indicative of easy and fast reduction reaction on *PSi* surface.

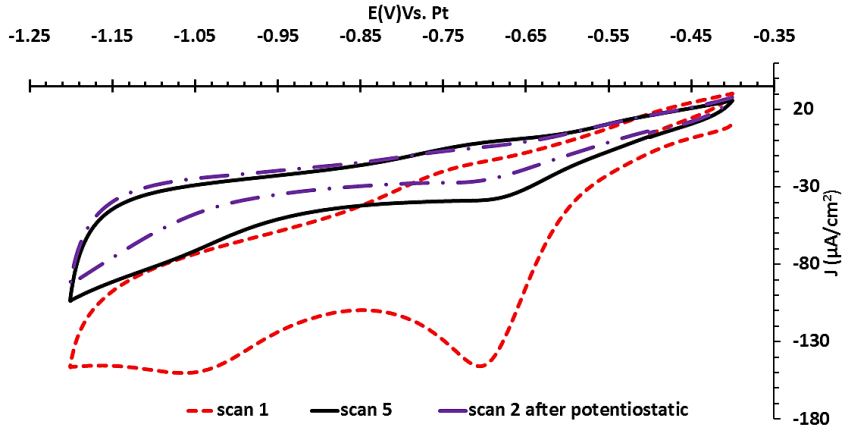

Fig. 45 *Cyclic voltammetries of PSi electrode in 2mM NBD + 0.1 M ($TBAPF_6$) at 10 mV/s.*[180]

As the number of cycles increases the reduction peak becomes less evident and a shift towards negative potentials can be appreciated, as well as a decrease of the recorded current, which it is indicative of the progressive

covering of the *PSi* surface. Indeed, as previously reported in literature, the grafting of monocristalline H terminated silicon involves a well-defined reduction peak in the first voltammetric cycle, that represents a fast and easy reduction of aryl diazonium cations to aryl radicals which can graft on the sample surface. [127,179,181] In the second scan, generally, the peak disappears nearly completely and this is indicative of the blocking effect of a dense monolayer, which hinders the further reduction at the surface. Instead, in our case, given the large inner surface of *PSi*, the diazonium reduction peak is still visible after five cycles indicating that the density of grafted molecules is not high enough in the first cycle. In fact, because of the very large surface that the porous structure of the silicon offers further electron transfer is possible during subsequent cycles. The negative shift of the reduction peak can be attributed to exchange of electrons between the silicon and diazonium molecules that are reduced on the already grafted molecules allowing the formation of a multilayer structure.

Fig. 46 shows the time evolution of the potentiostatic current during the functionalization under potentiostatic conditions at -1.1V for 600s.

As can be seen, the current density decreases by about one order of magnitude after about 2 minutes, indicating a complete passivation of the surface.

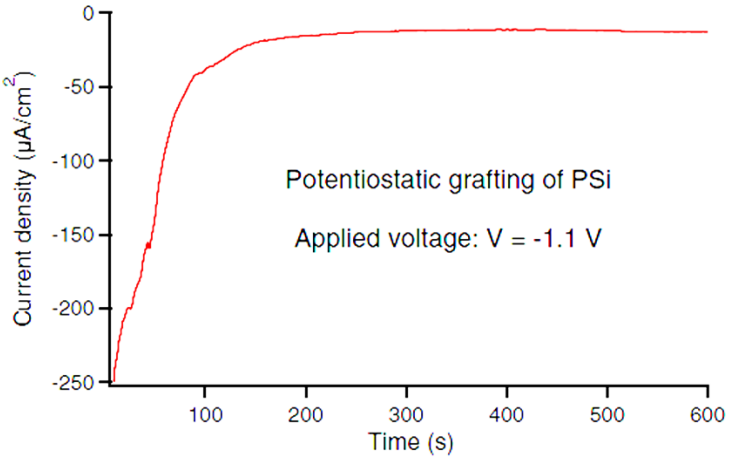

Fig. 46 *Current density vs time response during the grafting process performed at V=-1V.* [133]

To demonstrate the fully functionalization of the *PSi* surface two further CV scans were carried out. ***Fig. 45*** (violet line) shows the second voltammetric scan after the potentiostatic reduction where it is possible to appreciate the attenuation of the reduction peak, indicating a high degree of coverage of accessible *PSi* surface with nitrophenyl layer.
The amount of NBD reduced can be roughly estimated from the voltammetric charge related to the relevant peak using the Faraday's law:

$$\Gamma = \frac{Q}{nFA} \quad \textbf{(24)}$$

Where n is the number of electrons per molecule for reduction, that in this case is 1, F the Faraday constant, A the effective electrode area (338 cm^2) and Q is the charge associated to the cathodic peak.
Γ value of 4 $x10^{-11}$ mol cm^{-2} has been obtained in acetonitrile solution. Comparing these values with the theoretical value of $1.2x10^{-9}$mol cm^2 calculated for a close-packing layer of nitrobenezene. [109]
It can be observed that in ACN the molar concentration of nitro-phenyl groups is equivalent to a sub-monolayer.
However, these values are not a measure of the effective amount of 4-NBD deposited on the surface, because not all the aryl radicals graft to the electrode surface, due to the occurrence of reactions with other aryl groups in the solution to give dimers and polymers.
In order to obtain further information about the nitrophenyl layer, whose thickness can be estimated as 1–2 nm from the reduction of the average pore opening diameter in the case of 12 CV cycles samples, EIS measurements have been performed at OCP in a 4-NBD-free solution.
Fig. 47 shows the Nyquist and Bode plots for *PSi* modified using five voltammetric cycles (***Fig. 47b, Fig. 47d, Fig. 47f)*** and potentiostatic mode (***Fig. 47a, Fig. 47c, Fig. 47e***). Observing the plots can be appreciated that, in both the cases the deposition of the organic layer produces a significant increase of the impedance (blue curves) with respect to unmodified pristine *PSi* (purple curves). As shown in the Bode phase plots, the modification of the silicon surface permits the growth of the phase angle at high frequencies for both the electrografting methods, being higher for the sample grafted using five CV cycles.

The second phase maximum that appears after the grafting process in pristine *PSi* results shifted towards lower frequencies: moreover, the sample modified by CV shows a new overlapped wave, indicating the presence of a new time constant.

To obtain the characteristic parameters of the electrodes, the quantitative data analysis of the unmodified *PSi* has been performed using the equivalent circuit (EEC) typically proposed for porous silicon electrodes (See inset in ***Fig. 47e***). The elements, which composed the equivalent circuit are the solution resistance (R_S) and two parallel combinations. The first parallel combination is composed by the charge transfer resistance (R_{CT}) and a constant phase element (*CPE*). The last element has been employed instead of double layer capacitance C_{dl} for taking into account the surface roughness effects and inhomogeneity of the surface. The *CPE* exponent, *n*, is usually related to the surface defectiveness of the electrodes and it can be assume values in a range from 0 to 1.[182] The second parallel combination (R_p and C_p) has been inserted for taking into account the resistance and capacitance of the porous layer. The impedance spectra obtained for *PSi* modified by potentiostatic mode have been modelled with the same equivalent circuit, but using a CPE for the porous layer. Instead, for the sample modified with five CV cycles, a third p*arallel combination has further been added (See inset in* ***Fig. 47 f)***. R_L *and* C_L elements can be associated to the presence of an organic layer with high degree of coverage of the overall surface.

A good fit of the impedance spectra ($\chi^2 < 8 \times 10^{-4}$) has been obtained with these equivalent circuits.

The values of the circuit elements obtained from the fitting of the experimental data with the model are reported in ***Table 13***. As can be seen the R_{CT} enhanced after the 4-NBD grafting process, while the capacitance of the *CPE* element decreases. This was attributed to an increase of the thickness of the electronic double layer.

Both the effects can be associated to the presence of the phenyl layer on the surface. The exponent of the constant phase element related to the pores (n_p) is connected to the presence of inhomogeneity or variation in the composition of the surface inside the pore.

It approaches to 1 for the sample modified by potentiostatic mode: this can be related to a poor modification inside the pore structure. Values of $n_p << 1$

(see ***Table 13***) have been obtained for the sample modified with five CV cycles.

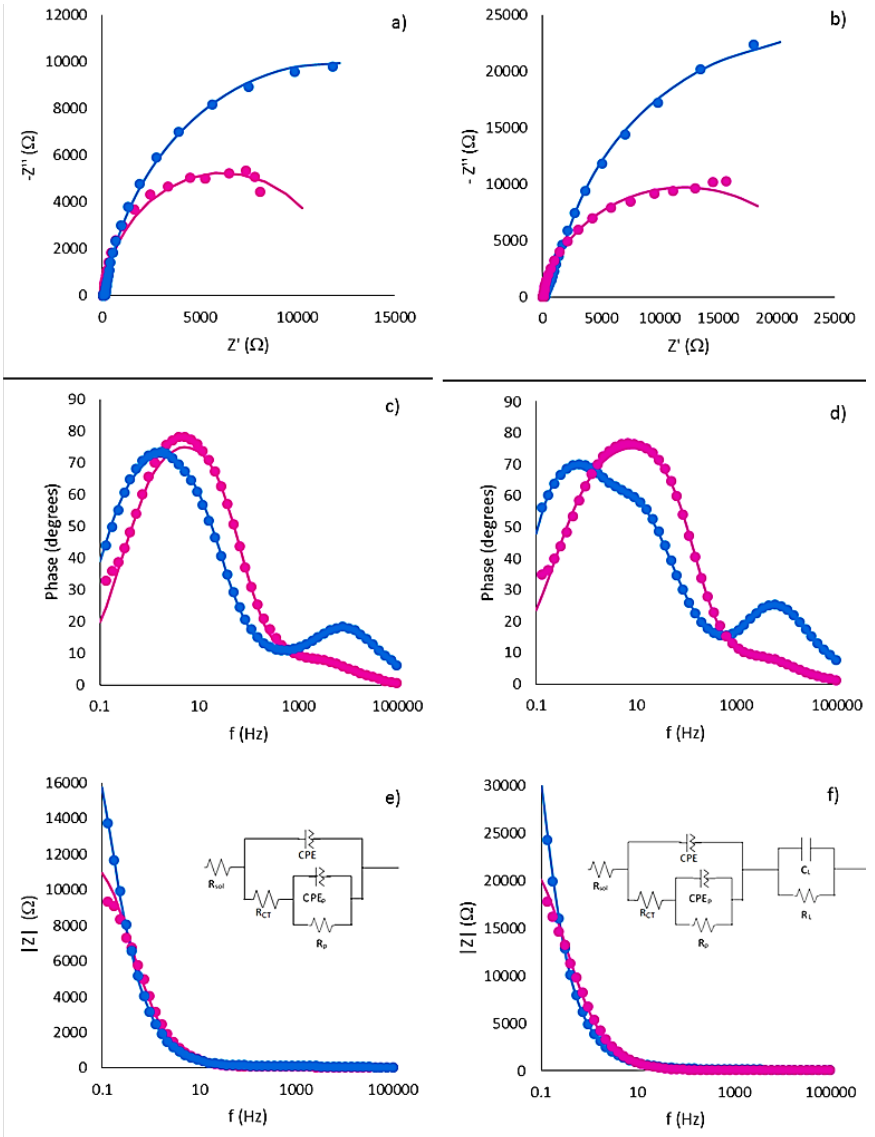

Fig. 47 *Nyquist and Bode plots compared for pristine PSi (purple) vs grafted PSi (blue) in the case of modification using potentiostatic method (a, c, e) and in the case of CV (b, d, f).In the insert the EEC adopted is reported.* [133]

A proof of a higher degree of coverage of the inner and external surface of the porous structure is given by the *RC* parallel combination. This component was added in order to model the sample modified with five CV cycles.

		R_{sol} (Ω)	C_{dl} (μF)	n	R_{CT} (Ω)	C_p (μF)	R_p (KΩ)	n_p	R_L (KΩ)	C_L (μF)
Sample 1	***Pristine PSi***	55.38	3.38	0.78	30.18	24	12.4	-		
	PSi pot.	56.9	0.45	0.72	103.3	57	23.6	0.91		
Sample 2	***Pristine PSi***	55.62	1.90	0.76	29.6	11.2	27.4	-		
	Psi 5 CV	61.13	0.34	0.81	146.8	45.9	1.88	0.77	45.8	42.5

Table 13 *Computed values obtained by simulation of impedance data by equivalent circuit analyses for PSi samples, before and after modification, both with potentiostatic mode (sample 1) and five CV (sample 2).*[133]

Optical reflectivity measurements

Optical reflectivity is a very sensitive technique for the porous layer modifications that allows to discriminate the pore diameters in a range of 10–20 nm. The porous layer is seen by the light as a homogeneous layer in the interval of the employed wavelengths. Any modification of the *PSi* layer, leads to a modification of its overall refractive index and then of the thin-layer interference fringes.

Observing the changing of amplitude and position in the thin-layer interference fringes together with the Si reflectivity peaks it is possible to evaluate the modifications of the layer with respect to freshly grafted *PSi* layer.

In order to investigate the chemical resistance of the 4-NBD grafted *PSi* samples have been dipped in NaOH aqueous solutions with two different concentrations: 0.5 and 0.1 M. The sample dipping duration was 10 s for the first two steps and 2.5 to 5 min for the other steps, depending on the samples chemical resistance. To characterize the improved resistance of

the 4-NBD grafted samples to alkaline etching, the optical reflectivity has been monitored after each dipping step.
In ***Fig. 48*** the effect on a pristine *PSi* layer after 10 s of dipping in a 0.5 M NaOH aqueous solution is shown. The red curve represents the pristine porous silicon reflectivity where it is possible to appreciate the typical *Fabry-Pérot* fringes, deriving from the light reflection at both the top and the bottom of the *PSi* layer and then associated to the thin-layer interferences; these are clearly visible for wavelengths longer than about 400 nm. After 10 s dipping (blue curve) the interference fringes are no more visible, due to the almost complete dissolution of the porous layer.
This it was expected since it is well known in literature that the dissolution of pristine *PSi* after immersion in a NaOH solution takes place very quickly. [120,183] The choice to use very concentrated basic solutions to test the resistivity of the grafted sample is linked to this reason.
As can be seen observing the ***Fig. 48*** the behaviour of the grafted *PSi* samples is markedly different with respect pristine *PSi*.

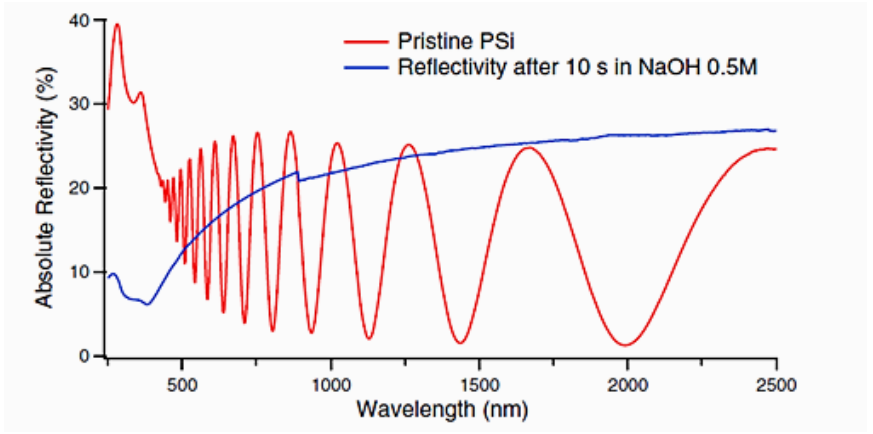

Fig. 48 *Absolute reflectivity spectra of PSi (in red) and PSi after 10 s of dipping in aqueous solutions containing 0.5 M NaOH.* [133]

Moreover, during the initial dipping it was possible to observe by naked eye that the portion of the *PSi* layer outside the nitrobenzene-grafted area (that it is the external surface region near the bulk Si-porosified Si separation border) was immediately dissolved, while the grafted area appeared unmodified throughout the process.

Fig. 49 shows the evolution of the reflectivity as a function of the total dipping time (20 s) for a *PSi* sample whose grafting has been realized using the potentiostatic method (V=-1V; t= of 600 s) . For comparison the pristine and freshly grafted samples are also shown (red and black curves, respectively).

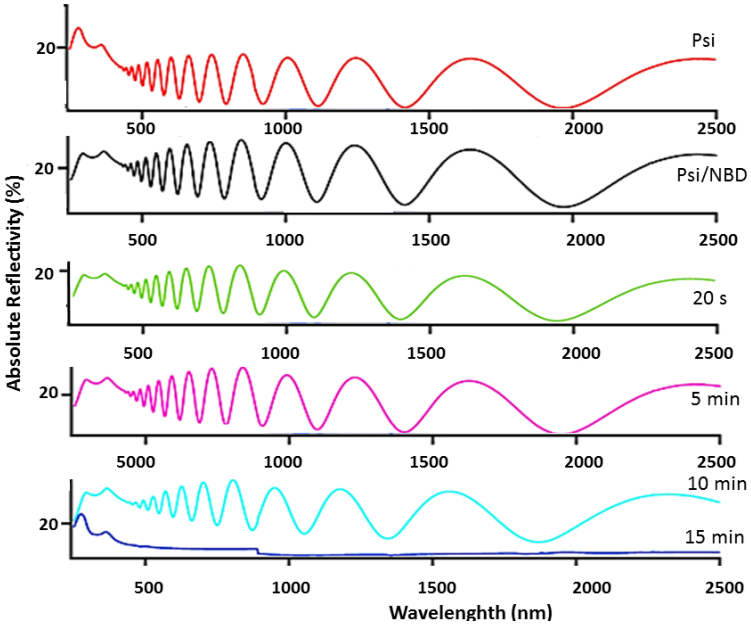

Fig. 49 *Reflectivity spectra of PSi sample (in red), of PSi after NBD grafting by potentiostatic runs (in black) and of the NBD grafted sample after 20s (in green), 5 min (in purple) and 15 min (in light blue).*[133]

The decreased reflectivity of the Si-related double peak and the interference fringes displacement demonstrate both the Si covering and the modification of the average refractive index of the porous layer induced by the nitrobenzene grafting.

It is evident that after about 5 min of dipping in NaOH solutions the spectrum shape remains unmodified, indicating a corrosion resistance in such environment. Instead, it is possible to appreciate that the portion of *PSi* layer not covered by 4-NBD diazonium salt was immediately dissolved in the alkaline media, while the covered portion stayed stable for much time.

After 10 min of dipping, the reflectivity started to change and after 15 min of dipping, no trace of the porous layer is observed, indicating a full *PSi* dissolution. The grafting method performed by potentiostatic runs has significantly improved the chemical resistance of the *PSi* layer, which does not vary for two order of magnitude longer times with respect the pristine *PSi*.

The behaviour of the samples grafted using CV techniques was also studied in order to evaluate if the electrochemical method could affect the chemical resistance of the organic layers. Since the *PSi* coverage depends essentially on the number of CV, the chemical resistance of the samples grafted using different numbers of cycles was investigated.

In ***Fig. 50*** the evolution of the reflectivity spectra of a *PSi* grafted with five CV cycles as a function of the dipping time is shown.

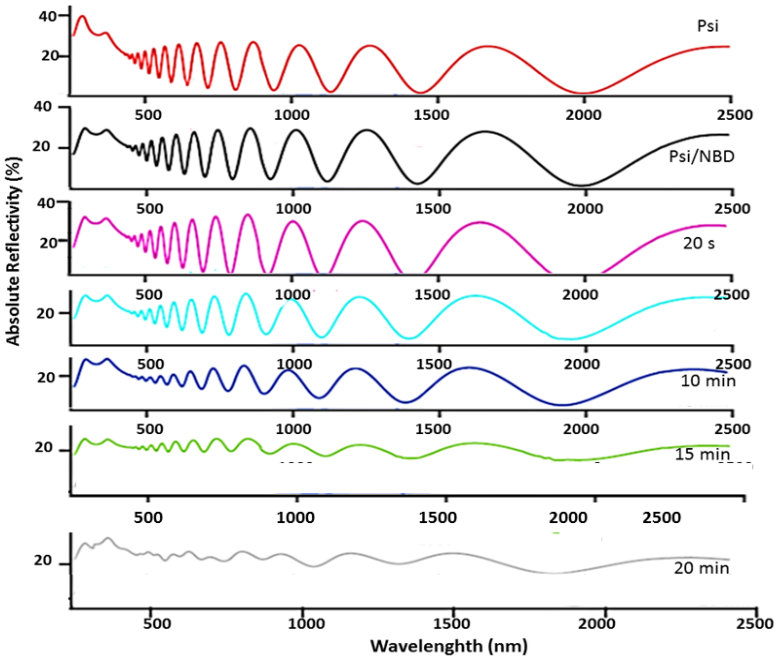

Fig. 50 *Reflectivity spectra of PSi (in red), PSi NBD grafted sample with 5 CV (in black) and of the NBD grafted sample after 20s (in pink), 5 min (in light blue), 10 min (in blue), 15 min (in green) and 20 min (in grey) of dipping in NaOH 0.5M.*[133]

It can be observed a significant increase by a factor of two to four with respect the functionalization in potentiostatic regime: after 20 min of dipping in NaOH solution the thin film interference fringes are still visible, although appear partially degraded, indicating that the porous layer was still present.

Since, as shown in ***Fig. 45***, after five CV cycles the reduction peak was still present, the chemical resistance test were performed on samples using a different numbers of CV cycles during the electrografting process. For less than five CV cycles, the chemical resistance resulted still higher than that observed for potentiostatic grafted samples but it decreased with respect to that obtained for the grafted samples with five CV ***(Fig. 50).*** For more than five CV cycles, instead, an increase of the chemical resistance was recorded.

As in ***Fig. 50***, in ***Fig. 51*** the evolution of the reflectivity spectra for a *PSi* sample grafted with eight CV cycles is shown.

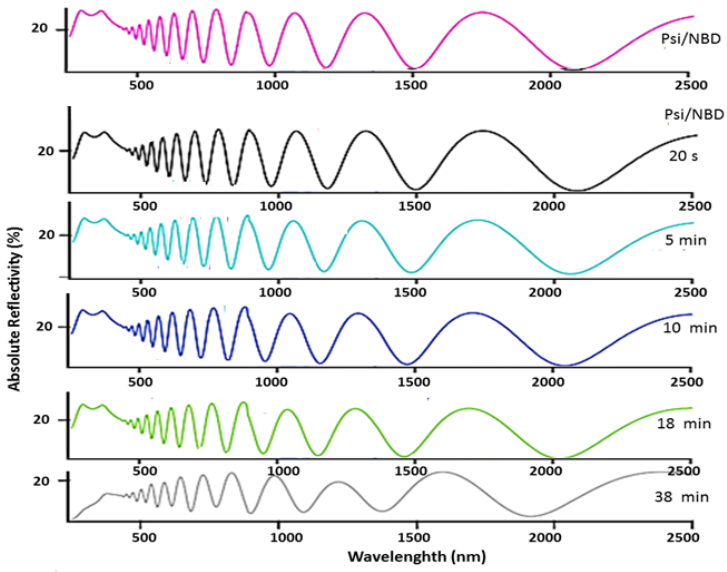

Fig. 51 *Reflectivity spectra of PSi after NBD grafting with 8 CV (in purple) and of the NBD grafted sample after 20s (in black), 5 min (in light blue), 10 min (in blue, 18 min (in green) and 38 min (in grey)of dipping in NaOH 0.5M.* [133]

In this case, it is evident that there is a significant improvement with respect to the grafting with five CV: after 38 min, the *PSi* structure is only poorly modified. Further increasing the number of cycles not significantly improved the chemical resistance of the samples, although the reduction peak was visible up to the 12th cycle.

Morphologic characterization

In collaboration with the University of Turin a morphological characterization of *PSi* after 4-NBD functionalization has been performed through scanning electron microscopy (SEM).
Fig. 52 shows the cross-section of the 4-NBD grafted sample with 12 CV. As can be noticed the pore openings are still remarkably visible and there is no sign of pore clogging (***Fig. 51b).*** It is important to remember that the sample functionalized using 12 CV cycles is fully functionalized since the diazonium reduction peak almost disappeared at the last CV. This is an important feature, since after the electrochemical grafting there is still space for further functionalization and/or pore filling with other materials.

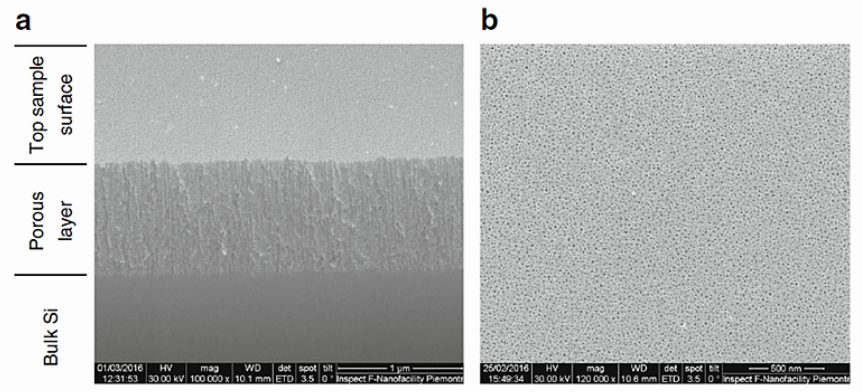

Fig. 52 *SEM images of cross section (a) and plane view (b) of PSi sample 4-NBD-grafted with 12 CV cycles. The different parts of the sample are indicated (a).* [133]

3.4. Results: Electrochemical reduction of NO_2 to NH_2

After the 4-NBD electrografting, the modified electrodes were removed from the solution and carefully rinsed with acetonitrile to remove the weakly adsorbed molecule.

In a preliminary study, different potential windows and scan rate have been used in order to perform the reduction of the nitro groups to amino groups. The reduction was carried out in H_2O/EtOH media, in presence of KNO_3 as supporting electrolyte. As well as ACN, ethanol was used in order to ensure an easy penetration of the solution inside the pores, since it presents a surface tension of 21.5 mN/m (25°C), comparable to that of ACN.

The use of a potential window for the reduction up to a cathodic limit of -1.8 V has led the evolution of hydrogen bubbles; then for the following experiments a cathodic limit of -1.6 V has been chosen.

The electrochemical reduction of nitro to amino groups has been often realized using water/ethanol in presence of a supporting electrolyte (i.e. KCl or KNO_3): very well defined peaks have been reported in the literature and also in our previous works on flat surfaces.[184]

Fig. 53 shows the cyclic voltammetries related to the nitro group reduction to ammine group in H_2O/EtOH media in presence of KNO_3 as supporting electrolyte, at 10 mV/s.

It is possible to observe the presence of well-defined peaks both in the cathodic and anodic direction in the first potential scan.

The common employed mechanism for the reduction of nitrophenyl moieties in protic medium implicates the formation of the redox reversible couple nitrous/hydroxylamine (NO/NHOH), followed by the irreversible amination of the hydroxylamine group. [185,186]

According to this mechanism, the peak in the first cathodic scan can be related both to the formation of hydroxylamine intermediate and its irreversible reduction to NH_2 groups, while the anodic peak designates the formation of the nitrous group from the hydroxylamine intermediate.

The size of the reduction peak in the second cycle significantly decreases, while the anodic peak is still visible. This is attributed to not totally conversion of the nitro to amino ones.

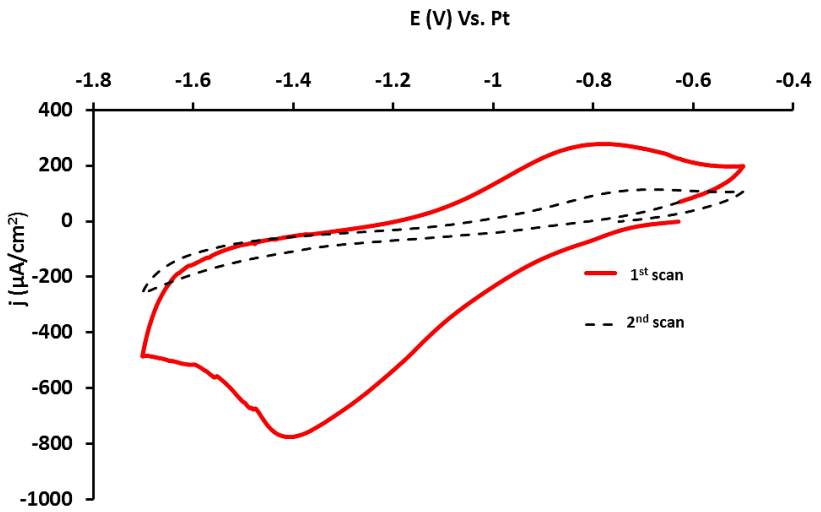

Fig. 53 *Cyclic voltammogramms of PSi sample modified with NBD in water/ethanol media containing 0.1M KNO_3, scan rate: 10 mV/s.* [180]

The reduction of nitro-groups requires 4 electrons for the formation of NHOH and 6 for NH_2, as follows (derivate by Faraday's law):

$$\Gamma_{NO_2} = \frac{Q(NO_2 \rightarrow NH_2)}{6FA} + \frac{Q(NO_2 \rightarrow NHOH)}{4FA} \qquad \textbf{(25)}$$

Where Q is the charge measured by integration of the two electrochemical signals, (reduction wave at -1.4 V and oxidation wave at -0.8 V), F is the Faraday constant, and A represents the real area of the electrode.
According **(24)** the surface coverage of an attached nitrophenyl groups Γ_{NO_2} can be evaluated by integration of the cyclic voltammogram in ***Fig. 53***. Values of 3.37 x10^{-11} mol cm^{-2} were obtained.
These values correspond at about 90% than those estimated for the NBD grafting (4 x10^{-11} [mol cm^{-2}]) and this means that just the 10% of the electro active groups is estimated to not be transformed in amino groups, (regarding the voltammetric charges involved in the reduction and oxidation processes). This indicates also that the 90% of the nitro-groups are accessible to the electrons.

Fig. 54 shows the cyclic voltammetries related to the second electrochemical step of nitro group reduction to ammine, performed at 100 mV/s.

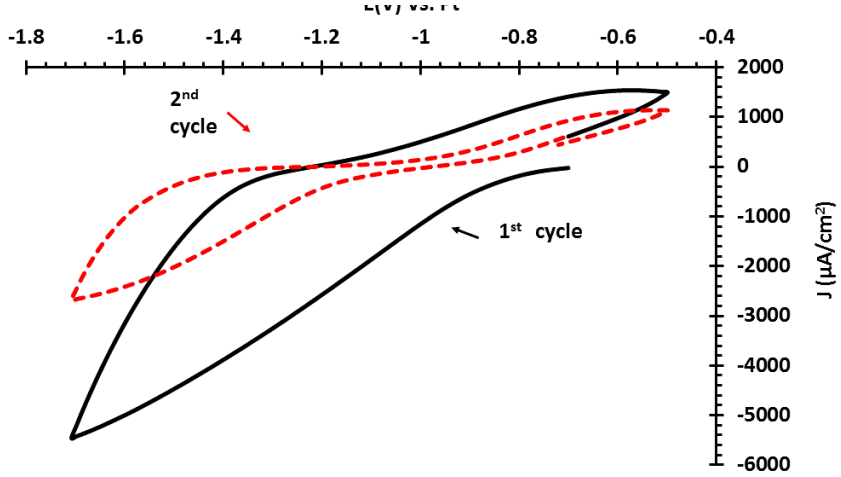

Fig. 54 *Cyclic voltammogramms of PSi sample modified with NBD in water/ethanol media containing 0.1M* KNO_3 *at scan rate of 100 mV/s.* [180]

As can be seen, conversely to the CV carried out at 10 mV/s a wide reduction wave is present in the first potential scan, while in the reverse scan an anodic shoulder can be appreciated between -0.7 and -0.6 V. The presence of the anodic and cathodic waves with respect to the peaks can be explained regarding the very high porosity of the system: the resulting very large area makes difficult obtaining defined peaks during voltammetric runs at these values of scan rate.

3.5. Results: aniline electropolymerization

After the second electrochemical step the samples were rinses in ACN and then submitted to the third electrochemical step. The electropolymerization has been performed in ACN solution containing $HClO_4$ (0.1 M) and aniline (0.1 M) at several values of scan rate. As a comparison, also pristine *PSi* samples were modified by direct electrochemical polymerization.
Fig. 55 shows the first and fifth scan of polymerization, performed at 30 mV/s onto a pristine *PSi* electrode (***Fig. 55a***) and a modified 4-NBD *PSi* electrode (***Fig. 55b)***.

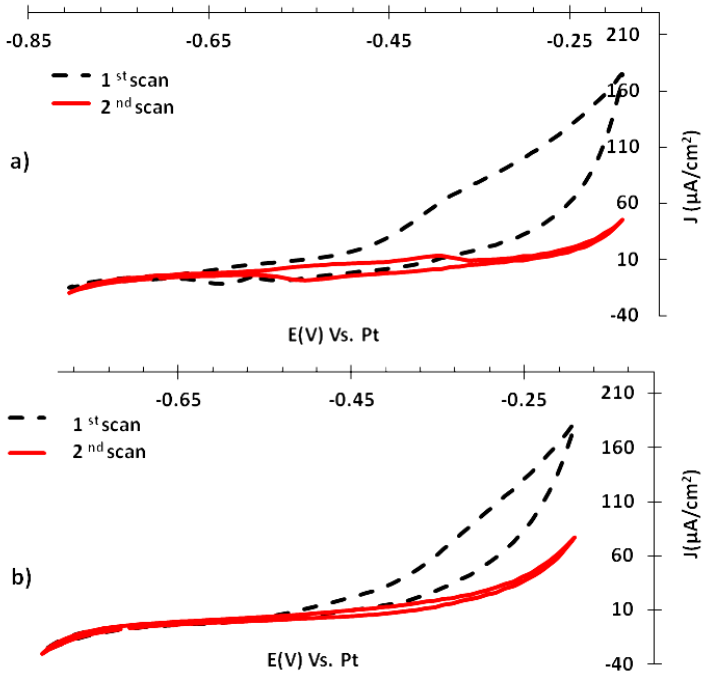

Fig. 55 *Cyclic voltammetry response recorded during electropolymerization of aniline in 0.1M $HClO_4$ +0.1M aniline in acetonitrile media on PSi (a) and PSi electrode after NBD reduction (b) at the scan rate of 30 mV/s.* [180]

As can be appreciated the first scan is characterized by an enhancement of the anodic current for both samples, linked to the oxidation of the aniline monomer to anilinium radical cation, which begins the electropolymerization process. This indicates, as reported in previous works that the aminophenyl layer has not blocking effect on aniline oxidation. [187,188] In the following scans, a couple of redox peaks is well visible only for *PSi* modified with aminophenyl layer (See magnification in ***Fig. 56***; black curve). In order to check if these peaks could still be the NO/NHOH reversible couple of the reduced NBD layer cyclic voltammetries were carried out in monomer-free solution before the electropolymerization, as control (***Fig. 56***; red curve).

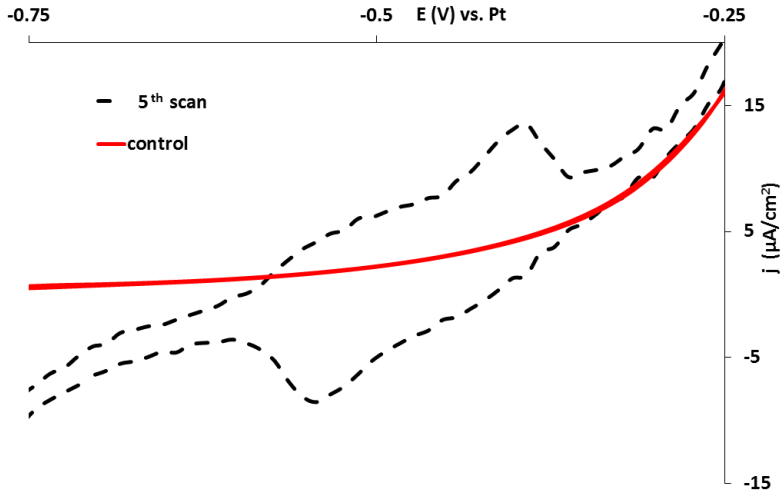

Fig. 56 *Cyclic voltammetry response (5th cycle) recorded during aniline electropolymerization and before electropolymerization in a monomer free solution on PSi electrode at 30 mV/s.* [180]

As can be noticed, not peaks can be appreciated in the polymerization range. In order to evaluate if the peaks attributable to NO/NHOH reversible couple could be detected both the $HClO_4$ concentration and the scan rate were increased up 0.4 M and 100 mV/s, respectively. Also in this case no peaks referable to characteristic *PANI* redox transitions appeared.
Then, it is possible to confirm that the two peaks detected during the electropolymerization can be ascribed to the redox transitions of *PANI* from leucoemeraldine to emeraldine and from emeraldine to pernigraniline. [189]

In case of direct electropolymerization at *PSi* samples, the redox couples were not visible neither in the fifth cycle, indicating that the polymerization process is more effective on aminophenyl-modified electrode: similar behaviour has been reported for gold and carbon based electrodes modified with *PANI* with and without aminophenyl layer.[110,190] In this case, the presence of aminophenyl layer grafted onto the *PSi*, can easily promote the oxidative radicalic polymerization process, due to the similarity of the organic layer to aniline. Then, the presence of the organic layer can offer a large number of starting points for the aniline polymerization, allowing to obtain a more strongly adherent coating than that without the organic layer.[146] Furthermore, this behaviour can be explained considering that the polymerization of *PANI* is a self-catalyzing and head-to- tail process: the nitrogen atom directly takes part in the redox transitions of *PANI* forms and its rate of precipitation enhances with amount of the reaction product.
The lower efficiency of polymerization observed with pristine *PSi* could be due to concentration gradients between the porous layer and the bulk of the solution during the electrochemical process. The concentration of aniline inside the pores (i.e. the concentration of reactant) decreased because of the formation of the anilinium radical cation. The monomer must then diffuse from the bulk to the porous layer, adding a mass-transfer resistance to the process. When the underlayer is present, the anilinium radicals may instead react with grafted phenylammine, which does not present diffusion limitations.
To demonstrate the presence of electroactive *PAN*I layer on the *PSi/PANI* samples cyclic voltammetries in monomer-free solution, containing $HClO_4$ 0.1 M, have been performed also after the electrochemical polymerization process, using several scan rate. In ***Fig. 55 57*** can be appreciated the typical peaks related to doping and dedoping of protons and anions in the polymeric layer , as well as the transition between the *PANI* different forms, which are well visible at high values of scan rate.[188]

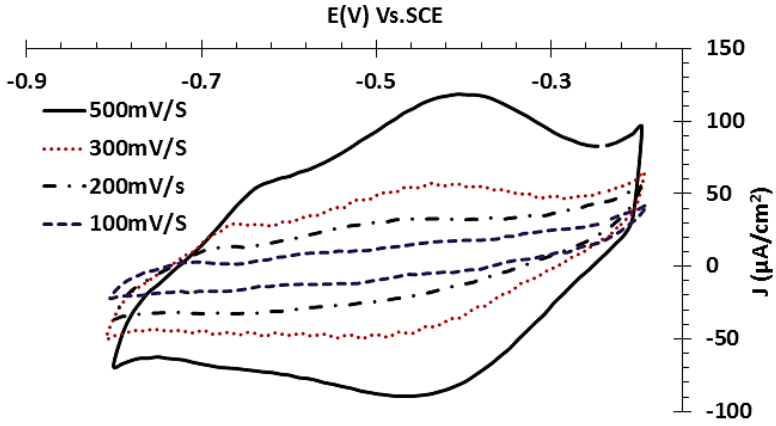

Fig. 57 *Cyclic voltammetries performed in ACN monomer-free solutions containing $HClO_4$ 0.1 M at PSi/Ar/PANI at different scan rates.* [180]

Optical reflectivity measurements

In order to evaluate the optical differences between the NBD modified samples and the pristine *PSi*, optical reflectivity measurements have been performed in the UV/VIS range. The optical reflectivity spectra of *PSi* samples has been collected before and after electrochemical modification.
Fig. 58 shows the comparison between pristine *PSi* and *PSi* sample submitted to direct aniline electropolymerization.
The reflectivity spectra of pristine *PS*i shows the two characteristic peaks of silicon at around 280 e and 360 nm and the typical series of regular thin-film interference fringes related to the presence of the thin porous layer on the bulk *Si* (for wavelengths higher than 400 nm). Instead, for wavelength longer than about 700 nm, where the *PSi* layer absorption coefficient is low, appear the classical interference figures due to the flatness of the external surface and of the *PSi/Si* interface. In the region between 450 and 700 nm the contrast of the interference fringes is progressively reduced when going from longer to shorter wavelengths due to the increasing absorption coefficient of the porous layer. At the shortest wavelengths the light beam entering in *PSi* is entirely absorbed.

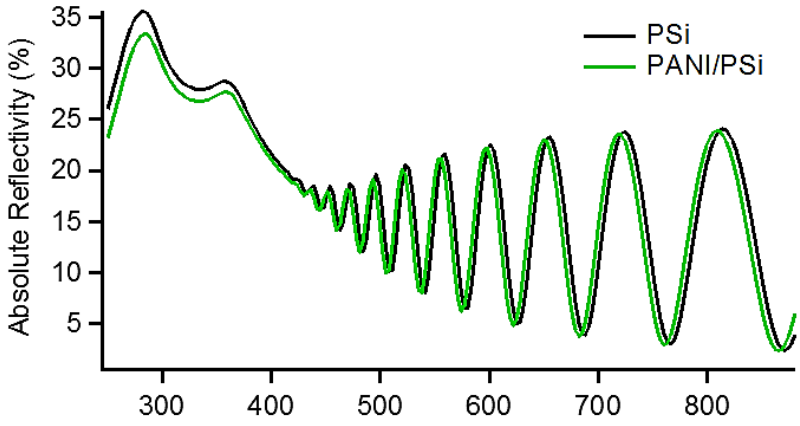

Fig. 58 *Reflectivity spectra of PSi (in black) and PSi submitted to aniline direct electropolymerization (in green).* [180]

The number and the position of the fringes depend on the optical thickness of the porous layer, that is the product of the refractive index times the real thickness, according:

$$m\lambda_{max} = 2n_{layer}L \qquad (26)$$

where, λ_{max} is the wavelength where is centred the fringe with the highest intensity, m is a integer number that corresponds to the spectral order of the fringe, n_{layer} the overall refractive index of *PSi*, L is the real thickness of the porous layer; $2n_{layer}L$ represents the length of the optical path.[191]
The refractive index of *PSi* depends on the porosity and, once that fixed, on the material that fills the pores. [191] When filling the pores, the air is progressively replaced by the polymer, changing then the overall refractive index of the porous matrix. It is important to underline that since the pores size is more than one order of magnitude smaller that the shortest wavelength in this spectrum, all light scattering effects can be neglected.
In ***Fig. 59*** can be appreciated the reflectivity spectra of *PANI/Ar/PSi* in comparison with pristine *PSi*. The comparison of spectra in ***Fig. 58*** and ***Fig. 59*** is interesting in view of understanding the different behaviours

induced in the *PANI* and *PSi* composite with and without the presence of the aryl underlayer.

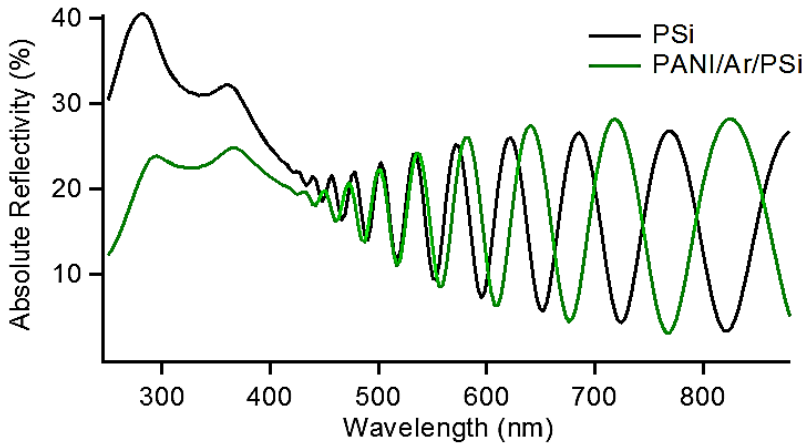

Fig. 59 *Reflectivity spectra of PSi and PANI/PSi (a); PSi and PANI/Ar/Psi.*[180]

It is evident that the *PANI/PSi* hetero-structure (green curve, ***Fig. 58***) does not show great optical differences with respect the pristine *PSi* (black curve). Instead, when the *PSi* is modified with the aryl layer before aniline electropolymerization, it is possible to observe a reflectivity spectrum (green curve) characterized by thin layer interference fringes, significantly modified with respect to the pristine *PSi* layer (black curve, ***Fig. 59***). Moreover, it can be appreciated that the presence of *PANI* also causes a considerable reduction of the *Si* double peak, since the silicon surface is progressively covered by the polymer. The displacement of the interference fringes is caused by the modification of the optical thickness of the layer.
The change of the periodicity of the fringes can be attributed to the presence of *PANI* within the pores, demonstrating the effectiveness of the filling process. Indeed, the absence of features of a double layer excludes the possibility of a thick *PAN*I layer onto the external *PSi* surface, indicating the presence of the polymer inside the porous structure.
Fig. 60 shows the spectra of crystalline *Si* and crystalline *Si* submitted to direct aniline electropolymerization (*PANI/Crystalline Silicon*) and

crystalline Si modified with aryl underlayer (*PANI/Ar/Crystalline Silicon*) before aniline electropolymerization.

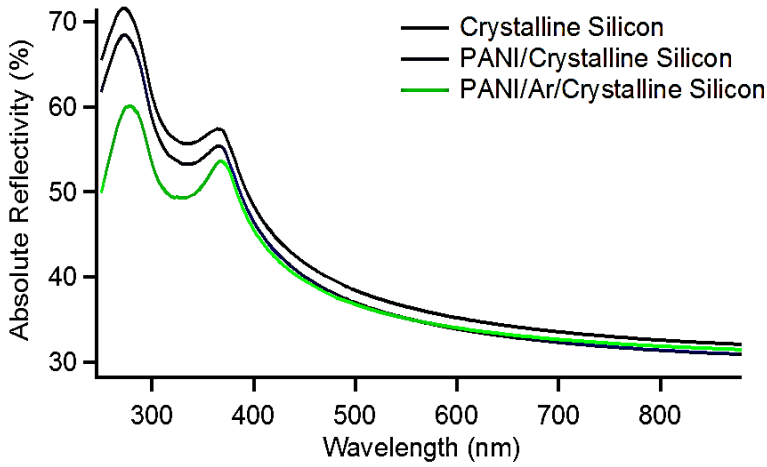

Fig. 60 *Reflectivity spectra of crystalline Si (black curve), crystalline Si submitted to direct aniline electropolymerization (blue curve) and crystalline Si with aryl underlayer before aniline electropolymerization (green curve).* [180]

As can be seen no interference fringes can be appreciated, but changes in the reflectivity spectra are present in the region of wavelengths shorter than 1100nm, which can be attributed to the optical response of *PANI*.

Morphologic characterization

In order to gather information about the presence of *PANI* inside the pores of the samples, SEM images were collected on *PSi* (***Fig. 61a***) and *PANI/Ar/PSi*. (***Fig. 61b***)
As can be observed a homogeneous coverage of the polymer on the overall Psi surface can be appreciated.
In spite of all, with this technique only a qualitative information can be obtained.

In order to obtain a quantitative estimate of the *PANI* content inside Si pores, in collaboration with the University of Pavia the reflectivity data from bulk Si with and without *PANI* and *PSi* with and without *PANI* have been analyzed.

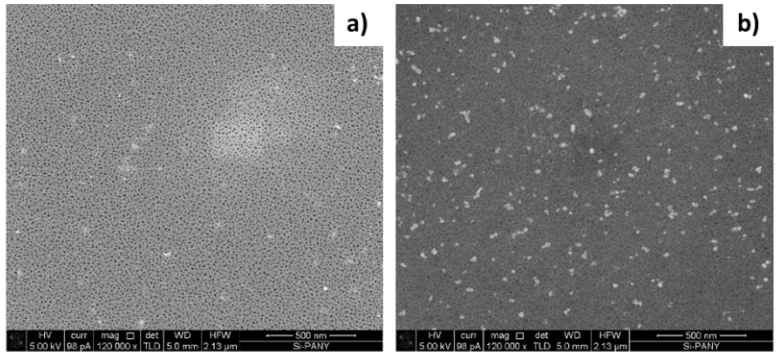

Fig. 61 *SEM of PSi (a) and PANI/Ar/PSi (b).The electropolymerization was performed at 30 mV* s^{-1}.

An optical simulation was performed through WVASE® software by J.A. Woollam Co. Inc. Then, the reflectivity data presented ***Fig. 58, Fig. 9*** and ***Fig. 60*** were analyzed, modelling the presence of *PANI* within the porous layer.

The analyses demonstrated that *PANI* was present in the whole layer both with and without the aryl underlayer, while there was a gradient in the *PANI* concentration along the samples thickness. The gradient was expected as in common in all thin filling processes. In case of *PANI/Ar/Psi* the concentration gradient was such that the bottom concentration was estimated to be about one third of the surface concentration. The *PANI* filling was evaluated as filling about 80% of the pores inner volume, on a homogeneous layer fitting, i.e. without considering concentration gradients. This also was expected, because of the dendritic structure of the *PSi* pores that makes difficult to aniline to fill the whole available volume portion.

The reflectivity data fitting confirmed the presence of the *PANI* in the whole structure and moreover, indicated that a concentration gradient was also present. Comparing the results of the simulation of the reflectivity spectra

of the samples with and without aryl layer, a decrease of the *PANI* amount was observed when the underlayer was not present.
Although a reliable quantitative estimation of the *PANI* content is not simple to evaluate with only the simulation of reflectivity spectra, this rough estimate suggests that the amount of *PANI* in *PANI/PSi* was less than two times the corresponding in *PANI/Ar/PSi*.
These results demonstrate that at aminophenyl modified *PSi* the polymerization process is more effective.
A more detailed concentration study with ellipsometry should give a more precise determination of the *PANI* concentration gradient. Then, a more detailed study of the *PANI* filling within the pores as a function of the preparation parameters has already be planned.

Photocurrent measurements

In order to gather information about the photoactivity of the samples, photocurrent measurements were carried out; the results are shown in ***Fig. 62***. As can be seen an higher light absorption in the visible range can be appreciated in case of *PANI/Ar/PSi*, compared to the empty porous Si. This means that a *p-n* junction was present between *PANI* and *PSi* and that the presence of the organic layer between them improved light absorption in the visible range (***Fig. 62a).*** Also the absolute white-light photocurrent was also higher for the hybrid heterojunction. *PANI/Ar/PSi* showed a distinct photosensitivity, higher by one order of magnitude with respect to pristine *PSi*. A different behaviour can be observed in case of *PANI/PSi* (***Fig. 62 b***): the photo-response (yellow curve) is comparable to that of the pristine porous silicon and the sample does not show the increase in absorbance observed with *PANI/Ar/ PSi* in the visible range (wavelengths between 400 and 800 nm).
These results demonstrate the importance that the organic underlayer plays in the formation of the hybrid structure. As a matter of fact, without underlayer it seems that the photocarrier generation contribution from the *PANI* content of the pore is negligible, while it is significant when *PANI*

electropolymerization is performed in a sample where the organic underlayer has been previously electrodeposited.
This might be due to the inefficiency of the interfacial junction between the organic and the inorganic components without aminophenyl layer, that may hampers the photocarriers generated within *PANI* layer to cross the interface.

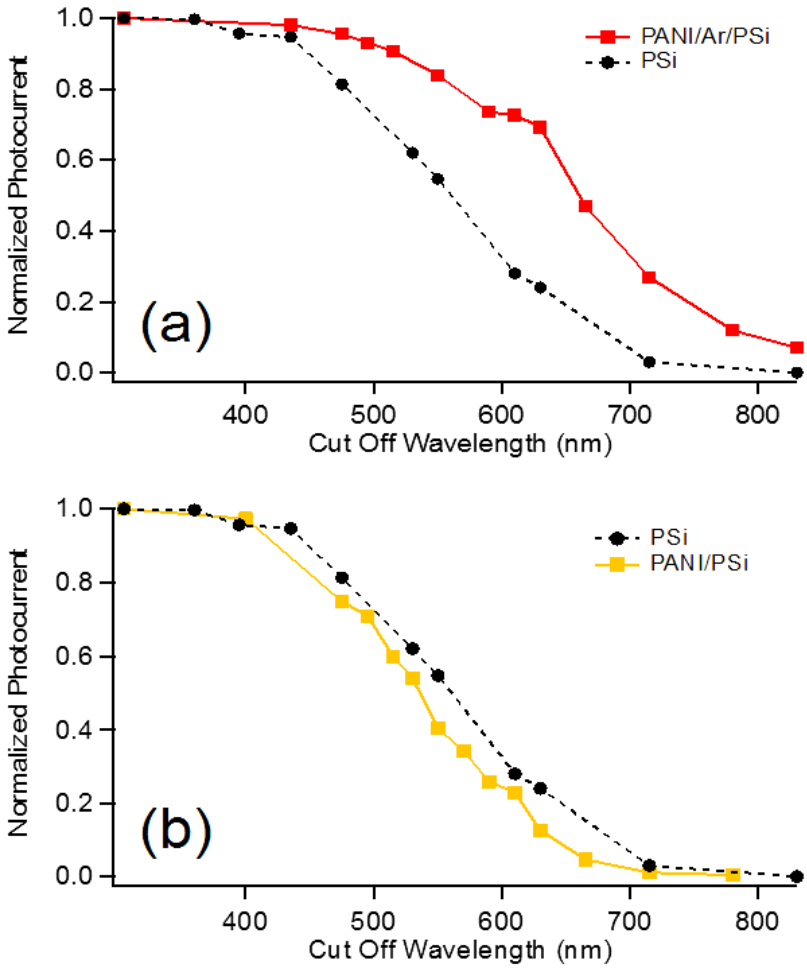

Fig. 62 *Comparison between normalized photocurrents of PSi and PANI/Ar/PSi (a) and PSi and PANI/PSi (b).* [180]

In order to study the effect of different operative conditions, as the scan rate and the number of cycles of electropolymerization on the photocurrent,

different *PANI/Ar/PSi* samples have been developed using several scan rates for the electropolymerization step. The experimental conditions concerning both the NBD grafting and NBD reduction phase were not modified.

Fig. 63 shows the second electropolymerization scan at different scan rate: as can be observed the current intensity of the redox peaks indicating *PANI* polymerization are well visible and they increase with the scan rate, showing that *PANI* growth occurs under each examined condition.

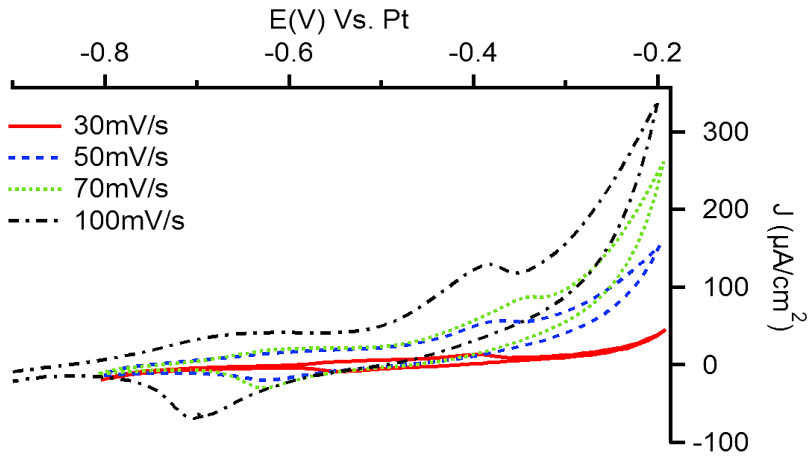

Fig. 63: *Cyclic voltammogramms (2nd cycle) recorded during electropolymerization of aniline in 0.1M $HClO_4$ + 0.1M aniline in acetonitrile media on PSi electrode after NBD reduction at the scan rate of 30, 50, 70 and 100 mV/s.* [180]

Fig. 64a and ***Fig. 64b*** show the photocurrents obtained for *PANI /Ar/PSi* samples prepared with different scan rates and number of voltammetric cycles. Specifically a scan rate and a number of cycles of: 30, 50, 70,100 mV and 10, 5 and 4 CV have been used, respectively.

As can be observed differences in the absolute value of the photocurrent are well visible: in particular, the photocurrent increases:

- when the scan rate decreases
- with the number of cycles, when the scan rate is fixed.

It is well known that such characteristics as morphology, conductivity and rate of the polyaniline growth are strongly dependent on the operative conditions. [147–149]

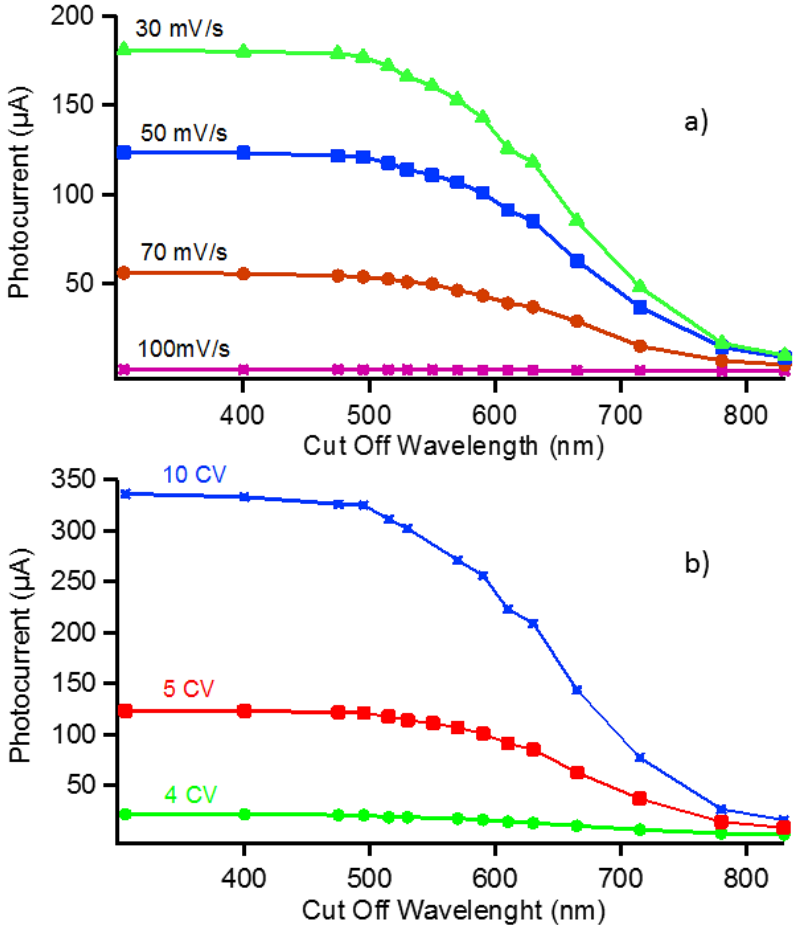

Fig. 64 *Normalized photocurrent recorded on PANI/Ar/PSi samples realized with five CV at scan rate of: 30 mV/s (in green), 50 mV/s (in blue), 70 (in orange)and 100 mV/s (in purple) (a); at 30 mV/s of scan rate and different number of cycles: 10 CV(in blue), 5 CV (in red), 4 CV (in green) (b).* [180]

When potentiodynamic electrodeposition is employed, the scan rate can play an important role; as reported in *Background section* the growth mechanism of *PANI* may occur via three different dimerization paths (i.e., head-to-head, head-to-tail, and tail to-tail), as well as competitive degradation reactions.[146] Depending on the scan rate, the formation of *PANI* can be controlled by the fastest reaction (i.e., head-to-tail polymerization) or by the secondary reactions (e.g., tail-to-tail, head-to-head polymerizations, degradation reactions). In this specific case further issues complicate the process, since the polymerization occurs in a porous structure, where diffusion effects overlap the kinetics aspect. The number of CV cycles also affects the overall efficiency of the system: as shown in ***Fig. 64b*** keeping constant the scan rate at 30mV/s the efficiency increases with the number of CV cycles.

Study of PANI pH switching behaviour

In order to investigate if there was reversibility between the protonated and deprotoneted *PANI* form (emeraldine salt and base, respectively), the *PSi/Ar/PANI* samples have first been dipped in a basic solution (acetonitrile solution containing 0.1 M NH_3; pH=9) and then in an acid solution (acetonitrile solution containing 0.1 M $HClO_4$; pH=4).
It is important to remember that after the aniline electropolymerization, *PANI* is in the emeraldine salt form, the *p*-type *PANI* protonated form, since it has been electropolymerized in acid media. After each dipping step, the photocurrent was recorded. As can be seen in ***Fig. 65*** the photocurrent decreases after dipping in basic solutions.
This behaviour can be explained with the probable transformation of the *p*-type protonated *PANI* form at least partially in *p*-type deprotonated form, that causes a decreasing of the *p-n* junction efficiency.
After the second dipping in acid media *PANI* partially acquires again its starting *p*-type protonated form as it is suggested from the photocurrent results**.**
This demonstrates the possibility to modify the *PANI/PSi* photocurrent efficiency by a doping/de-doping process controlled by the pH.

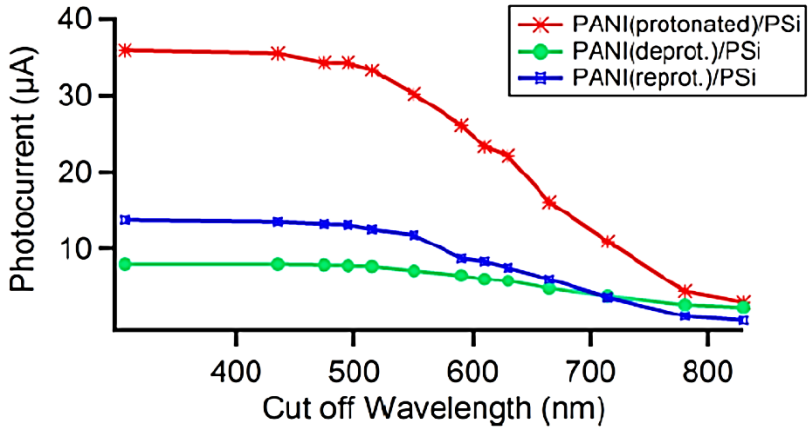

Fig. 65 *Normalized photocurrent response of a PANI/PSi heterojunction after electropolymerization (in red) and after dipping in basic and acid solutions (green and blue curve, respectively).*

3.6. Conclusions

It was demonstrated that the porous silicon electrodes *PSi* can be successfully functionalized by an approach based on electrochemical grafting of 4-NBD salts. The 4-NBD was electrodeposited using both CV and potentiostatic methods.

It was demonstrated that the functionalization process widely increase the chemical resistance of the *PSi* layers towards harsh alkaline solutions: the samples stay unmodified up to about 40 min. The voltammetric deposition of NBD allows to significant improve the chemical resistance with respect to the potentiostatic grafting method, multiplying by at least a factor of four the maximum dipping time.

The obtained open pores structure has allowed to further functionalize the samples surfaces: *PSi* samples modified with NBD were undergone to two electrochemical functionalization steps in order to develop a hybrid *PANI/PSi* heterojunction. In the second step, the nitro groups were successfully electrochemically reduced to amino groups and in the last step, aniline polymerization was performed on the surface of the aminophenyl-modified *PSi*.

The result show that phenyl amine promotes the polymerization of aniline and that the covalent bond between the organic and the *PSi* is the principal responsible for the formation of an effective p-n heterojunction.

Moreover, the results show that the as-prepared heterojunctions exhibit an increased light absorption capability in the visible range, with respect to *PSi* alone and generate higher photocurrents (more than one order of magnitude) in the whole spectrum.

The photoactivity of samples obtained by simple electropolymerization of aniline on *PSi*, without organic underlayer, resulted virtually equal to those of pristine *PSi*.

Furthermore, it was demonstrated that he photocurrent efficiency can be modified by setting the polymerization conditions, namely scan rate and number of voltammetric cycle.

Under the conditions adopted the coatings obtained at scan rates of 30 mV s^{1} and with 10 voltammetric cycles of polymerization, showed the highest capability to efficiently photogenerate carriers from light, from the visible to the near-infrared region.

Finally, it was also demonstrated the possibility to modify the *PANI/PSi* photocurrent efficiency by a doping/de-doping process controlled by the pH.

Chapter 4

Final considerations and further investigations

In this PhD project the synthesis of nanoporous nickel electrodes and *PSi/PANI* heterojunctions through electrochemical techniques have been successfully accomplished.
The former material was developed by an electrochemical easy method that has allowed obtaining several pores morphologies and structures with different range of porosity.
It was demonstrated that the as-prepared samples can be effectively adopted as anodes for *OER* and removal of organic compounds as well as cathodes for *HER* and photocathodes.
Evidences about the improvement of both the activity and photoactivity of the electrodes with the extension of the active surface area are reported.
The results suggest also that the resulting morphology and chemical structure affect positively both the electroactivity and photoactivity of the electrodes.
Further developments of this research will regard the study of a n-type photoanode to couple with the p-type photocathode prepared with the strategy proposed in this research project. The resulting p-n system should be suitable for other interesting photoelectrochemical applications including organic light-emitting diodes, photovoltaic solar cells and tandem p/n type devices in general.
The second material object of this PhD thesis was porous silicon: it was functionalized by an electrochemical approach based on 4-NBD salts.
This method has allowed obtaining porous silicon samples with strong resistance to the etching solutions, typically used in optical lithography. In this scenario, the electrochemical group of the University of Turin

successfully patterned a matrix of electrical contacts on porous silicon samples treated with 4-NBD, using standard optical lithography.
The results showed that the 4-NBD samples maintained open pores after the grafting, making them suitable for further treatments, which can be useful for a large variety of applications that requires stable substrates.
In this context in this PhD project an efficient pore filling with polyaniline was performed. The resulting p-n system showed an enhanced light absorption capability in the visible range: characteristic remarkably useful for energy/solar- related applications. Moreover, it was also demonstrated the possibility to modify the photocurrent efficiency of *PANI/PSi* heterojunction by a doping/de-doping process controlled by the pH. This can be used for instance, to build a photovoltaic pH sensor.
The same strategy could be applied to different conducting polymers of interest for energy conversion and bio-sensing applications.

Bibliography

1 J. Erlebacher and R. Seshadri, *MRS Bull.*, 2009, **34**, 561–568.

2 A. Wittstock, J. Biener and M. Bäumer, *Phys. Chem. Chem. Phys.*, 2010, **12**, 12919–12930.

3 Y. Yamauchi, N. Suzuki, L. Radhakrishnan and L. Wang, *Chem. Rec.*, 2010, **9**, 321–339.

4 C.-J. Zhong, J. Luo, B. Fang, B. N. Wanjala, P. N. Njoki, R. Loukrakpam and J. Yin, *Nanotechnology*, 2010, **21**, 62001.

5 X. Lang, A. Hirata, T. Fujita and M. Chen, *Nat Nanotechnol*, 2011, **6**, 232–236.

6 X. T. Zheng and C. M. Li, *Chem. Soc. Rev.*, 2012, **41**, 2061–71.

7 J. H. Bang and P. V. Kamat, *Adv. Funct. Mater.*, 2010, **20**, 1970–1976.

8 J. He, H. Lindström, A. Hagfeldt and S. E. Lindquist, *Sol. Energy Mater. Sol. Cells*, 2000, **62**, 265–273.

9 S. K. Karuturi, J. Luo, C. Cheng, L. Liu, L. T. Su, A. I. Y. Tok and H. J. Fan, *Adv. Mater.*, 2012, **24**, 4157–4162.

10 Y. Qu, W. Zhou, X. Miao, Y. Li, L. Jiang, K. Pan, G. Tian, Z. Ren, G. Wang and H. Fu, *Chem. - An Asian J.*, 2013, **8**, 3085–3090.

11 K. Tennakone, G. R. R. A. Kumara, A. R. Kumarasinghe, K. G. U. Wijayantha and P. M. Sirimanne, *Semicond. Sci. Technol.*, 1995, **10**, 1689–1693.

12 J. Erlebacher, M. J. Aziz, a Karma, N. Dimitrov and K. Sieradzki, *Nature*, 2001, **410**, 450–453.

13 A. Kloke, F. Von Stetten, R. Zengerle and S. Kerzenmacher, *Adv.*

Mater., 2011, **23**, 4976–5008.

14 O. D. Velev, P. M. Tessier, a. M. Lenhoff and E. W. Kaler, *Nature*, 1999, **401**, 548.

15 P. V. Braun and P. Wiltzius, *Curr. Opin. Colloid Interface Sci.*, 2002, **7**, 116–123.

16 Y. Yamauchi and K. Kuroda, *Chem. - An Asian J.*, 2008, **3**, 664–676.

17 X. Lang, A. Hirata, T. Fujita and M. Chen, *Nat Nanotechnol*, 2011, **6**, 232–236.

18 A. Stein, F. Li and N. R. Denny, *Chem. Mater.*, 2008, **20**, 649–666.

19 K. M. Kulinowski, P. Jiang, H. Vaswani and V. L. Colvin, *Adv. Mater.*, 2000, **12**, 833–838.

20 X. S. Zhao, F. Su, Q. Yan, W. Guo, X. Y. Bao, L. Lv and Z. Zhou, *J. Mater. Chem.*, 2006, **16**, 637.

21 H. Ataee-Esfahani, L. Wang, Y. Nemoto and Y. Yamauchi, *Chem. Mater.*, 2010, **22**, 6310–6318.

22 Y. Song, Y. Yang, C. J. Medforth, E. Pereira, A. K. Singh, H. Xu, Y. Jiang, C. J. Brinker, F. Van Swol and J. A. Shelnutt, *J. Am. Chem. Soc.*, 2004, **126**, 635–645.

23 F. Kertis, J. Snyder, Lata Govada, Sahir Khurshid, N. Chayen, J. Erlebacher, JOM., 2010, 62, 51-56.

24 Y. Ding and M. Chen, *MRS Bull.*, 2009, **34**, 569–576.

25 J. Zhang and C. M. Li, *Chem. Soc. Rev.*, 2012, **41**, 7016.

26 H. Adkins and H. R. Billica, *J. Am. Chem. Soc.*, 1948, **70**, 695–698.

27 D. E. Lieberman, *Writing*, 2001, **410**, 20–22.

28 A. Pareek, S. Borodin, A. Bashir, G. N. Ankah, P. Keil, G. A. Eckstein, M. Rohwerder, M. Stratmann, Y. Gründer and F. U.

Renner, *J. Am. Chem. Soc.*, 2011, **133**, 18264–71.

29 C. Yu, L. Zhang, J. Shi, J. Zhao, J. Gao and D. Yan, *Adv. Funct. Mater.*, 2008, **18**, 1544–1554.

30 A. Pareek, S. Borodin, A. Bashir, G. N. Ankah, P. Keil, G. A. Eckstein, M. Rohwerder, M. Stratmann, Y. Gründer and F. U. Renner, *J. Am. Chem. Soc.*, 2011, **133**, 18264–71.

31 H.-J. Qiu, H.-T. Xu, L. Liu and Y. Wang, *Nanoscale*, 2015, **7**, 386–400.

32 C. K. Tsang, Z. Xu and Y. Y. Li, *J. Electrochem. Soc.*, 2009, **156**, D508.

33 I. Herraiz-Cardona, E. Ortega and V. Pérez-Herranz, *Electrochim. Acta*, 2011, **56**, 1308–1315.

34 I. Herraiz-Cardona, E. Ortega, L. Vázquez-Gómez and V. Pérez-Herranz, *Int. J. Hydrogen Energy*, 2012, **37**, 2147–2156.

35 K. R. Koboski, E. F. Nelsen and J. R. Hampton, *Nanoscale Res. Lett.*, 2013, **8**, 528.

36 P. Los, A. Lasia, H. Ménard and L. Brossard, *J. Electroanal. Chem.*, 1993, **360**, 101–118.

37 A. Kellenberger, N. Vaszilcsin and W. Brandl, *J. Solid State Electrochem.*, 2006, **11**, 84–89.

38 V. N. Kuleshov, N. V. Kuleshov, S. A. Grigoriev, E. Y. Udris, P. Millet and A. S. Grigoriev, *Int. J. Hydrogen Energy*, 2016, **41**, 36–45.

39 C. Hitz and A. Lasia, *J. Electroanal. Chem.*, 2001, **500**, 213–222.

40 F. Safizadeh, E. Ghali and G. Houlachi, *Int. J. Hydrogen Energy*, 2015, **40**, 256–274.

41 J. Cai, J. Xu, J. Wang, L. Zhang, H. Zhou, Y. Zhong, D. Chen, H.

Fan, H. Shao, J. Zhang and C. N. Cao, *Int. J. Hydrogen Energy*, 2013, **38**, 934–941.

42 H. Ju, Z. Li and Y. Xu, *Mater. Res. Bull.*, 2015, **64**, 171–174.

43 M. E. G. Lyons and M. P. Brandon, *Int. J. Electrochem. Sci.*, 2008, **3**, 1386–1424.

44 M. F. Kibria and M. S. Mridha, *Int. J. Hydrogen Energy*, 1996, **21**, 179–182.

45 D. K. Bediako, Y. Surendranath and D. G. Nocera, *J. Am. Chem. Soc.*, 2013, **135**, 3662–3674.

46 K. Juodkazis, J. Juodkazyt and R. Vilkauskait, 2008, 1469–1479.

47 J. Zhang, Y. Zhan, H. Bian, Z. Li, C. K. Tsang, C. Lee, H. Cheng, S. Shu, Y. Y. Li and J. Lu, *J. Power Sources*, 2014, **257**, 374–379.

48 W. Sheng, H. a. Gasteiger and Y. Shao-Horn, *J. Electrochem. Soc.*, 2010, **157**, B1529.

49 P. Rasiyah and A. C. C. Tseung, *J. Electrochem. Soc.*, 1984, **131**, 803–808.

50 M. Fleischmann, K. Korinek and D. Pletcher, *J. Electroanal. Chem.*, 1972, **34**, 499–503.

51 V. N. Kuleshov, N. V. Kuleshov, S. A. Grigoriev, E. Y. Udris, P. Millet and A. S. Grigoriev, *Int. J. Hydrogen Energy*, 2016, **41**, 36–45.

52 L. A. Hutton, M. Vidotti, A. N. Patel, M. E. Newton, P. R. Unwin and J. V. MacPherson, *J. Phys. Chem. C*, 2011, **115**, 1649–1658.

53 S. L. Medway, C. A. Lucas, A. Kowal, R. J. Nichols and D. Johnson, *J. Electroanal. Chem.*, 2006, **587**, 172–181.

54 O. Simond, V. Schaller and C. Comninellis, *Electrochim. Acta*, 1997, **42**, 2009–2012.

55 X. Lu and C. Zhao, *Nat. Commun.*, 2015, **6**, 1–7.

56 B. O'Regan and M. Grätzel, *Nature*, 1991, **353**, 737–740.

57 a Fujishima and K. Honda, *Nature*, 1972, **238**, 37–38.

58 C. Ng, A. Iwase, Y. H. Ng and R. Amal, *ChemSusChem*, 2013, **6**, 291–298.

59 Z. Zhang, C. Shao, X. Li, C. Wang, M. Zhang and Y. Liu, *ACS Appl. Mater. Interfaces*, 2010, **2**, 2915–2923.

60 J. A. Seabold and K. S. Choi, *Chem. Mater.*, 2011, **23**, 1105–1112.

61 X. Yang, A. Wolcott, G. Wang, A. Sobo, R. C. Fitzmorris, F. Qian, J. Z. Zhang and Y. Li, *Nano Lett.*, 2009, **9**, 2331–2336.

62 K. Sivula, F. Le Formal and M. Grätzel, *ChemSusChem*, 2011, **4**, 432–449.

63 Q. Jia, K. Iwashina and A. Kudo, *Pnas*, 2012, **109**, 11564–11569.

64 P. M. Nwanya, A. C., Ezema, F. I. and Ejikeme, *Int. J. Phys. Sci.*, 2011, **6**, 5190–5201.

65 C. Hu, K. Chu, Y. Zhao and W. Y. Teoh, *ACS Appl. Mater. Interfaces*, 2014, **6**, 18558–18568.

66 D. a. Wruck, *J. Electrochem. Soc.*, 1993, **140**, 1097–1104.

67 F. Odobel, L. Le Pleux, Y. Pellegrin and E. Blart, *Acc. Chem. Res.*, 2010, **43**, 1063–1071.

68 A. Nattestad, A. J. Mozer, M. K. R. Fischer, Y. Cheng, A. Mishra, P. Bäuerle and U. Bach, *ChemSusChem*, 2010, **3**, 304.

69 P. Qin, H. Zhu, T. Edvinsson, G. Boschloo, A. Hagfeldt and L. Sun, *J. Am. Chem. Soc.*, 2008, **130**, 8570–8571.

70 E. A. Gibson, L. Le Pleux, J. Fortage, Y. Pellegrin, E. Blart, F. Odobel, A. Hagfeldt and G. Boschloo, *Langmuir*, 2012, **28**, 6485–6493.

71 H. Zheng, T. Zhai, M. Yu, S. Xie, C. Liang, W. Zhao, S. C. I. Wang, Z. Zhang and X. Lu, *J. Mater. Chem. C*, 2013, **1**, 225–229.

72 W. Zhou, F. Sun, K. Pan, G. Tian, B. Jiang, Z. Ren, C. Tian and H. Fu, *Adv. Funct. Mater.*, 2011, **21**, 1922–1930.

73 L. Lepleux, B. Chavillon, Y. Pellegrini, E. Blart, L. Cario, S. Jobic and F. Odobel, *Inorg. Chem.*, 2009, 48, 8245–8250.

74 Y. Qu, W. Zhou, K. Pan, C. Tian, Z. Ren, Y. Dong and H. Fu, *Phys. Chem. Chem. Phys.*, 2010, **12**, 9205–12.

75 D. A. Corrigan and R. M. Bendert, *J. Electrochem. Soc.*, 1989, **136**, 723–728.

76 J. K. Chang, S. N. Hsu, I. W. Sun and W. T. Tsai, *J. Phys. Chem. C*, 2008, **112**, 1371–1376.

77 L. Sun, C. L. Chien and P. C. Searson, *Chem. Mater.*, 2004, **16**, 3125–3129.

78 E. Sechi, A. Vacca, M. Mascia and S. Palmas, 2016, **47**, 97–102.

79 A. M. Zaky, *Univers. J. Chem.*, 2013, **1**, 1–6.

80 A. Jouanneau, M. Keddam and M. C. Petit, *Electrochim. Acta*, 1976, **21**, 287–292.

81 P. Schmuki, *J. Solid State Electrochem.*, 2002, **6**, 145–164.

82 L. M. Da Silva, L. A. De Faria and J. F. C. Boodts, *Electrochim. Acta*, 2001, **47**, 395–403.

83 P. Danielsson, J. Bobacka and A. Ivaska, *J. Solid State Electrochem.*, 2004, **8**, 809–817.

84 S. Palmas, M. Mascia, A. Vacca, J. Llanos and E. Mena, *RSC Adv.*, 2014, **4**, 23957.

85 X. Jin and J. Lu, *J. Power Sources*, 2001, **93**, 8–13.

86 S. Trasatti and O. A. Petrii, *J. Electroanal. Chem.*, 1992, **327**, 353–

376.

87 M. El Baydi, S. K. Tiwari, R. N. Singh, J.-L. Rehspringer, P. Chartier, J. F. Koenig and G. Poillerat, *J. Solid State Chem.*, 1995, **116**, 157–169.

88 R. K. Shervedani and a Lasia, *J. Appl. Electrochem.*, 1999, **29**, 979–986.

89 D. Marin, F. Mendicuti and C. Teijeiro, *Journal of Chemical Education*, 1994, **71**, 4–5.

90 R. A. and L. A., *J. appied Electrochem.*, 1992, **22**, 376.

91 I. Herraiz-Cardona, E. Ortega, J. G. Antón and V. Pérez-Herranz, *Int. J. Hydrogen Energy*, 2011, **36**, 9428–9438.

92 J. Kubisztal and A. Budniok, *Int. J. Hydrogen Energy*, 2008, **33**, 4488–4494.

93 Y. Miao, L. Ouyang, S. Zhou, L. Xu, Z. Yang, M. Xiao and R. Ouyang, *Biosens. Bioelectron.*, 2014, **53**, 428–439.

94 R. D. Armstrong and M. Henderson, *Electroanalytical Chemistry and InterJacial Electrochemistry*.,1972, **39**, 81-90.

95 G. J. Brug, A. L. G. van den Eeden, M. Sluyters-Rehbach and J. H. Sluyters, *J. Electroanal. Chem.*, 1984, **176**, 275–295.

96 Y. Choquette, L. Brossard, A. Lasia and H. Ménard, *Electrochim. Acta*, 1990, **35**, 1251–1256.

97 H. M. Y. Choquette, L. Brossard, A. Lasia, *J. Electrochem. Soc.*, 1990, **137**, 1723–1730.

98 L. L. Chen and A. Lasia, *J. Electrochem. Soc.*, 1992, **139**, 3214–3219.

99 P. Chang YC, *J. Electrochem. Soc.*, 1989, **38(4)**, 890–894.

100 L. Daikhin, a. Kornyshev and M. Urbakh, *Phys. Rev. E*, 1996, **53**,

6192–6199.

101 K. Ngamlerdpokin and N. Tantavichet, *Int. J. Hydrogen Energy*, 2014, **39**, 2505–2515.

102 S. Kim, J. Lee, H. Ahn, H. Song and J. Jang, *ACS Appl Mater Inter*, 2013, **5**, 1595–1603.

103 W. Y. Teoh, J. A. Scott and R. Amal, *J. Phys. Chem. Lett.*, 2012, **3**, 629–639.

104 U. A. Joshi and P. A. Maggard, *J. Phys. Chem. Lett.*, 2012, **3**, 1577–1581.

105 A. Morandeira, T. Edvinsson, L. Pleux, E. Blart, G. Boschloo, A. Hagfeldt and L. Hammarstro, 2008, **112**,1721–1728.

106 S. Kango, S. Kalia, A. Celli, J. Njuguna, Y. Habibi and R. Kumar, *Prog. Polym. Sci.*, 2013, **38**, 1232–1261.

107 F. A. El Hadj, A. Amiar, M. Cherkaoui, J. N. Chazalviel and F. Ozanam, *Electrochim. Acta*, 2012, **70**, 318–324.

108 C. Bourdillon, M. Delamar, C. Demaille, R. Hitmi, J. Moiroux and J. Pinson, *J. Electroanal. Chem.*, 1992, **336**, 113–123.

109 J. Pinson and F. Podvorica, *Chem. Soc. Rev.*, 2005, **34**, 429–439.

110 A. Vacca, M. Mascia, S. Rizzardini, S. Palmas and L. Mais, *Electrochim. Acta*, 2014, **126**, 81–89.

111 M. Ceccato, A. Bousquet, M. Hinge, S. U. Pedersen and K. Daasbjerg, *Chem. Mater.*, 2011, **23**, 1551–1557.

112 C. Combellas, F. Kanoufi, J. Pinson and F. I. Podvorica, *Langmuir*, 2005, **21**, 280–286.

113 O. Fontaine, J. Ghilane, P. Martin, J. C. Lacroix and H. Randriamahazaka, *Langmuir*, 2010, **26**, 18542–18549.

114 P. Actis, G. Caulliez, G. Shul, M. Opallo, M. Mermoux, B. Marcus, R. Boukherroub and S. Szunerits, *Langmuir*, 2008, **24**, 6327–6333.

115 J. Ghilane, P. Martin, O. Fontaine, J. C. Lacroix and H. Randriamahazaka, *Electrochem. commun.*, 2008, **10**, 1060–1063.

116 J. O. Estevez and V. Agarwal, *Handb. Porous Silicon*, 2014, 805–814.

117 C. Lai, X. Li, D. Zhang, Z. Xiang, W. Yang and X. Guo, *Mater. Chem. Phys.*, 2014, **144**, 355–360.

118 J. Salonen, V. P. Lehto, M. Björkqvist, E. Laine and L. Niinistö, *Phys. Status Solidi Appl. Res.*, 2000, **182**, 123–126.

119 J. Salonen, E. Laine and L. Niinistö, *J. Appl. Phys.*, 2002, **91**, 456–461.

120 M. Björkqvist, J. Salonen, J. Paski and E. Laine, *Sensors Actuators, A Phys.*, 2004, **112**, 244–247.

121 M. Ohmukai, K. Okada and Y. Tsutsumi, *J. Mater. Sci. Mater. Electron.*, 2005, **16**, 119–121.

122 S. Setzu, P. Ferrand, G. Lérondel and R. Romestain, *Appl. Surf. Sci.*, 2002, **186**, 588–593.

123 G. Aggarwal, P. Mishra, B. Joshi, Harsh and S. S. Islam, *J. Porous Mater.*, 2014, **21**, 23–29.

124 S. Chatterjee, R. Carter, L. Oakes, W. R. Erwin, R. Bardhan and C. L. Pint, *J. Phys. Chem. C*, 2014, **118**, 10893–10902.

125 J. Salonen, M. Björkqvist, E. Laine and L. Niinistö, *Appl. Surf. Sci.*, 2004, **225**, 389–394.

126 I. N. Lees, H. Lin, C. A. Canaria, C. Gurtner, M. J. Sailor and G. M. Miskelly, *Langmuir*, 2003, **19**, 9812–9817.

127 J. T. C. Wojtyk, K. a Morin, R. Boukherroub and D. D. M. Wayner, *Society*, 2002, **18**, 6081–6087.

128 L. De Stefano, E. De Tommasi, I. Rea, L. Rotiroti, M. Canciello, G.

Maglio and R. Palumbo, *Appl. Phys. A Mater. Sci. Process.*, 2010, **98**, 525–530.

129 P. Allongue, C. H. de Villeneuve, J. Pinson, F. Ozanam, J. N. Chazalviel and X. Wallart, *Electrochim. Acta*, 1998, **43**, 2791–2798.

130 M. P. Stewart, F. Maya, D. V Kosynkin, S. M. Dirk, J. J. Stapleton, C. L. McGuiness, D. L. ALLARA and J. M. Tour, *J. Am. Chem. Soc.*, 2004, **126**, 370–378.

131 D. Wang and J. M. Buriak, *Langmuir*, 2006, **22**, 6214–6221.

132 K. Roodenko, F. Yang, R. Hunger, N. Esser, K. Hinrichs and J. Rappich, *Surf. Sci.*, 2010, **604**, 1623–1627.

133 M. Tiddia, G. Mula, E. Sechi, A. Vacca, E. Cara, N. De Leo, M. Fretto and L. Boarino, *Nanoscale Res. Lett.*, 2016, **11**, 436.

134 A. G. MacDiarmid, *Synth. Met.*, 2001, **125**, 11–22.

135 B. Wessling, D. Srinivasan, G. Rangarajan, T. Mietzner and W. Lennartz, *Eur. Phys. J. E*, 2000, **2**, 207–210.

136 A. G. Macdiarmid, J. Chiang, W. Huang and S. Mu, 1985, 37–41.

137 D. W. Wang, F. Li, J. Zhao, W. Ren, Z. G. Chen, J. Tan, Z. S. Wu, I. Gentle, G. Q. Lu and H. M. Cheng, *ACS Nano*, 2009, **3**, 1745–1752.

138 W. Hou, Y. Xiao, G. Han, D. Fu and R. Wu, *J. Power Sources*, 2016, **322**, 155–162.

139 P. Cavallo, E. Frontera, D. F. Acevedo, R. Olejnik, P. Slobodian, P. Saha and C. A. Barbero, *Synth. Met.*, 2016, **215**, 127–133.

140 A. R. Elkais, M. M. Gvozdenović, B. Z. Jugović, J. S. Stevanović, N. D. Nikolić and B. N. Grgur, *Prog. Org. Coatings*, 2011, **71**, 32–35.

141 J. Stejskal, I. Sapurina and M. Trchová, *Prog. Polym. Sci.*, 2010, **35**, 1420–1481.

142 T. P. Wallace G., Spinks G., Kane-Maguire L., *Conductive Electroactive Polymers*, .

143 S. Bhadra, D. Khastgir, N. K. Singha and J. H. Lee, *Prog. Polym. Sci.*, 2009, **34**, 783–810.

144 C. Hu and C. Chu, *J. Electroanal. Chem.*, 2001, **503**, 105–116.

145 K. Aoki and M. Kawase, *J. Electroanal. Chem.*, 1994, **377**, 125–129.

146 H. C. Budnikov, G. A. Evtugyn and A. V. Porfireva, *Talanta*, 2012, **102**, 137–155.

147 R. Córdova, M. A. del Valle, A. Arratia, H. Gómez and R. Schrebler, *J. Electroanal. Chem.*, 1994, **377**, 75–83.

148 J. L. Camalet, J. C. Lacroix, T. D. Nguyen, S. Aeiyach, M. C. Pham, J. Petitjean and P. C. Lacaze, *J. Electroanal. Chem.*, 2000, **485**, 13–20.

149 T. Chimiche, R. Vergata, E. Pan, T. Pt, S. E. Interface, E. Interface and R. One, *Electrochim. Acta*, 1988, **34**, 223–228.

150 A. Ali Ramadan Elkais Milica M. Gvozdenović, Branimir Z. Jugović, Jasmina S. Stevanović, Tomislav Lj. Trišović and Branimir N. Grgur, Progress in Organic Coatings, 2011, **71**, 32-35.

151 G. S. Higashi, K. Raghavachari, F. Ozanam, J. N. Chazalviel, T. Journal, S. R. Wenham and M. A. Green, 1991, **138**, 1989–1992.

152 a Guiseppi-Elie, S. R. Pradhan, a M. Wilson, D. L. Allara, P. Zhang, R. W. Collins and Y. T. Kim, *Chem. Mater.*, 1993, **5**, 1474–1480.

153 S. Matsumura, A. R. Hlil, C. Lepiller, J. Gaudet, D. Guay, Z. Shi, S. Holdcroft and A. S. Hay, *Am. Chem. Soc. Polym. Prepr. Div. Polym. Chem.*, 2008, **49**, 511–512.

154 V. Gupta and N. Miura, *Electrochem. commun.*, 2005, **7**, 995–999.

155 V. Rajendran, A. Gopalan, T. Vasudevan, W. C. Chen and T. C. Wen, *Mater. Chem. Phys.*, 2000, **65**, 320–328.

156 G. S. Popkirov, E. Barsoukov and R. N. Schindler, *J. Electroanal. Chem.*, 1997, **425**, 209–216.

157 A. A. Hermas, M. Nakayama and K. Ogura, *Electrochim. Acta*, 2005, **50**, 3640–3647.

158 P. Fedorko, M. Trznadel, A. Pron, D. Djurado, J. Plans and J. P. Travers, *Synth. Met.*, 2010, **160**, 1668–1671.

159 A. G. Macdiarmid, J. C. Chiang, A. F. Richter and A. J. Epstein, *Synth. Met.*, 1987, **18**, 285–290.

160 V. Guarino, S. Zuppolini, A. Borriello and L. Ambrosio, *Polymers*, 2016, **8,**

161 V. R. Parkhutik, R. D. Calleja and E. M. Matveeva, 1993, **140**, 94–95.

162 I. Morsi, S. Ebrahim and M. Soliman, *Int. J. Photoenergy*, 2012, **2012**.

163 S. E. El-zohary, M. A. Shenashen, N. K. Allam, T. Okamoto and M. Haraguchi, *J. Nanomater.*, 2013, **2013**, 1–8.

164 C. A. Betty, *Biosens. Bioelectron.*, 2009, **25**, 338–343.

165 N. Chiboub, R. Boukherroub, S. Szunerits, N. Gabouze, S. Moulay and S. Sam, *Surf. Interface Anal.*, 2010, **42**, 1342–1346.

166 P. Kumar, S. Adhikari and P. Banerji, *Synth. Met.*, 2010, **160**, 1507–1512.

167 P. Allongue, M. Delamar, B. Desbat, O. Fagebaume, R. Hitmi, J. Pinson and J. M. Sav??ant, *J. Am. Chem. Soc.*, 1992, **114**, 5883–5884.

168 M. Delamar, R. Hitmi, J. Pinson and J. M. Saveant, *J. Am. Chem. Soc.*, 1992, **114**, 5883–5884.

169 A. A. Mohamed, Z. Salmi, S. A. Dahoumane, A. Mekki, B. Carbonnier and M. M. Chehimi, *Adv. Colloid Interface Sci.*, 2015, **225**, 16–36.

170 S. S. C. Yu, E. S. Q. Tan, R. T. Jane and A. J. Downard, *Langmuir*, 2007, **23**, 11074–11082.

171 V. Mévellec, S. Roussel, L. Tessier, J. Chancolon, M. Mayne-L'Hermite, G. Deniau, P. Viel and S. Palacin, *Chem. Mater.*, 2007, **19**, 6323–6330.

172 S. Mahouche-Chergui, S. Gam-Derouich, C. Mangeney and M. M. Chehimi, *Chem. Soc. Rev.*, 2011, **40**, 4143–4166.

173 S. Palacin, C. Bureau, J. Charlier, G. Deniau, B. Mouanda and P. Viel, *ChemPhysChem*, 2004, **5**, 1468–1481.

174 L. M. Santos, J. Ghilane, C. Fave, P. C. Lacaze, H. Randriamahazaka, L. M. Abrantes and J. C. Lacroix, *J. Phys. Chem. C*, 2008, 112, 16103–16109.

175 K. Jlassi, A. Mekki, M. Benna-Zayani, A. Singh, D. K. Aswal and M. M. Chehimi, *RSC Adv.*, 2014, **4**, 65213–65222.

176 K. Jlassi, S. Chandran, M. A. Poothanari, M. Benna-Zayani, S. Thomas and M. M. Chehimi, *Langmuir*, 2016, **32**, 3514–3524.

177 A. Mekki, S. Samanta, A. Singh, Z. Salmi, R. Mahmoud, M. M. Chehimi and D. K. Aswal, *J. Colloid Interface Sci.*, 2014, **418**, 185–192.

178 S. Descroix, G. Hallais, C. Lagrost and J. Pinson, *Electrochim. Acta*, 2013, **106**, 172–180.

179 G. Mula, L. Manca, S. Setzu and A. Pezzella, *Nanoscale Res. Lett.*, 2012, **7**, 377.

180 M. Tiddia, G. Mula, M. Mascia, E. Sechi and A. Vacca, *RSC Adv.*, 2016, **6**, 101880–101887.

181 D. K. Aswal, S. P. Koiry, B. Jousselme, S. K. Gupta, S. Palacin and J. V. Yakhmi, *Phys. E Low-Dimensional Syst. Nanostructures*, 2009, **41**, 325–344.

182 *T. Orazem ME, Electrochemical impedance spectroscopy, 2008, John Wiley & Sons.*

183 D. Hamm, T. Sakka and Y. H. Ogata, *Phys. Status Solidi Appl. Res.*, 2003, **197**, 175–179.

184 F. Priolo, L. Pavesi, L. D. Negro, C. Mazzoleni, G. Franzo, L. Dal Negro, C. Mazzoleni, G. Franzò and F. Priolo, *Nature*, 2000, **408**, 440–4.

185 B. Ortiz, C. Saby, G. Y. Y. Champagne and D. Bélanger, *J. Electroanal. Chem.*, 1998, **455**, 75–81.

186 W. Richard, D. Evrard and P. Gros, *J. Electroanal. Chem.*, 2012, **685**, 109–115.

187 M. Trchová, I. Šeděnková, E. N. Konyushenko, J. Stejskal and G. Ćirić-Marjanović, *J. Phys. Chem. B*, 2006, **110**, 9461–9468.

188 N. Pekmez, K. Pekmez, M. Arca and A. Yildiz, *J. Electroanal. Chem.*, 1993, **353**, 237–246.

189 E. Kang, *Prog. Polym. Sci.*, 1998, **23**, 277–324.

190 L. Pilan, M. Raicopol, A. Pruna and V. Branzoi, *Surf. Interface Anal.*, 2012, **44**, 1198–1202.

191 M. S. Salem, M. J. Sailor, T. Sakka and Y. H. Ogata, *J. Appl. Phys.*, 2007, **101**.

Table of symbols

[BMP] [TFSA]	1-butyl-1-methylpyrrolidinium bis (trifluoromethylsulfonyl)imide
4-NBD	4-nitrobenzenediazonium
A	nominal surface area
ACN	acetonitrile
A_r	real surface area
BDD	boron doped diamond
C_{de}	external capacitance
C_{di}	inner differential capacitance
C_{dl}	double layer capacitance
ConstG-Ni-foams	porous nickel prepared at constant voltage using BDD as substrate and water/glycerol solutions
Const-Ni-foams	porous nickel prepared at constant voltage using BDD as substrate and aqueous solutions
CPs	conducting polymers
CV	cyclic voltammetry
E	potential
E^0	equilibrium potential
E_{appl}	potential applied
E_{corr}	corrosion potential

EEC	electrical equivalent circuit
EIS	electrochemical impedance spectroscopy
HER	hydrogen evolution reaction
i_c	capacitive current
i_{ce}	capacitive current related to the more accessible area
i_o	exchange current density normalized per the nominal surface area
i_{or}	exchange current density normalized per the active surface area
J	current density
LSV	Linear sweep voltammetry
Nb	niobium
$NPt_{0.01}t_{0.05}$	porous nickel prepared at pulsed voltage using Nb as substrate; t_{corr}=0.01s t_{relax}= 0.05s
$NPt_{0.01}t_{0.5}$	porous nickel prepared at pulsed voltage using Nb as substrate; t_{corr}=0.01 s t_{relax}= 0.5s
$NPt_{0.1}t_{0.5}$	porous nickel prepared at pulsed voltage using Nb as substrate; t_{corr}=0.1s t_{relax}= 0.5s
$NPt_{0.1}t_5$	porous nickel prepared at pulsed voltage using Nb as substrate; t_{corr}=0.1s t_{relax}= 5s
NPt_1t_5	porous nickel prepared at pulsed voltage using Nb as substrate; t_{corr}=1s t_{relax}=5s
NPt_1t_{50}	porous nickel prepared at pulsed voltage using Nb as substrate; t_{corr}=1s t_{relax}= 50 s
OCP	open circuit potential

OER	oxygen evolution reaction
PANI	polyaniline
PSi	porous silicon
PSi/Ar/PANI	PSi functionalized by electropolymerization on aminophenyl layer
PSi/PANI	PSi functionalized by direct electropolymerization
Pt	platinum
PulseG-Ni-foams	porous nickel prepared at pulsed voltage using BDD as substrate and water/glycerol solutions
Pulse-Ni-foams	porous nickel prepared at pulsed voltage using BDD as substrate and aqueous solutions
R_{ough}	roughness
SCE	satured calomel electrode
SEM	Scanning Electron Microscopy
Si	silicon
t_{corr}	corrosion time of the pulsed voltage potential
t_{relax}	relaxation time of the pulsed voltage potential
v	scan rate
V_{corr}	corrosion voltage pulse
v_{high}	high scan rate
v_{low}	low scan rate
V_{relax}	relaxation voltage pulse

β	Tafel slope
η	overpotential
η_{10}	overpotential calculated at 10 mA/cm^2
φ	morphologic factor